Helicity Asymmetry E In Eta (547) Meson Photoproduction From The Proton

by

Brian Morrison

A Dissertation Presented in Partial Fulfillment
of the Requirements for the Degree
Doctor of Philosophy

Approved November 2011 by the
Graduate Supervisory Committee:

Barry Ritchie, Chair
Igor Shovkovy
Paul Davies
Michael Dugger
Ricardo Alarcon

ARIZONA STATE UNIVERSITY

December 2011

ABSTRACT

The nucleon resonance spectrum consists of many overlapping excitations. Polarization observables are an important tool for understanding and clarifying these spectra. While there is a large data base of differential cross sections for the process, very few data exist for polarization observables. A program of double polarization experiments has been conducted at Jefferson Lab using a tagged polarized photon beam and a frozen spin polarized target (FROST). The results presented here were taken during the first running period of FROST using the CLAS detector at Jefferson Lab with photon energies ranging from 329 MeV to 2.35 GeV.

Data are presented for the E polarization observable for η meson photoproduction on the proton from threshold ($W = 1500$ MeV) to $W = 1900$ MeV. Comparisons to the partial wave analyses of SAID and Bonn-Gatchina along with the isobar analysis of η-MAID are made. These results will help distinguish between current theoretical predictions and refine future theories.

DEDICATION

To my parents, George and Beverly, for all the support and encouragement they have given me over the years.

ACKNOWLEDGEMENTS

I would like to thank my parents, George and Beverly, my sisters, Heather and Michelle, and all the rest of my family and friends for the support they have given me through this entire process. Without all of you I surely would have lost my way.

Special thanks are also due to my high school physics professor, Dr. Ablidinger, and my undergraduate adviser, Dr. Boukahil. Both of whom mentored me through the early development of my physics career and encouraged me to pursue the field as far as I was capable of going. Without either one, I would have never become the physicist I am today.

I would also like to thank Professor Barry Ritchie, my adviser, without whom none of this would have been possible. Working with Dr. Ritchie has been a great pleasure and he has been an amazing mentor to me as I progressed with my physics career.

Special thanks go out to Assistant Research Professor Michael Dugger and Staff Scientist Eugene Pasyuk. Michael was there every step of the way for me, putting up with my inane banter and random conversations on a daily basis. Eugene took me under his wing when I arrived at Jefferson Lab and guided me along as I learned the ins and out of Linux and the CLAS software and made sure I was fully prepared for working within the CLAS collaboration.

Thanks also go out to the CLAS Collaboration and all collaborators at Jefferson Lab. These people made the experiment that this dissertation is based on successful. I do not have room to thank them all individually, but I am grateful for all of their help.

I would also like to thank my dissertation committee members: Professors Ricardo Alarcon, Igor Shovkovy, and Damien Easson.

Finally, I would like to thank the National Science Foundation for providing the funding that allowed me to pursue and achieve this degree.

TABLE OF CONTENTS

APPENDIX Page

LIST OF TABLES

Table Page

LIST OF FIGURES

Chapter 1

INTRODUCTION

Contemporary theories describe a universe in which nearly all visible mass is composed of quarks. Quarks are spin 1/2 particles having electric, weak, and color charges, and come in six different types (or "flavors"): up, down, strange, charm, top, and bottom. The intrinsic properties of the quarks are given in Table 1.1.

Each flavor of quark has an associated anti-quark with the same mass and lifetime, but the electric charge of the anti-quark is reversed in sign. The possession of a color charge allows for interaction of these particles via strong reactions; particles that interact by way of the strong force are called "hadrons". Many types of hadrons can be made using quarks, differing in properties based on the quarks that comprise them. Mesons are formed from quark anti-quark pairs, while baryons are comprised of a quark trio.

A definitive model for hadronic structure does not exist because no single approach has been able to fully solve the quantum chromodynamic (QCD) Lagrangian. Many quark models of hadrons have been proposed, differing in

Flavor	Charge	Mass	Isospin (I_3)	C	S	T	B'
Up (u)	$+2/3e$	1.7-3.1 MeV	$+\frac{1}{2}$	0	0	0	0
Down (d)	$-1/3e$	4.1-5.7 MeV	$-\frac{1}{2}$	0	0	0	0
Strange (s)	$-1/3e$	100^{+30}_{-20} MeV	0	0	-1	0	0
Charm (c)	$+2/3e$	$1.29^{+0.05}_{-0.11}$ GeV	0	1	0	0	0
Top (t)	$+2/3e$	$172.9 \pm 0.6 \pm 0.9$ GeV	0	0	0	1	0
Bottom (b)	$-1/3e$	$4.19^{+0.18}_{-0.06}$ GeV	0	0	0	0	-1

Table 1.1: Flavors and charges for all known quarks. The u, s, and d quark masses are the current (as opposed to constituent) quark masses, the c and b quark masses are the running quark masses, and the t quark mass is from direct observation. C, S, T and B' are the quark's charm, strangeness, topness and bottomness quantum numbers [1].

approximations used, resulting in differing predictions for the hadronic spectra. Many experimental observations are necessary to help refine these models and help identify the correct features.

Some of the most readily testable portions of these models involve nucleon excited states, or nucleon resonances. There are two types of nucleon resonances that only include u and d quarks: The N^* resonances, which have isospin $I = 1/2$, and the Δ resonances, which have isospin $I = 3/2$. Isospin is a symmetry due to the nearly equal u and d masses and the symmetry due to the strong interaction not depending on electric charge. Isospin can be used to label charge states. There are a total of $2I+1$ charge states, with each charge state labeled by the I_3 quantum number such that

$$Q = I_3 + \frac{B + B^{'} + C + T + S}{2},$$

where B, B', C, T and S are the baryon number, bottom, charm, top, and strange quantum numbers, respectively. For strong interactions, the initial and final states of the reaction must conserve isospin. Thus, based on the isospin of the initial state, combinations of hadrons and mesons can be expected to conserve isospin for strong interactions in the final state.

Many baryon resonances are not well established with current experimental data. At the same time, QCD-based models predict many more nucleon resonances than are observed; these are the so-called "missing" resonances. This is due, in large part, to the complexity of the resonance spectrum for the different reactions. For example, the resonance spectrum for the $\gamma + p \rightarrow \pi^+ + n$ reaction has many broad and overlapping states, as can be seen in Figure 1.1.

The overlapping structure of the nucleon resonance spectrum causes complexities when attempting to analyze resonance channels. One way to mitigate this is to decompose the resonance spectrum using the isospin properties of the reactions.

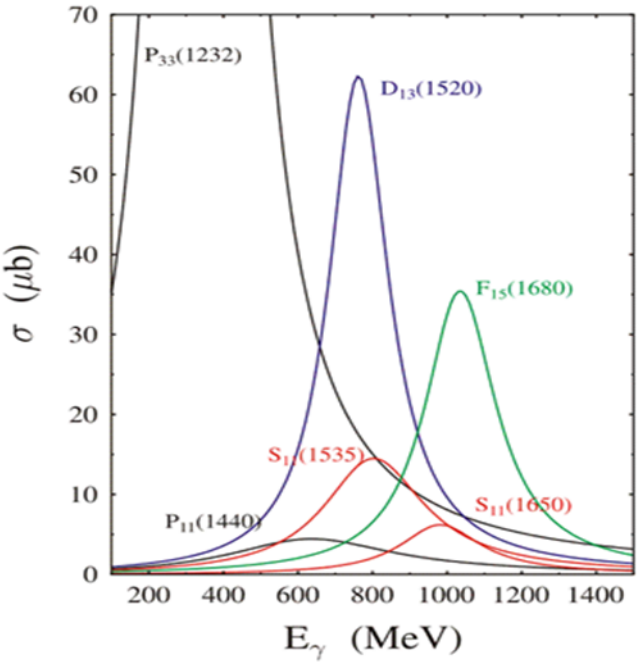

Figure 1.1: Relative strengths of resonances for the $\gamma + p \rightarrow \pi^+ + n$ reaction below E_γ = 1.5 GeV. The notation for the resonances is in the $L_{2I,2J}$ format, where L is the orbital angular momentum of the resonance (in terms of S, P, D, etc.), I is the isospin, and J is the total angular momentum of the resonance. Note that both $I = 1/2$ (N^*) and $I = 3/2$ (Δ) resonances are present [6].

In particular, requiring $I = 0$ mesons in the final state for photoproduction isolates the $I = 1/2$ resonances due to isospin conservation of strong interactions. By requiring an individual $I = 0$ meson in the final state, the resonances in the final state must be of the N^* type for one-step processes, effectively constructing an isospin filter for the resonance spectrum. Because the η meson is the lightest $I = 0$ meson, the η meson makes a good choice for isolating the N^* ($I = 1/2$) spectrum. Compared to the π^+ resonance spectrum, the η spectrum is much cleaner and does not include the Δ states, as seen in Figure 1.2. A large part of the extra complexity in the $\pi^+ n$ resonance spectrum is due to the π^+ being an $I = 1$ meson, which allows for $I = 3/2$ final states. The complication due to of the $I = 3/2$ states can be seen clearly with the

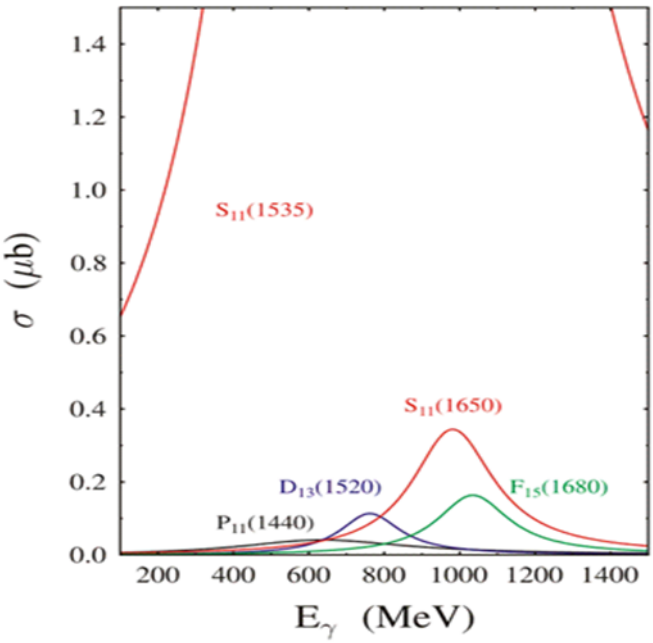

Figure 1.2: Relative strengths of resonances for the $\gamma + p \rightarrow p + \eta$ reaction below E_γ = 1.5 GeV [6].

Clebsch-Gordan decomposition for the reaction $\pi^+ + n$:

$$|\,11\rangle \oplus |\,\frac{1}{2}\frac{-1}{2}\rangle = \left(\frac{1}{\sqrt{3}}\right)|\,\frac{3}{2}\frac{1}{2}\rangle + \sqrt{\frac{2}{3}}\,|\,\frac{1}{2}\frac{1}{2}\rangle.$$

The notation is in the form of $|\,II_3\rangle$, where I is the isospin of the particle and I_3 is the isospin projection for the particle of interest. The first term has a clear $I = 3/2$ state, indicating Δ resonance couplings. In comparison, the η is a state of $|\,00\rangle$ as an $I = 0$ singlet neutral meson, and when coupled with the proton the Clebsch-Gordan decomposition for $\eta + p$ is trivial:

$$|\,00\rangle \oplus |\,\frac{1}{2}\frac{1}{2}\rangle = |\,\frac{1}{2}\frac{1}{2}\rangle$$

Thus, there are no Δ resonances with η photoproduction from the proton in one-step processes.

As shown in Table 1.2, despite the advantages of using η photoproduction as an isospin filter, very little data is currently available for these kinds of reactions. The

degree of certainty ("confidence") in the resonances shown in Table 1.2 are given in terms of stars, ranging from 1-star to 4-star. A four-star rating (****) indicates that the existence of the resonance is certain and the properties are at least fairly well determined, while a one-star (*) rating means the evidence for existence of the resonance is poor.

The lack of overall confidence for a majority of the N^* resonances in the $N\eta$ column of Table 1.2 clearly shows that, beyond the $S_{11}(1535)$, very few resonances have been definitively established. This is primarily due to the lack of available data for these resonances, and a lack of data on η meson production. Table 1.3 shows the state of the database for published η photoproduction from the proton. There are currently no published data points for double polarization observables for η photoproduction. Double polarization observables require two participants in the reaction be polarized: beam + target, beam + recoil, or target + recoil polarizations

Because of the lack of data, investigations like the experiment that provided the data for the work described in this dissertation have been conducted to provide values for the different spin observables needed to more fully determine each resonance amplitude. As discussed in chapter 2, a full resonance amplitude description can only be completely determined with a combination of eight observables out of the sixteen observables available: The differential cross-section, beam polarization, target asymmetry, recoil polarization and a combination of four double polarization observables from at least two different groupings (possible groupings are target-beam, target-recoil, and beam-recoil polarization). Table 1.4 shows the relation between the possible polarizations of the beam, the target proton, and recoil proton and the observables that can be obtained. In particular, the E observable can be obtained with a circularly polarized photon beam and a longitudinally polarized target, a condition that was met in this experiment.

Particle	$L_{2I\cdot 2J}$	Status	$N\pi$	$N\eta$	$K\Delta$	$K\Sigma$	$\Delta\pi$	$N\rho$	$N\gamma$
N(939)	P_{11}	****							
N(1440)	P_{11}	****	****	*			***	*	***
N(1520)	D_{13}	****	****	***			****	****	****
N(1535)	S_{11}	****	****	****			*	**	***
N(1650)	S_{11}	****	****	*	***	**	***	**	***
N(1675)	D_{15}	****	****	*	*		****	*	****
N(1680)	F_{15}	****	****	*			****	****	****
N(1700)	D_{13}	***	***	*	**	*	**	*	**
N(1710)	P_{11}	***	***	**	**	*	**	*	***
N(1720)	P_{13}	****	****	*	**	*	*	**	**
N(1900)	P_{13}	**	**					*	
N(1990)	F_{17}	**	**	*	*	*			*
N(2000)	F_{15}	**	**	*	*	*	*	**	
N(2080)	D_{13}	**	**	*	*				*
N(2090)	S_{11}	*	*						
N(2100)	P_{11}	*	*	*					
N(2190)	G_{17}	****	****	*	*	*		*	*
N(2200)	D_{15}	**	**	*	*				
N(2220)	H_{19}	****	****	*					
N(2250)	G_{19}	****	****	*					
N(2600)	I_{111}	***	***						
N(2700)	K_{113}	**	**						
Particle	$L_{2I\cdot 2J}$	Status	Nπ	Nη	ΔK	ΣK	$\Delta\pi$	Nρ	Nγ
Δ(1232)	P_{33}	****	****	F	F				****
Δ(1600)	P_{33}	***	***	o	o		***	*	**
Δ(1620)	S_{31}	****	****	r	r		****	****	***
Δ(1700)	D_{33}	****	****	b	b	*	***	**	***
Δ(1750)	P_{31}	*	*	i	i				
Δ(1900)	S_{31}	**	**	d	d	*	*	**	*
Δ(1905)	F_{35}	****	****	d	d	*	**	**	***
Δ(1910)	P_{31}	****	****	e	e	*	*	*	*
Δ(1920)	P_{33}	***	***	n	n	*	**		*
Δ(1930)	D_{35}	***	***			*			**
Δ(1940)	D_{33}	*	*	F	F				
Δ(1950)	F_{37}	****	****	o	o	*	****	*	****
Δ(2000)	F_{35}	**		r	r		**		
Δ(2150)	S_{31}	*	*	b	b				
Δ(2200)	G_{37}	*	*	i	i				
Δ(2300)	H_{39}	**	**	d	d				
Δ(2350)	D_{35}	*	*	d	d				
Δ(2390)	F_{37}	*	*	e	e				
Δ(2400)	G_{39}	**	**	n	n				
Δ(2420)	H_{311}	****	****						*
Δ(2750)	I_{313}	**	**						
Δ(2950)	K_{315}	**	**						

Table 1.2: Current confidence for observed N^* and Δ resonances from the Particle Data Group. The notation of the first column indicates the average mass for each resonance, the second column indicates the type , and the star notation as described in the text [2].

The goal of this dissertation is to provide measurements of the double polarization observable E using the data gathered during the FROST experiment conducted at Thomas Jefferson National Accelerator Facility (Jefferson Lab or JLab).

Observable	Number of data points
σ_{tot}	66
$d\sigma/d\Omega$	1020
P	7
Σ	166
T	50
Other	2
Total	1311

Table 1.3: The database statistics for η photoproduction on the proton. The asymmetry measurements Σ are from Grenoble (GRAAL), Bonn, and Yerevan, the T measurements are target asymmetries from Bonn. P (recoil proton) and some observables from smaller contributions. The data for this table was obtained from the historically-named "Scattering-Analysis-Interactive-Dial-In" (now simply called SAID) web page [3] on September 6th, 2011.

In summary, obtaining data for double polarization observables from η photoproduction on the proton is vital to understanding the nucleon resonance spectrum. Data has been collected at JLab and analyzed to provide the first measurements for the E double polarization observable in η photoproduction from the proton. In Chapter 2 the theoretical background for this analysis is discussed along with the theoretical predictions with which the results are compared. Chapter 3 details the techniques used in the experiment, including discussions about the polarized electron beam, the tagged bremsstrahlung facility, the frozen spin target, and the detector used. Chapter 4 discusses the analysis techniques used to reduce the data,

Polarization	Target				Recoil			Target + Recoil			
	-	-	-	-	x'	y'	z'	x'	y'	z'	z'
	-	x	y	z	-	-	-	x	z	x	z
unpolarized	σ_0	0	T	0	0	P	0	$T_{x'}$	$-L_{x'}$	$T_{z'}$	$L_{z'}$
linear	$-\Sigma$	H	(-P)	-G	$O_{x'}$	(-T)	$O_{z'}$	$(-L_{z'})$	$(T_{z'})$	$(L_{x'})$	$(-T_{x'})$
circular	0	F	0	-E	$-C_{x'}$	0	$-C_{z'}$	0	0	0	0

Table 1.4: The possible observables for pseudoscaler meson photoproduction experiments and the experimental requirements for measuring each observable. The polarization column refers to the overall polarization of the incoming photon beam.

including detailed discussion of procedures applied before true analysis commences. In Chapter 5, the results for analysis of the E polarization observable for η meson photoproduction from the proton are shown and compared to theoretical predictions. Chapter 6 provides a discussion of the implications of the results shown in Chapter 5, and what future measurements are expected.

Chapter 2

BACKGROUND

This experiment explores η photoproduction on the proton and the double polarization helicity asymmetry E. An understanding of helicity and helicity asymmetry is necessary for comprehension of this topic, along with the methods used to predict the values for these asymmetries at various energies. For this dissertation, predictions from Bonn-Gatchina [14] and the historically-named "Scattering-Analysis-Interactive-Dial-In" (now simply called SAID) [3] will be used. This chapter will discuss helicity, partial-wave analysis methods, how bremsstrahlung is used in CLAS photon experiments, and how dynamic nuclear polarization functions in the polarized nucleon target used in the experiment on which data was obtained.

2.1 Helicity

The definition of helicity and the helicity asymmetry are described elsewhere for single-pseudoscaler meson photoproduction[15]; an overview of that derivation is presented here. To start, define the initial photon 4-momentum as $k = (\mathbf{k}, k)$, the 4-momentum of the outgoing meson as $q = (\mathbf{q}, \omega)$, and the 4-momenta of the incident and final state nucleons as $p_1 = (\mathbf{p}_1, E_1)$ and $p_2 = (\mathbf{p}_2, E_2)$, respectively. Next, the amplitude A is defined and related to the S matrix by

$$S = 1 + (2\pi)^4 i\delta^4\left(P_f - P_i\right)(8\pi WN)A$$

where N is the normalization factor $\sqrt{16k\omega E_1 E_2}$, ω is the energy of the meson, and W is the total energy in the system. The spin dependence of the system is then brought into A by writing A as a matrix in terms of initial and final spin states

$$A = \begin{pmatrix} A_{11} & A_{12} \\ A_{21} & A_{22} \end{pmatrix}.$$

If the spins are then quantized along the directions of **q** and **k** in the center-of-momentum frame, the elements of A then become the helicity amplitudes $A_{\mu\lambda}$, where the final total helicity is $\mu = \lambda_q - \lambda_2$, the initial helicity is $\lambda = \lambda_k - \lambda_1$, λ_1 (λ_2) is the helicity of the initial (final) proton, λ_q is the helicity of the outgoing meson, and λ_k is the helicity of the incident photon. Since real, transverse photons will have a spin of ± 1, λ will have values of $\pm 1/2$ and $\pm 3/2$ when considering an initial state of $\gamma + p$. Also, since η is a pseudoscalar spin-0 meson, the final state has $\mu = -\lambda_2$. This yields eight possible helicity amplitudes. However, through parity symmetry, half the amplitudes can be mapped to the others through a phase shift as given by

$$A_{-\mu-\lambda}(\theta,\phi) = -e^{i(\lambda-\mu)(\pi-2\phi)} A_{\mu\lambda}(\theta,\phi).$$

The four unique helicity amplitudes are labeled as H_1,...H_4, with $\lambda_k = +1$ and $\phi = 0$ in **q**. The relationships between the helicity amplitude H_i and the helicities for $\lambda_k = +1$ are given in Table 2.1.

The total differential cross section for the reaction is:

$$\sigma(\theta) = \frac{1}{2}\frac{q}{k}\sum_{i=1}^{4} |H_i|^2$$

The total differential cross sections for the final-state helicity 3/2 states and final-state helicity 1/2 states are

$$\sigma_{3/2}(\theta) = \frac{1}{2}\frac{q}{k}\sum_{i=1,3} |H_i|^2$$

	3/2	1/2
1/2	H_1	H_2
−1/2	H_3	H_4

Table 2.1: The relationship between the helicity amplitude H_i and the helicities for $\lambda_k = +1$. The top row represents the initial spin state of the system and the left column is the final spin state of the system.

and

$$\sigma_{1/2}(\theta) = \frac{1}{2}\frac{q}{k}\sum_{i=2,4} |\, H_i \,|^2 \,.$$

With the differential cross section information about the helicity 3/2 and 1/2 states separated, a comparison between them can be made. Since each helicity amplitude is complex, eight independent numbers are needed to completely specify the full quantum mechanical amplitude. However, the overall phase is not observable, leaving only seven independent numbers that can be experimentally determined. Due to the interdependence of the possible spin observables, the minimum number of observables required to measure the seven numbers is eight.

An asymmetry is the fractional difference between two values v_1 and v_2, and takes the form

$$N = \frac{v_1 - v_2}{v_1 + v_2}.$$

N will have values between 1 and -1. The asymmetry relating the differential cross sections for helicity 1/2 and 3/2 states is the double polarization observable E, one of the 8 measurements necessary for fully specifying the full quantum mechanical amplitude:

$$E = \frac{\sigma_{1/2} - \sigma_{3/2}}{\sigma_{1/2} + \sigma_{3/2}}$$

Empirically, this equation can be measured by determining the yield for each spin state

$$\sigma_\lambda = \frac{Y_\lambda}{N_{\lambda\gamma}\varepsilon n}.$$

where σ_λ is the cross section for initial helicity state λ_k, Y_λ is the measured yield for the spin state, ε is the detection efficiency, n is the number of scattering centers per unit area, and $N_{\lambda\gamma}$ is the number of incident photons for the initial helicity state. If there is an equal number of incident photons for both spin states, the equation for the helicity asymmetry E can be written in terms of yields as

$$E = \frac{Y_{1/2} - Y_{3/2}}{Y_{1/2} + Y_{3/2}}.$$

An example for this equation is the helicity asymmetry E for the $S_{11}(1535)$ nucleon resonance, which dominates η photoproduction near threshold. (The threshold energy for η photoproduction is $E_\gamma = 707$ MeV and $W = 1485$ MeV) Since the $S_{11}(1535)$ is a $S = 1/2$ nucleon resonance with $L = 0$, the helicity asymmetry E for the production of an $S_{11}(1535)$ resonance can only have a value of $+1$. Thus, at threshold for η photoproduction from the proton where the $S_{11}(1535)$ dominates (see Figure 1.2), E should be $+1$.

2.2 Partial-wave analysis methods

Partial-wave analyses can be used on existing data for experimental observables to predict observables where little or no current data exist. Such analyses provide predictions based on what might be expected from current trends in the data if the behavior is consistent in unexplored regions. The technique can provide evidence for the existence of a resonance based on trajectories in an Argand plot, using the complex energy plane and some assumed phenomenological form for resonances (e.g., a Breit-Wigner form with further assumptions about branching ratios, spin, etc.). The non-relativistic formalism, as described in Reference [16], takes a generalized scattering amplitude expanded in terms of Legendre polynomials

$$f(k,\theta) = \frac{1}{k}\sum_l (2l+1) a_l P_l(\cos\theta)$$

Though unsolvable as an infinite expansion, truncating this series at some order l leads to a fit to the data as each Legendre polynomial included adds another possible resonance to the spectrum. To find a resonance associated with any particular order l, the elastic amplitude a_l may be written as a Breit-Wigner plus an additional background term

$$a_l = \frac{\Gamma_{el}}{2} \cdot \frac{1}{W_R - W - i\frac{\Gamma_{tot}}{2}} + B. \tag{2.1}$$

Here W_R is the center-of-mass energy of the resonance, Γ_{el} is the elastic width of the resonance, Γ_{tot} is the total width of the resonance, W is the center-of-mass energy for

the initial system, and B is a generalized background term. Resonances will occur when a pole is reached in the complex plane, with the pole having a value of

$$E = E_R + i\frac{\Gamma_{tot}}{2}.$$

While the formalism in Equation 2.1 does not take into account spin, the partial wave analysis approach with spin included is similar.

The plane-wave analysis code Scattering Analysis Interactive Dial-In (SAID) [3] was developed by Prof. R. A. Arndt and collaborators at Virginia Polytechnic Institute and State University, and is now maintained by the Center for Nuclear Studies at George Washington University. SAID does not assume any resonances *a priori*, but rather determines the presence of resonances with two assumptions: (1) a pole for a resonance will be found in the imaginary plane close to the real axis, and (2) a Breit-Wigner equation plus a background term describes the process. Extracting the angular momentum and isospin quantum numbers yields resonance couplings.

Another plane-wave analysis code that has been developed is maintained by the Bonn-Gatchina analysis group [14]. Over 1000 fits are performed to validate a given partial wave solution. The number of resonances, spin, parity, and relative weight of the included data sets are all varied in the fitting routines. Any new resonances predicted are tested against current data using an omit/replace χ^2 method. The process looks at the change in χ^2 overall and for each individual final state when the new resonance is omitted, and then when replaced by resonances with different spin and parity. The team at Bonn-Gatchina currently use 14 N^* resonances coupling to $N\pi$, $N\eta$, $K\Lambda$, and $K\Sigma$ along with 7 Δ resonances coupling to $N\pi$ and $K\Sigma$ in their partial wave analysis [17].

2.3 Isobar analysis methods

Another model that will be used to interpret the results of this work is the Mainz unitary isobar model for η photo- and electroproduction (η-MAID) [4]. This model divides the response of the nucleon in photoproduction into a non-resonant background contribution and a multipole resonance isobar contribution.

The contribution for the non-resonant background is determined from an effective Lagrangian consisting of Born terms and vector meson interactions. The effective Lagrangian terms for the Born contribution for η photo- and electroproduction include the electromagnetic vertex

$$L_{\gamma NN} = -e\overline{\psi}\left[\gamma_\mu A^\mu F_1^{p,n}(Q^2) + \frac{\sigma_{\mu\nu}}{2m_N}(\partial^\mu A^\nu)F_2^{p,n}(Q^2)\right]\psi, \tag{2.2}$$

the pseudoscalar coupling

$$L_{\eta NN}^{PS} = -ig_{\eta NN}\overline{\psi}\gamma_5\psi\phi_\eta, \tag{2.3}$$

and the pseudovector coupling

$$L_{\eta NN}^{PV} = \frac{f_{\eta NN}}{m_\eta}\overline{\psi}\gamma_5\gamma_\mu\psi\partial^\mu\phi_\eta. \tag{2.4}$$

where $\partial^\mu A^\nu$ is the photon term and ϕ_η is the η meson field. The effective Lagrangian terms for vector meson interactions are given by the term for the $\gamma-\eta$-vector meson vertex,

$$L_{\gamma\eta V} = \frac{e\lambda_V}{m_\eta}\varepsilon_{\mu\nu\rho\sigma}(\partial^\mu A^\nu)\phi_\eta(\partial^\rho V^\sigma)F_V^{em}(Q^2) \tag{2.5}$$

where $\partial^\rho A^\sigma$ is the vector meson field in the interaction, and by the term for the nucleon-nucleon-vector electromagnetic vertex

$$L_{VNN} = \overline{\psi}\left(g_\nu\gamma_\mu + \frac{g_t}{2m_N}\sigma_{\mu\nu}\partial^\nu\right)V^\mu\psi \tag{2.6}$$

which is nearly identical to the photon electromagnetic term. The electromagnetic couplings of the vector mesons λ_V in Equation 2.5 are determined from the radiative

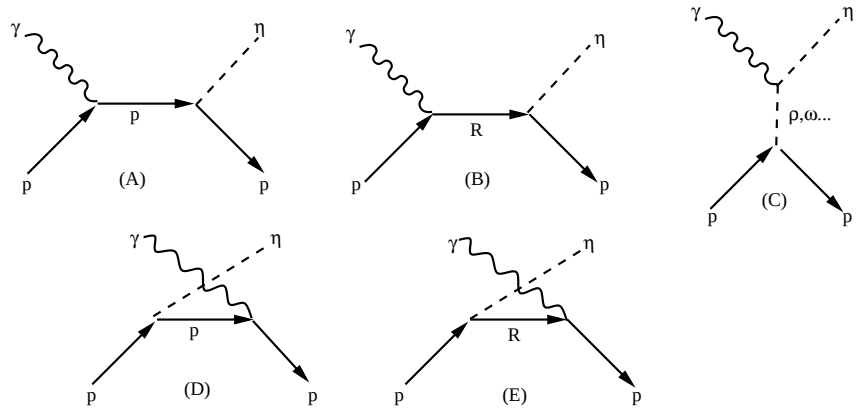

Figure 2.1: Feynman diagrams for (A) the *s*-channel Born term, (B) the *s*-channel resonance excitation term, (C) vector meson exchange, (D) the *u*-channel Born term, and (E) the *u*-channel resonance excitation term.

decay widths, and the electromagnetic form factor is assumed to have dipole behavior

$$\frac{1}{\left(1-\frac{Q^2}{0.71(GeV^2/c^2)}\right)^2},$$

where $Q^2 = -k^2$. The strong coupling constants $\tilde{g_v}$ and $\tilde{g_t}$ are considered free parameters in the fitting routines used by η-MAID, since their values are not well determined by current data. Feynman diagrams for these interactions are shown in Figure 2.1.

The multipole resonance contribution is constructed using a Breit-Wigner energy dependence of the form

$$M_{l\pm}(W,Q^2) = \tilde{M_{l\pm}}(Q^2)\frac{W_R\Gamma_{tot}(W)}{W_R^2 - W^2 - iW_R\Gamma_{tot}(W)}f_{\eta N}(W)C_{\eta N}$$

for η photo- and electroproduction. The term $f_{\eta N}(W)$ describes the ηN decay of the N^* resonance with total width Γ_{tot}. The Breit-Wigner form is directly correlated to known data through the masses, widths, branching ratios and photon couplings of each resonance. The specific resonances used in η-MAID are given in Table 2.3.

Unlike isobar models for pions, there is no explicit resonance phase term for η as the necessary information on η-nucleon scattering is not yet available. The free or

N^*	Mass (MeV)	Width (MeV)	$\beta_{\eta N}$	$\beta_{\pi N}$	$\beta_{\pi\pi N}$
$D_{13}(1520)$	1520	120	0.08±0.01%	50-60%	40-50%
$S_{11}(1535)$	1520-1555	100-250	30-55%	35-55%	1-10%
$S_{11}(1650)$	1640-1680	145-190	3-10%	55-95%	10-20%
$D_{15}(1675)$	1670-1685	150	0.1±0.1%	40-50%	50-60%
$F_{15}(1680)$	1675-1690	130	0.15±0.3%	60-70%	30-40%
$D_{13}(1700)$	1700	100	10±6%	5-15%	85-95%
$P_{11}(1710)$	1680-1740	100	16±10%	10-20%	40-90%
$P_{13}(1720)$	1720	150	0.2±1%	10-20%	¿70%

Table 2.2: The resonances included in the η-MAID isobar analysis for η photo- and electroproduction [4]. Values for the masses are established from the Particle Data Group. β terms are the branching ratios of particular decay channels.

uncertain parameters for η-MAID are fixed by a least-squares fitting method. The data used for these fits are the total and differential photoproduction cross sections from MAMI and GRAAL, the photon asymmetry of GRAAL, and the electroproduction cross sections from JLab. The data provided by this work will be especially useful in better determining the parameters used in the model. The results of η-MAID have been in agreement with current data up to $Q^2 = 4.0$ GeV.

2.4 Production of polarized photon beams using polarized electron beams

Polarized electron beams can be used to generate polarized photon beams. Circularly polarized bremsstrahlung photons can be generated by the scattering of polarized electron beams, while linearly polarized photon beams can be generated by the scattering of circularly polarized electron beams. Based on the type of radiator used and the properties of the incoming electron beam, both linearly and circularly polarized photon beams can be produced. For the purpose of this dissertation, the equations describing how to obtain a generalized polarization amplitude for a circularly polarized photon beam will be discussed, as detailed elsewhere by Olsen and Maximon [18].

The general Sommerfeld-Maue type wave function for an electron is

$$\psi_{\pm} = e^{i\mathbf{p}\cdot\mathbf{r}}(1 - \frac{i\overrightarrow{\alpha}\cdot\overrightarrow{\bigtriangledown}}{2\varepsilon})uF_{\pm}$$

where the + and - represent incoming and outgoing wave functions, $\varepsilon = \sqrt{p^2+1}$ where ε is the electron energy, and $m_e c^2$ is set to 1. F is a function of position $\mathbf{r}$ that is normalized such that F goes to 1 as r $\rightarrow \infty$. The free-particle spinor is u, and $\overrightarrow{\alpha}$ is the Dirac operator

$$\overrightarrow{\alpha} = \begin{pmatrix} 0 & \overrightarrow{\sigma} \\ \overrightarrow{\sigma} & 0 \end{pmatrix}.$$

The free-particle spinor u is rewritten explicitly in terms of the two component Pauli spinors v and w and a normalization factor N through the relations

$$\left(\overrightarrow{\alpha}\cdot\mathbf{p} + \beta - \varepsilon\right) = u,$$

$$u = N\begin{pmatrix} v \\ w \end{pmatrix},$$

$$\overrightarrow{\sigma}\cdot\mathbf{p}w + (1-\varepsilon)v = 0,$$

and

$$\overrightarrow{\sigma}\cdot\mathbf{p}v - (1-\varepsilon)w = 0.$$

Using these relations yields the free particle spinor

$$u = N\begin{pmatrix} 1 \\ \overrightarrow{\sigma}\cdot\mathbf{p}/(\varepsilon+1) \end{pmatrix}$$

where $N = [(\varepsilon+1)/2\varepsilon]^{\frac{1}{2}}$ and v is assumed to be normalized to 1.

For modeling an electron undergoing bremsstrahlung, a value of $N = 1/\sqrt{2}$ is obtained in the above equation assuming $\varepsilon \gg 1$, giving the general wave function

equation for an electron

$$\psi_{el,\pm} = \frac{1}{\sqrt{2}} e^{i\mathbf{p}\cdot\mathbf{r}} (1 - \frac{i\overrightarrow{\alpha}\cdot\overrightarrow{\bigtriangledown}}{2\varepsilon}) \begin{pmatrix} 1 \\ \overrightarrow{\sigma}\cdot\mathbf{p}/(\varepsilon+1) \end{pmatrix} vF_{\pm} \tag{2.7}$$

where again the + indicates incoming wave functions and the - indicates outgoing.

The amplitude for the bremsstrahlung process is $\mathbf{A}\cdot\mathbf{e}^*$, with $\mathbf{e}$ being a complex vector with a_1 in the x-direction, a_2 in the y-direction, and with the propagation of the photon beam in the $+z$ direction, normalized such that

$$\mathbf{e} = a_1\mathbf{e}_x + a_2\mathbf{e}_y,$$

and

$$|\mathbf{e}|^2 = |a_1|^2 + |a_2|^2 = 1.$$

With this choice of normalization, the method for determining the polarization of the photons produced through the coherent bremsstrahlung process is entirely dependent on the values of a_1 and a_2. Values of 1 for either variable will yield purely linear polarization in either the x or y-plane. A combination of $a_1 = 1/\sqrt{2}$ and $a_2 = \pm i/\sqrt{2}$ will yield purely circularly polarized photons, with the direction of polarization being determined by the sign of a_2 (right-handed helicity being positive and left-handed helicity being negative).

When the spin states of the incoming and outgoing electron are taken into account, as given by Equation 2.7, the equation for the amplitude of the coherent bremsstrahlung can be written as

$$\mathbf{A}\cdot\mathbf{e}^* = (\psi_{2,-}, \overrightarrow{\alpha}\cdot\mathbf{e}^* e^{-i\mathbf{k}\cdot\mathbf{r}}\psi_{1,+})$$

where ψ_1 is the initial electron wave function, ψ_2 is the final electron wave function, and $\mathbf{k}$ is the photon momentum.

The above equation can then be rewritten in terms of three unique integrals with the assumption that terms of the order $1/\varepsilon$ (large ρ) are small enough to discard.

$$I_1 \equiv \int F^*_{2,-} e^{i\mathbf{q}\cdot\mathbf{r}} F_{1,+} d^3r \tag{2.8}$$

$$\mathbf{I}_2 \equiv -\frac{i}{2\varepsilon_1} \int F^*_{2,-} e^{i\mathbf{q}\cdot\mathbf{r}} \overrightarrow{\bigtriangledown} F_{1,+} d^3r \tag{2.9}$$

$$\mathbf{I}_3 \equiv \frac{i}{2\varepsilon_2} \int \left(\overrightarrow{\bigtriangledown} F^*_{2,-} \right) e^{i\mathbf{q}\cdot\mathbf{r}} F_{1,+} d^3r \tag{2.10}$$

The amplitude is thus

$$\mathbf{A}\cdot\mathbf{e}^* = \left(u_2, \left[\overrightarrow{\alpha}\cdot\mathbf{e}^* I_1 + \overrightarrow{\alpha}\cdot\mathbf{e}^* \overrightarrow{\alpha}\cdot\mathbf{I}_2 + \overrightarrow{\alpha}\cdot\mathbf{I}_3 \overrightarrow{\alpha}\cdot\mathbf{e}^*\right] u_1\right).$$

Note here that the I_1 is a scalar quantity, while $\mathbf{I}_2$ and $\mathbf{I}_3$ are vector quantities. All three integrals are related by the following equation

$$\mathbf{I}_3 = \frac{\varepsilon_1}{\varepsilon_2}\mathbf{I}_2 + \frac{\mathbf{q}}{2\varepsilon_2} I_1.$$

This allows the bremsstrahlung amplitude to be simplified to require only two integrals. Olsen and Maximon state that, at high energies, the only components of $\mathbf{I}_2$ and $\mathbf{I}_3$ that contribute to the matrix elements are those that are perpendicular to $\mathbf{k}$. With this assumption, and using the relation $\mathbf{q} = \mathbf{p}_1 - \mathbf{p}_2$ the following relationships may be obtained:

$$\left(u_2, \overrightarrow{\alpha}\cdot\mathbf{e}^* \overrightarrow{\alpha}\cdot\mathbf{I}_2 u_1\right) = \left(v_2, \overrightarrow{\sigma}\cdot\mathbf{e}^* \overrightarrow{\sigma}\cdot\mathbf{I}_{2\perp} v_1\right)$$

$$\left(u_2, \overrightarrow{\alpha}\cdot\mathbf{I}_3 \overrightarrow{\alpha}\cdot\mathbf{e}^* u_1\right) = \left(v_2, \overrightarrow{\sigma}\cdot\mathbf{I}_{3\perp} \overrightarrow{\sigma}\cdot\mathbf{e}^* v_1\right)$$

With these results, a vector $\mathbf{J}$ can be introduced for convenience

$$J_z = -\frac{1}{2\varepsilon_1\varepsilon_2} I_1,$$

such that

$$\mathbf{J}_\perp = \frac{\mathbf{u}}{2\varepsilon_1\varepsilon_2} I_1 + \frac{1}{\varepsilon_2}\mathbf{I}_{2\perp} = \frac{\mathbf{v}}{2\varepsilon_1\varepsilon_2} I_1 + \frac{1}{\varepsilon_1}\mathbf{I}_{3\perp}.$$

The above relation is made possible by the relation $\mathbf{q}_\perp = \mathbf{u} - \mathbf{v}$ and because $\mathbf{u}$ is the part of $\mathbf{p}_1$ which is perpendicular to $\mathbf{k}$, while $\mathbf{v}$ is the portion of $\mathbf{p}_2$ perpendicular to $\mathbf{k}$. This allows the amplitude $\mathbf{A}\cdot\mathbf{e}^*$ to be written as

$$\mathbf{A}\cdot\mathbf{e}^* = \left(v_2, \left[\overrightarrow{\sigma}\cdot\mathbf{e}^*\left(\frac{\overrightarrow{\sigma}\cdot\mathbf{u}}{2\varepsilon_1} + \overrightarrow{\sigma}\cdot\mathbf{I}_{2\perp} - \frac{\sigma_z}{2\varepsilon_1}I_1\right) + \left(\frac{\overrightarrow{\sigma}\cdot\mathbf{v}}{2\varepsilon_2} + \overrightarrow{\sigma}\cdot\mathbf{I}_{3\perp} - \frac{\sigma_z}{2\varepsilon_2}I_1\right)\overrightarrow{\sigma}\cdot\mathbf{e}^*\right]v_1\right),$$

which, when written in terms of $\mathbf{J}$, gives

$$\mathbf{A}\cdot\mathbf{e}^* = \left(v_2, \{\varepsilon_2\overrightarrow{\sigma}\cdot\mathbf{e}^*\overrightarrow{\sigma}\cdot\mathbf{J} + \varepsilon_1\overrightarrow{\sigma}\cdot\mathbf{J}\overrightarrow{\sigma}\cdot\mathbf{e}^*\}v_1\right).$$

Using the identity $\left(\overrightarrow{\sigma}\cdot\mathbf{A}\right)\left(\overrightarrow{\sigma}\cdot\mathbf{B}\right) = \mathbf{A}\cdot\mathbf{B} + i\overrightarrow{\sigma}\cdot\mathbf{A}\times\mathbf{B}$ for arbitrary vectors $\mathbf{A}$ and $\mathbf{B}$, this may be simplified to:

$$\mathbf{A}\cdot\mathbf{e}^* = \left(v_2, \{(\varepsilon_1+\varepsilon_2)\mathbf{J}\cdot\mathbf{e}^* + ik\overrightarrow{\sigma}\times\mathbf{J}\cdot\mathbf{e}^*\}v_1\right).$$

This may be applied to find the differential cross section for arbitrarily polarized bremsstrahlung. The matrix element H'_{12} for bremsstrahlung (the full quantum mechanical amplitude) is found first. From this point forward, the electron charge e, Plank's constant $\hbar$, the speed of light c, and the mass of the electron m_e are reintroduced and shown explicitly in the equations. The matrix element is given by the equation

$$H'_{12} = -e\hbar c\,(2\pi/k)^{\frac{1}{2}}\,(\hbar/mc)^3\,\mathbf{A}\cdot\mathbf{e}^*.$$

The transition probability per unit time written in terms of the density of final states (ρ_f) is

$$w = (2\pi/\hbar)\,\rho_f|H'_{12}|^2,$$

where

$$\rho_f = \left(mc^2\right)^4(2\pi c)^{-6}k^2dkd\Omega_1p_2\varepsilon_2d\Omega_2.$$

By dividing w by the velocity of the incident electron (cp_1/ε_1) and using the high-energy approximation of $\varepsilon = p$, the differential cross section for arbitrarily

polarized bremsstrahlung is

$$d\sigma = \frac{1}{(2\pi)^4}\frac{e^2}{mc^2}\frac{\hbar}{mc}\frac{e_2^2}{k}|\mathbf{A}\cdot\mathbf{e}^*|^2 k^2 dk d\Omega_1 d\Omega_2.$$

With the differential cross section for arbitrarily polarized bremsstrahlung, the amount of circular polarization P can be determined based on the differential cross sections of both the right-handed and left-handed circularly polarized bremsstrahlung

$$P = \frac{d\sigma_{right} - d\sigma_{left}}{d\sigma_{right} + d\sigma_{left}}.$$

Since screening has negligible influence on the polarization curve, Olsen and Maximon approximate the circular polarization of the photon beam produced through bremsstrahlung with the equation

$$P_{(\mathbf{p}_1,\zeta_1,\mathbf{e}_{circ})} = \frac{k\left(\varepsilon_1 + \frac{1}{3}\varepsilon_2\right)\zeta_{1z}}{\varepsilon_1^2 + \varepsilon_2^2 - \frac{2}{3}\varepsilon_1\varepsilon 2}$$

where ζ_1 refers to the initial spin, ζ_{1z} is the polarization term, $\mathbf{e}_{circ}$ is the polarization of radiation, ε_1 (ε_2) refer to the energies of the incoming (outgoing) electron state, and k is the energy of the photon as mentioned previously. If the assumption that $\varepsilon_2 = \varepsilon_1 - k$ is made a form that is dependent only on the ratio $\kappa \equiv k/\varepsilon_1$ arises:

$$P = \frac{k\left(\varepsilon_1 + \frac{1}{3}(\varepsilon_1 - k)\right)}{\varepsilon_1^2 + (\varepsilon_1 - k)^2 - \frac{2}{3}\varepsilon_1(\varepsilon_1 - k)}$$

$$P = \frac{k\varepsilon_1 + \frac{k\varepsilon_1}{3} - \frac{k^2}{3}}{\varepsilon_1^2 + (\varepsilon_1 - k)^2 - \frac{2\varepsilon_1^2}{3} + \frac{2k\varepsilon_1}{3}}$$

$$P = \frac{\frac{4k\varepsilon_1}{3} - \frac{k^2}{3}}{\frac{4\varepsilon_1^2}{3} - \frac{4k\varepsilon_1}{3} + k^2}$$

$$P = \frac{4\kappa - \kappa^2}{4 - 4\kappa + 3\kappa^2}$$

This relation for photon polarization from circularly polarized coherent bremsstrahlung is used in the data analysis of this thesis.

2.5 Dynamic nuclear polarization

The technique for polarizing the free protons within the polarized nucleon target used in this work is called dynamic nuclear polarization (DNP). Dynamic nuclear polarization is the process of transferring the spin polarization of electrons in paramagnetic radicals, spread throughout the target mixture, to the nuclei of the target material. The target mixture must be brought down to a very low temperature (usually less than < 1 K) within a polarizing magnetic field. The magnetic field completely and uniformly polarizes the paramagnetic radicals in the mixture.

Once full polarization of the radical molecules is established, the target mixture is exposed to microwave radiation near the range of the known electron spin resonances of the paramagnetic radicals within the target. The electron spin resonance is defined by the width of the splitting in the energy levels of the paramagnetic material caused by the applied magnetic field. The nuclear spins can be polarized either parallel or anti-parallel to the magnetic field by using microwave frequencies either just above or just below the electron spin resonance frequency, or by reversing the magnetic field. An illustration of the simplified idea behind DNP is shown in Fig 2.2 [19]. The actual DNP process occurs through one or more of four mechanisms: The Overhauser effect, the solid effect, the cross effect, and thermal mixing. These are described in turn.

Overhauser effect

The groundwork for DNP was laid by Albert Overhauser during the mid-1950's. He proposed a method for polarizing nucleons within a metal by using the electron spin resonance of the conduction electrons. Through the interaction between the electron spin magnetic moment β_e and the nuclear spin magnetic moment β_n, via the hyperfine coupling of an *S* state, the polarization of a metallic material is possible. The polarization occurs when the metallic material is placed in a constant magnetic field Φ

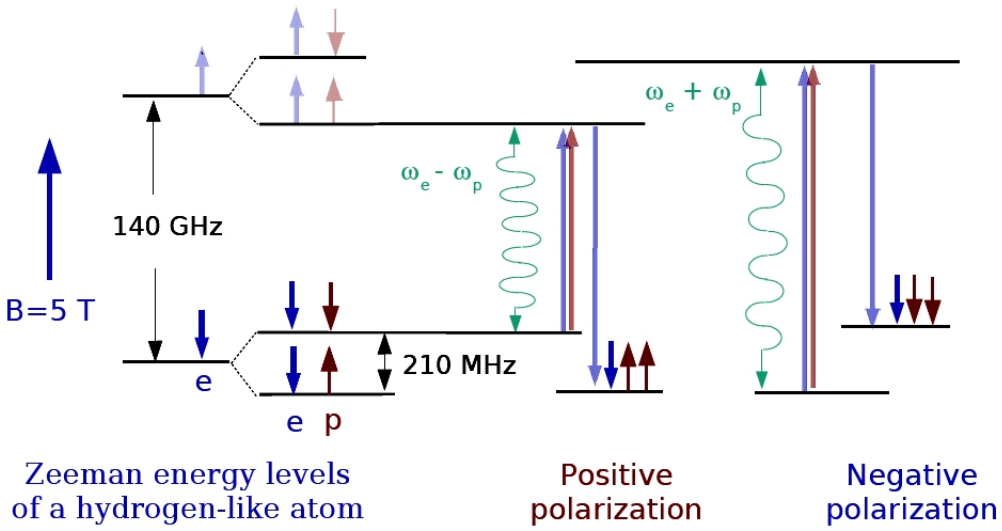

Figure 2.2: A simple model of DNP. The target material is first split into electron spin states by use of the applied magnetic field. These energy levels are further split based on the proton spin states, giving four total energy levels. The applied microwave radiation will be at one of two frequencies, $\omega_e + \omega_p$ or $\omega_e - \omega_p$. These two driving frequencies will cause a particular spin state combination to be flipped ($\downarrow\downarrow$ to $\uparrow\uparrow$ for a frequency of $\omega_e - \omega_p$ and $\downarrow\uparrow$ to $\uparrow\downarrow$ for a frequency of $\omega_e + \omega_p$). Meanwhile, the other spin states will be left to transition normally and so as the net result after enough time has elapsed is a majority of the material will have the desired polarization. The process shown here is very similar to the solid effect described in the text [7].

and is irradiated by a perpendicular microwave magnetic field which fits the resonance criteria: $\hbar\omega = 2\beta_e\Phi$, where ω is the resonance frequency. In order to return to an equilibrium state, the nucleons within the metal will begin to exchange spins with the electrons until equilibrium is achieved, thus polarizing the nuclei of the metal [20].

Solid effect

The solid effect builds on the framework of the Overhauser effect. The solid effect assumes that all the paramagnetic materials in a target mixture have spin $S_1 = 1/2$, a Larmor frequency of $\omega_{S_1} = \gamma_S B$, where γ_S is the gyromagnetic ratio $eg/2m$, and that the nuclei of the material to be used for scattering within the target material have spin of $S_2 = 1/2$ and Larmor frequency of ω_{S_2}.

Nuclear spins in the two materials are coupled to neighboring nuclear spins through dipolar interactions. Dipolar interactions are dipole-dipole interactions for two interacting nuclear spins, given by the equation

$$\mathbf{H} = -\frac{\mu_0}{4\pi}\frac{\gamma_j\gamma_k^2}{r_{jk}^3}\left(3\left(\mathbf{S}_j\cdot\mathbf{e}_{jk}\right)\left(\mathbf{S}_k\cdot\mathbf{e}_{jk}\right)-\mathbf{S}_j\cdot\mathbf{S}_k\right)$$

where $\mathbf{e}_{jk}$ is a unit vector parallel to the line joining the center of the two dipoles, r_{jk} is the spin-spin distance, and γ_j and γ_k are both gyromagnetic ratios of the two individual spins. The gyromagnetic ratio is the ratio of the magnetic dipole moment to the angular momentum. The dipolar interactions allow for the simultaneous switching of two spin states between S and L spins, $\Omega = \omega_{S_1} - \omega_{S_2}$ for spin reversals in the parallel spin configuration and $\Omega = \omega_{S_1} + \omega_{S_2}$ for spin reversals in the anti-parallel configuration, where Ω is the frequency of an external microwave source.

The microwave frequency applied to the target mixture is chosen either slightly above or below the Larmor frequency of the paramagnetic material, on the order of the electronic line width $\Delta\omega_S << \omega_{S_2}$. The requirement of $\Delta\omega_{S_1} << \omega_{S_2}$ effectively locks in the type of spin-flip which will occur due to the slight shift $\Delta\omega_{S_1}$ causing one of the possible interaction states, opposite or same direction, to be off resonance and thus a forbidden transition in the first order approximation. The key aspect of the solid effect for DNP is that the rate of nuclear relaxation for the scattering material through normal dipolar interactions is much less than the rate at which the exchange is driven by the applied microwave frequency. In an ideal situation, these dipolar interactions occur only with the paramagnetic material inside the target mixture. In principle, this process should allow for full polarization of all I spin states [21].

Cross effect

The cross effect follows from the solid effect by considering an impure paramagnetic mixture. This paramagnetic mixture contains multiple electron spin resonance

frequencies (also referred to as electron paramagnetic resonances) ω_{S_1}, $\omega_{S_1'}$ and $\omega_{S_1''}$ where $\omega_{S_1'} + \omega_{S_1''} = \omega_{S_2}$. Thus, nuclear transitions occur both through the driving microwave frequency, from the ω_{S_1} electron spin resonance, and from combinations of spin resonances from the other unpaired electrons from different paramagnetic materials ($\omega_{S_1'}$ and $\omega_{S_1''}$). The advantage to the cross effect as a DNP mechanism is in allowing for a broader electron spin resonance range based on the number and type of paramagnetic materials introduced into the target mixture [22].

Thermal mixing

The previous two sections assumed a very dilute mixture of paramagnetic centers. However, most modern target materials have a very high fraction of such centers. This results in more complex phenomena than these simple cases.

Thermal mixing is the coupling of a thermal spin reservoir with the electronic Zeeman interaction under off-electronic-resonance microwave radiation and spin-lattice relaxation. The target mixture, from a thermal mixing point of view, contains three thermal reservoirs: the nuclear Zeeman reservoir, the electronic Zeeman reservoir, and the electronic non-Zeeman reservoir. The applied microwave frequency causes a change in the non-Zeeman electronic energy. This non-Zeeman reservoir is in close thermal contact with the nuclear Zeeman reservoir through thermal mixing, which allows their common spin temperatures to evolve together based on the applied microwave frequency. A frequency shifted above the Larmor frequency will produce a positive spin temperature value while a shift below will produce a negative spin temperature value. The electronic Zeeman reservoir has a much faster relaxation time associated with it due to the difference in heat capacity between it and the linked nuclear Zeeman and electronic non-Zeeman reservoirs. At this point, the process becomes similar to the solid effect as the difference in relaxation times allows for the full polarization of the scattering material in the target mixture [23].

Almost all DNP target materials utilize thermal mixing as the primary mechanism for the DNP process, although a few materials use a combination of both thermal mixing and cross effect. The TEMPO-doped butanol in the target used in this experiment uses thermal mixing as the main driving mechanism for DNP.

Chapter 3

EXPERIMENTAL APPARATUS AND TECHNIQUES

A polarized target, when coupled with a polarized photon beam, allows for measurements of double polarization spin observables such as the helicity asymmetry E, described in detail in Chapter 2. This chapter provides the technical details of the apparatus used for the measurements made in this work. All data for the Frozen Spin Target (FROST) experiment were obtained using the equipment in the John J. Domingo Experimental Hall B at JLab, and the Continuous Electron Beam Accelerator Facility (CEBAF). Located within Hall B is the CEBAF Large Acceptance Spectrometer (CLAS), a detector primarily sensitive to charged particles.

For this work, the recoiling proton from the reaction $\gamma + p \rightarrow p + \eta$ was detected in CLAS. With this two-body final state, a missing mass reconstruction can be used to detect the η meson using knowledge of the photon energy E_γ and recoil proton information alone. In order to properly reconstruct the missing mass of the η, the four-vector momentum for the incident photon and for the recoil proton must be known. The information for the photon comes from the Hall B Bremsstrahlung Tagging Facility ("tagger"), and the initial proton within the cryogenic target is considered to be at rest. With the information from the CLAS drift chambers, the three-vector momentum $\vec{p}$ of each particle detected can be determined which, when coupled with the timing information from the time-of-flight system (ToF), permits a full reconstruction of the four-momentum for each charged particle detected in CLAS.

3.1 The Continuous Electron Beam Accelerator Facility (CEBAF)

CEBAF at JLab is a superconducting radio-frequency (RF) electron accelerator capable of accelerating electrons to energies up to 6 GeV. Figure 3.1 shows an aerial photograph and schematic drawing of the accelerator. CEBAF utilizes a strained

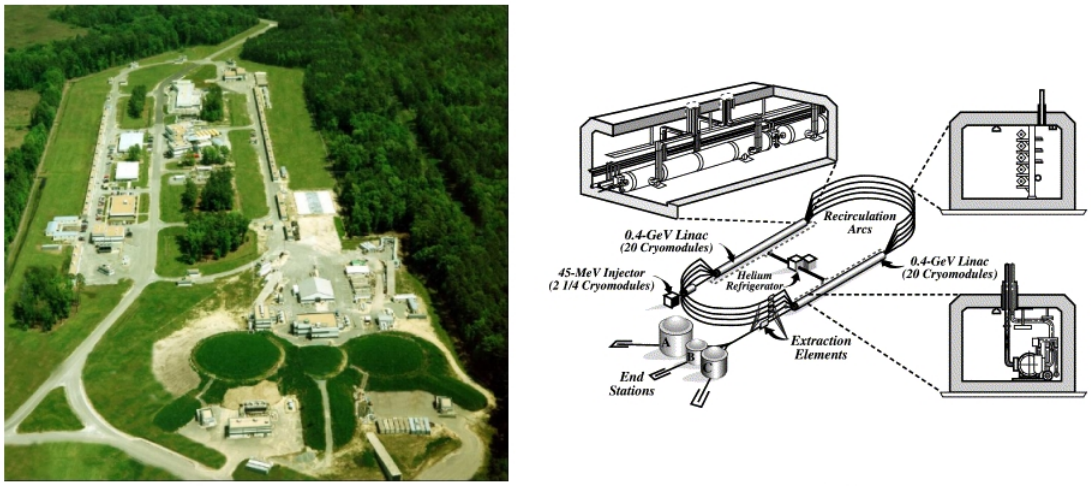

Figure 3.1: (A) The Continuous Electron Beam Accelerator Facility (CEBAF) and experimental halls seen from the air. (B) A schematic drawing of the interior of the accelerator, showing all major structures [8].

gallium-arsenide photocathode gun electron source that can deliver longitudinal electron beam polarizations up to 85% while still providing current simultaneously to all three experimental halls. In general, Experimental Halls A and C require beam currents on the order of a μA while Experimental Hall B, the experimental hall where the FROST experiment was performed, requires a beam current on the order of 10 nA due to the high event and data rates of data generated by the large solid angle CLAS detector.

As can be seen in Figure 3.1, the general shape of the accelerator is similar to a racetrack, with electrons entering from the injector via an RF chopping system.

The injector consists of two electron guns, a thermionic gun and a polarized gun. The polarized electron gun was used for this experiment. The polarized electron gun produces polarized electrons by illuminating a strained GaAs cathode with a 1497-MHz gain-switched diode laser operated at 780 nm. The polarization of the electrons is measured at the injection point using a 5-MeV Mott polarimeter. The polarization angle can be oriented with a Wein filter [24].

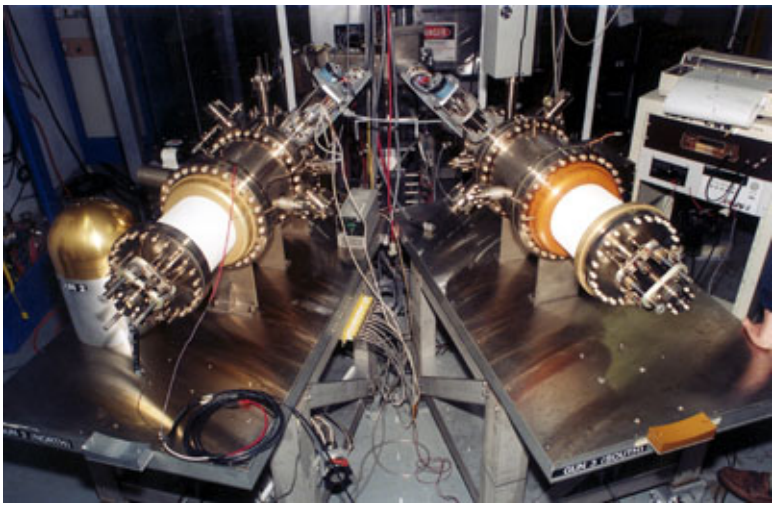

Figure 3.2: The two electron guns used in the injector [8].

Once injected, the electrons travel around the "racetrack" a fixed number of times before being fed into an experimental hall. The track is composed of two linear accelerators, each consisting of 338 superconducting radio frequency niobium cavities distributed in 21 "cryomodules". Two 180° arcs with a radius of 80 m complete the circuit between each linear accelerator. Each of the cryomodules consists of four sets of paired niobium cavities; these cavities were aligned and referenced to eight permanent external fiducials (the fiducials are objects used in imaging systems as a point of reference) along with four or five temporary fiducials that are glued in place [25]. The cavities are kept at approximately 2 K to sustain superconductivity through use of the liquid helium supply produced on site at the Central Helium Liquifer facility. Each of these arcs contains five possible paths for the beam to follow depending on beam energy, with the beam being bent into the proper track based on its present energy by a system of magnets consisting of a series of quadrapoles and dipoles that steer and focus the beam. In total, there are over 2,200 magnets associated with the accelerator [26].

The accelerator beam chopping system uses a frequency of 499 MHz to split the electron beam into a three-beam-bunch train, and then puts this stream of electrons through a longitudinal compression to achieve a 2 ps bunch structure. This structure allows each experimental hall to receive a beam with the desired energy and current requirements. The beam energy is constrained based on the initial electron beam energy produced by the CEBAF injector and the number of times the beam goes through the linear accelerators. Each pass around the racetrack increases the beam energy. A maximum of five passes around the track are possible to obtain a maximum beam energy of nearly 6 GeV. Each experimental hall determines the number of passes necessary for their desired beam energy based on the knowledge of what the linear accelerators are currently delivering to other halls. Once the electrons are accelerated to the desired energy they are then fed into an experimental hall at the beam switchyard. Table 4.1 provides the specific beam energies used during the running period for this experiment.

3.2 The Hall B Bremsstrahlung Tagging Facility

Hall B experiments for which a photon beam is required use the tagged bremsstrahlung method of creating and identifying the photons. The bremsstrahlung photons are generated by the electron beam delivered by CEBAF impinging on a thin target (called the "radiator"). The process of creating and identifying the photons is performed by the photon tagging system (tagger), shown in Figure 3.3. The tagger consists of an upstream radiator followed by a magnetic spectrometer. The magnetic spectrometer is used to determine the energy of the post-bremsstrahlung electrons.

The radiator for the tagger is often a thin foil, but is replaced with a diamond crystal for coherent bremsstrahlung experiments. Radiators with different thicknesses can be moved into position to change the intensity of the photon beam. Radiator changes are made using hardware controlled by the software running in the counting

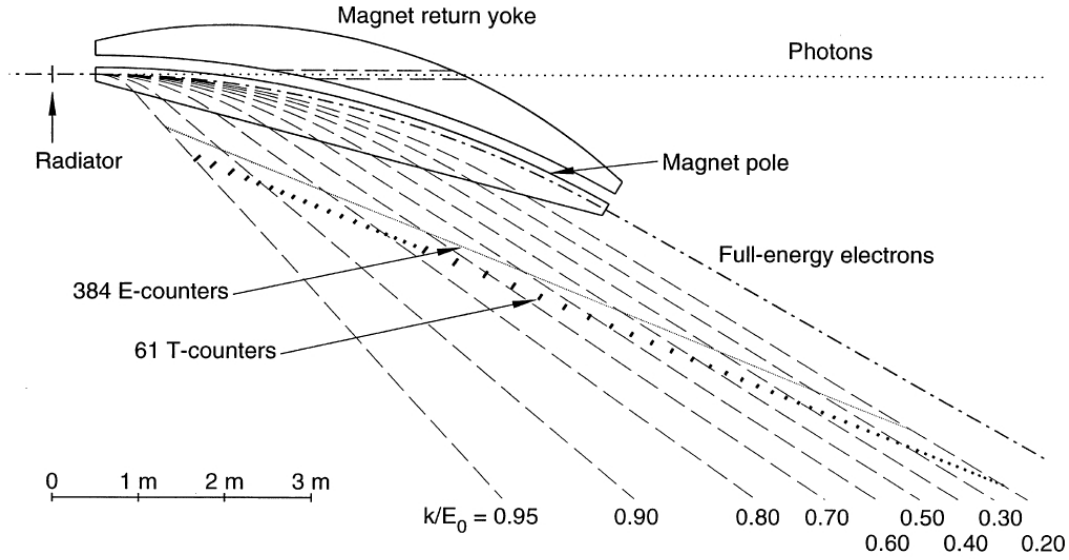

Figure 3.3: The bremsstrahlung photon tagging system (tagger) that is used in Hall B for photon beam experiments. As can be seen, the electrons enter from the left, are scattered off the radiator, and then "tagged" while the photons go down stream through the collimator [9].

house, This software will be discussed below. The radiator can also be completely removed to take reference runs in order to verify proper electron beam alignment.

Once the electrons in the electron beam strike the radiator, the electrons experience bremsstrahlung and emit a photon in the forward direction with a characteristic angle $\theta = m_e/E_e$, where E is the energy of the electron that radiated a photon with respect to the incident electron beam direction. This bremsstrahlung, or "braking" radiation, is caused when a charged particle (in this case an electron) undergoes an acceleration that is collinear to its velocity. In this braking process, the electron emits a photon such that energy and momentum are conserved. Simple Feynman diagrams of the bremsstrahlung process are shown in Figure 3.4. A more detailed explanation of the bremsstrahlung process was given in Chapter 2, Section 3. The momentum transferred to the nucleus is negligibly small, so that the process effectively obeys $E_\gamma = E_0 - E_e$, where E_0 is the incident electron energy determined by

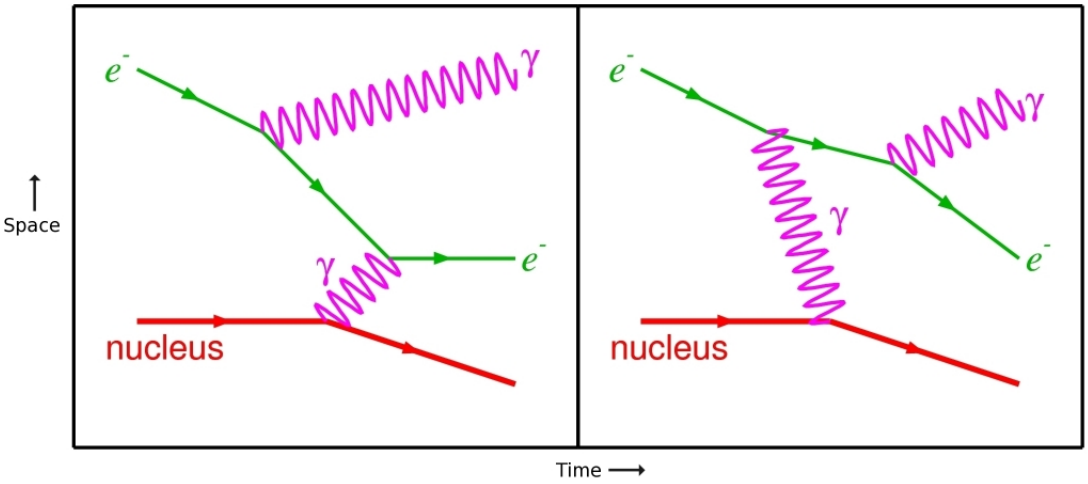

Figure 3.4: A simple Feynman diagram of the bremsstrahlung radiation that occurs when the electron beam is incident on the radiator in the tagger. The diagram on the left shows the case where the emitted photon originates before the virtual photon is exchanged, whereas the diagram on the right shows the case where the emitted photon originates after the virtual photon.

the accelerator facility, E_e is the energy of the electron following bremsstrahlung, and E_γ is the energy of the emitted photon. The number of photons emitted is inversely proportional to E_γ.

The trajectory of each electron in the incident beam is bent downward by a magnetic field towards a series of scintillators located in a sealed vacuum enclosure below the beam line. One set of scintillators, the energy counters (or "E-counters"), form the focal plane of the spectrometer. These E-counters, along with timing counters ("T-counters") spaced out below them as shown in Figure 3.3, are used to "tag" the photon that is produced, giving accurate energy and timing for the event. By overlapping the coverage of adjacent counters, the E-counters divide the full energy acceptance of the tagger into 767 photon energy bins. If the electron does not radiate a photon, the magnetic field is such that the electron beam will be bent directly into a beam dump located at the end of the tagger structure. If the electron does radiate a photon, that electron will be bent in an arc downwards, with less energetic electrons

(which have yielded more energetic photons) being bent more. Based on where the electron strikes the focal plane, the energy of the scattered electron is determined, and the energy of the photon emitted is computed.

The photon beam goes through a collimator further downstream to define the size and shape of the photon beam. Associated with the collimator are a magnets that eliminate the charged particle background produced when the beam is collimated, which arises when the photon strikes the collimator walls, by bending the paths of the charged particles away from the photon beam. Once past the collimator, the photon beam proceeds to the target, located in the center of CLAS, with a well-determined energy and direction. With 767 energy bins the resolution for the tagger is on the order of $10^{-3}E_0$, with a tagging range of 20 to 95% of E_0. The T-counters give a timing resolution for events better than 300 ps [9].

3.3 Targets

There are three meson production targets for this experiment: the FROST target, a graphite (carbon) target, and a polyethylene (CH_2) target. The carbon target is used to simulate the bound nucleon background in butanol; data taken on that target can be used to subtract the bound contribution from the butanol target.

Previous polarized targets were limited to longitudinally-polarized nucleons, and permitted scatterings of angles up to 55° from the beam. The Frozen Spin Target produced at JLab is capable of being both longitudinally and transversely polarized, reaching free proton polarization values over 80% at a base temperature of 28 mK. During running times, FROST had relaxation rates of 0.9% per day for positive polarization and 1.5% per day for negative polarization. Target polarization is determined by performing an integration of the peak in the NMR spectra for a voltage-versus-frequency-deviation plot and the sign is pulled from the run database. The peak area in this plot is multiplied by a calibration constant to give the final

polarization. This constant is determined by calculating the polarization from the equation

$$P = tanh\left(\frac{\mu \mathbf{B}}{kT}\right)$$

The constant is $\tau = P/A$, where A is the area from the voltage versus frequency plot. This calibration constant is set early in the controlled stages of the setup, and the ratio is assumed to hold for the entire running period.

The design for FROST is shown in Figures 3.5 and 3.6. As can be seen in Figure 3.6, FROST is composed of a series of nested cylinders consisting of three total targets, two heat shields, a target cup, a mixing chamber, and solid foam exterior shell. The main target is a mixture of supercooled butanol (C_4H_9OH) beads, immersed in liquid helium, filling the entire target cup. To create these beads, the butanol is doped with the paramagnetic TEMPO ($C_9H_{18}NO$), a necessity for the dynamic nuclear polarization process, and then supercooled in liquid nitrogen, causing the formation of the beads as the butanol freezes. This process is regulated to produce consistent 1.5

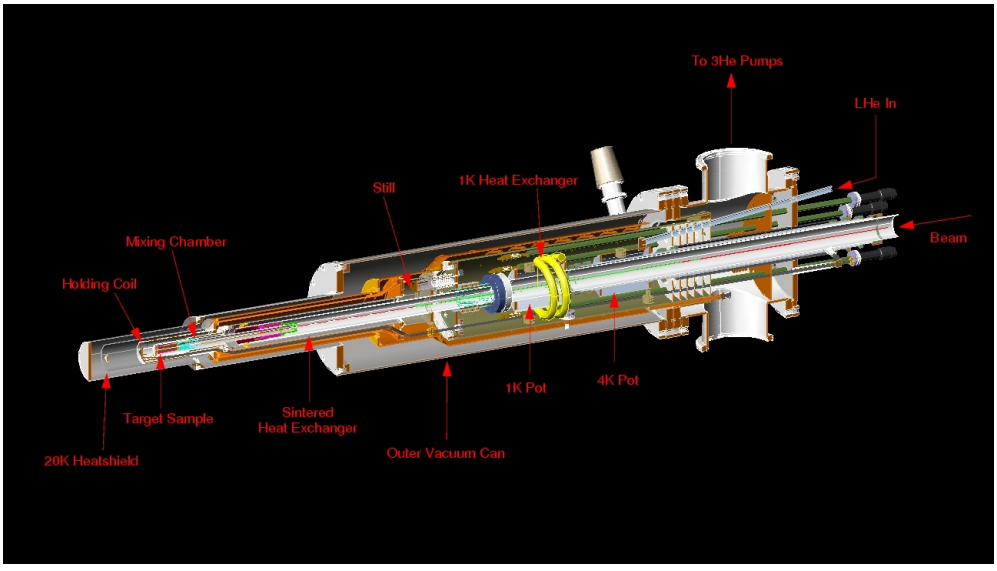

Figure 3.5: The FROST target used in this work [7]. The actual butanol target portion is located on the far left end in the mixing chamber.

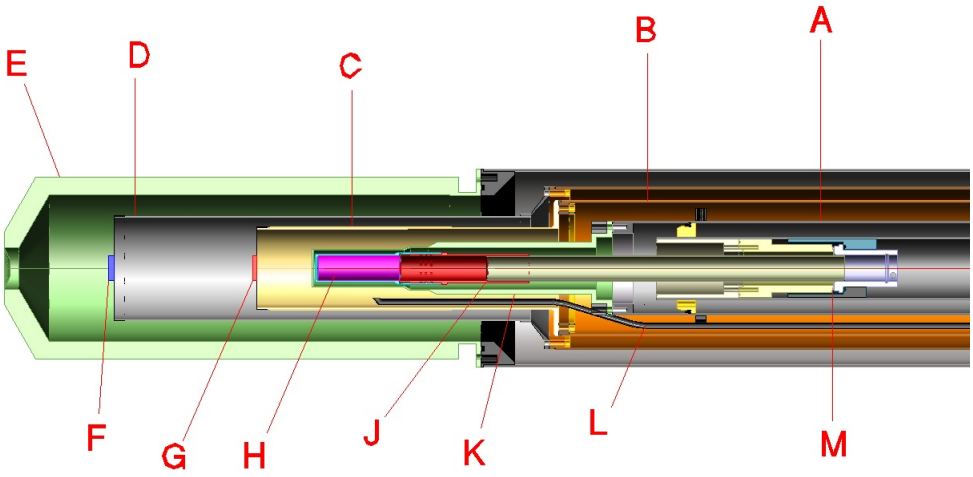

Figure 3.6: A cross section of the target area of FROST: *a)* primary heat exchanger; *b)* 1 K heat shield; *c)* holding coil; *d)* 20 K heat shield; *e)* outer vacuum can (Rohacell extension); *f)* polyethylene target; *g)* carbon target; *h)* butanol target; *j)* target insert; *k)* mixing chamber; *l)* microwave waveguide; *m)* kapton coldseal [10].

mm diameter beads. One step of the freezing process for the butanol beads is shown in Figure 3.7. Downstream from the main target, on the end caps of the 1 K heat shield/holding coils and the 20 K heat shields, are the carbon and polyethylene targets used for background measurements.

The butanol beads are polarized using the dynamic nuclear polarization technique described in Chapter 2. This process is performed at 0.3 K by placing the butanol mixture into a 5.0 T polarizing magnet. These conditions caused a nearly complete polarization of the paramagnetic radicals within the butanol mixture. While in this condition, a microwave field is applied to the mixture to transfer the spins from the free radicals to the free nucleons within the butanol. When the overall polarization of the free nucleons within butanol reaches approximately 90%, the microwave generator was turned off. The spins were then "frozen" in place by cooling the entire target to 30 mK.

Figure 3.7: The target cup coming out of the liquid nitrogen submersion filled with butanol beads and ready to be placed in the target [7].

The cooling process for the butanol was accomplished with a ^{3}He/^{4}He dilution refrigerator. Below 0.8 K, a ^{3}He/^{4}He mixture will separate into two phases: a dilute phase and a concentrate, with the concentrate sitting atop of the dilute. At very low temperatures, the ^{3}He behaves as a gas of spin-1/2 particles, and will absorb thermal energy. The two phases of the ^{3}He/^{4}He mixture also have different specific heats, 106 J/(mol·K) for dilute and 22 J/(mol·K) for the concentrate. Removing the ^{3}He from the lower part of the mixing chamber, where the dilute phase lies, causes the top portion to absorb the heat from its surroundings to maintain thermal equilibrium as a portion of the concentrate transitions to the dilute phase. Since the target beads are submerged in

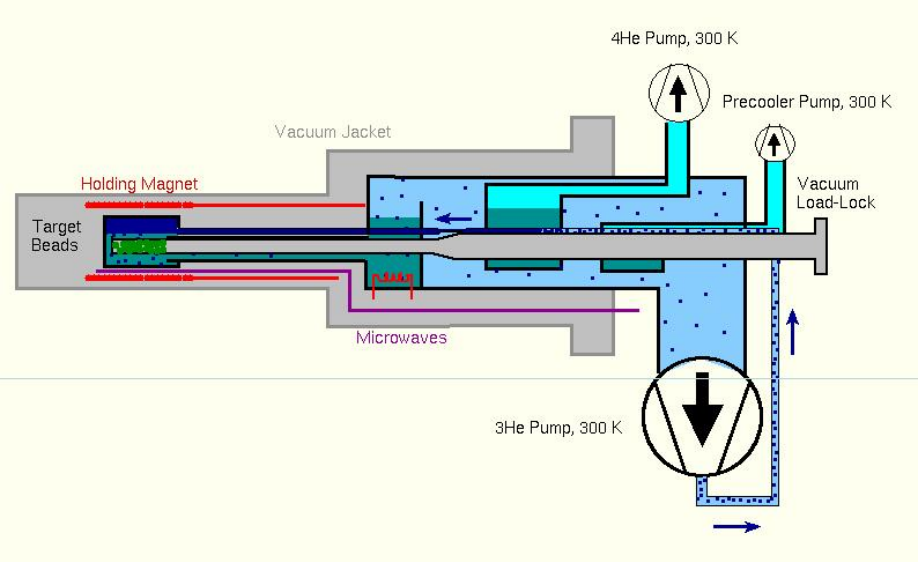

Figure 3.8: An illustration of the operation of the dilution refrigerator for FROST. ^{3}He is pumped from the chamber, causing the ^{4}He to absorb heat from the surroundings, most notably the butanol beads, in order to maintain thermal equilibrium, as part of the ^{4}He is converted over to the dilute phase [7].

this ^{3}He bath, the beads will be the main source for this thermal transfer to maintain equilibrium. This process is implemented around FROST as shown in Figure 3.8.

At the nominal 30 mK temperature, a "holding field" of only around 0.55 T is required to effectively freeze the target polarization, with less than 2% decay in polarization per day. The superconducting solenoid magnet used for this is sufficiently thin that, while producing the desired field, a charged particle was able to pass through the magnet with only minor effects on the four-momentum of the particle. The DNP process was repeated every 5 to 10 days, usually flipping the target polarization when undergoing the re-polarization process [27].

The carbon target was placed on the end cap of the 1 K heat shield/holding coils layer and was 1.49 ± 0.01 mm thick. Butanol is composed of a large percentage of bound nuclear protons: four carbon nuclei - giving 24 bound protons - and one oxygen nucleus - providing another eight bound protons - and only 10 free protons

from the hydrogens. This means that around 76% (i.e. 32/42) of the nucleons in butanol are bound content. On the downstream end cap of the 20 K heat shield, the polyethylene target is mounted; the polyethylene target is 3.45 ± 0.01 mm thick. The polyethylene target consists of six bound nucleons and two free nucleons. This gives the polyethylene target 75% bound content. Because of this, the polyethylene target will produce a signal similar to the butanol target, but on a much smaller scale due to the size of the polyethylene target and its position in the beam line.

3.4 Start counter

In order to properly associate the particles recorded in CLAS with the tagged photon for an event, a detector is used in photon experiments to determine the time of passage of a charged particle into CLAS. This ”start counter”, as seen in Figure 3.9, surrounds the target in CLAS and is placed in logical coincidence with the tagger as part of the event trigger.

The start counter has six identical sectors, matching the six-sector geometry of the CLAS enclosure. Each of these sectors contains four scintillators, giving a total of

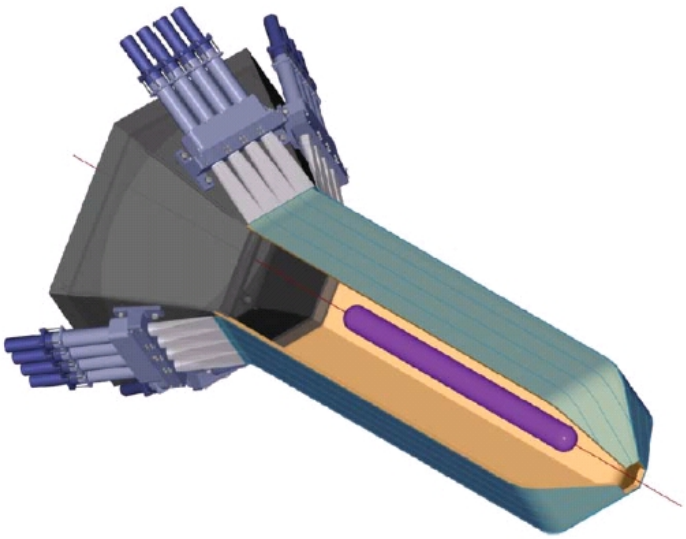

Figure 3.9: A rendering of the start counter used during the g9a running period. The six sector structure matching that of class is clearly visible in the geometry [11].

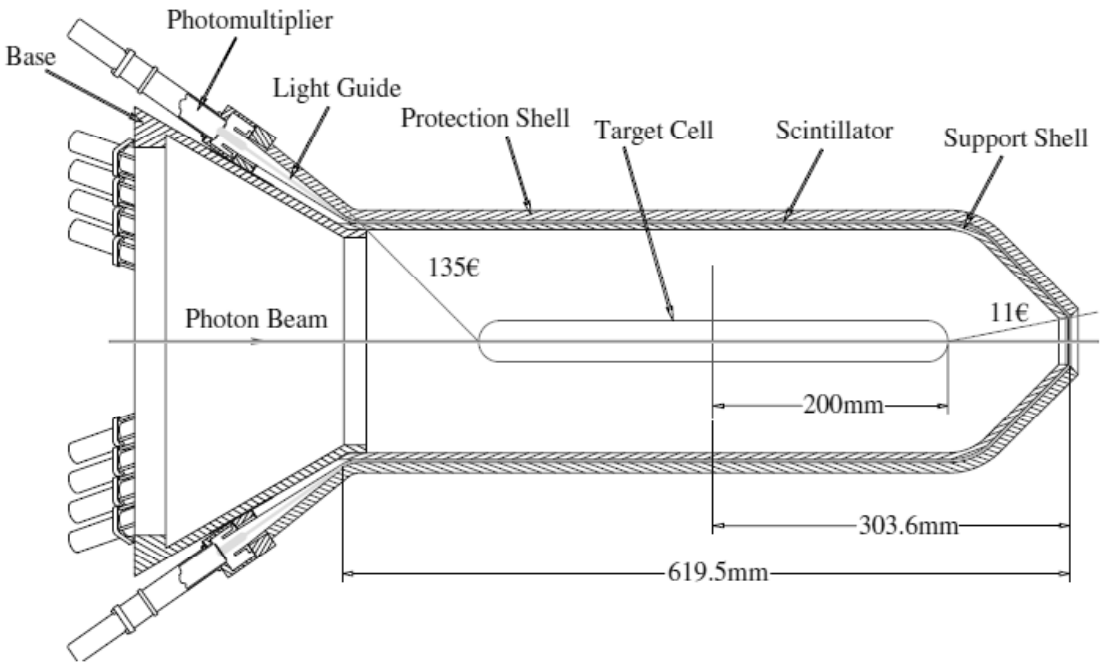

Figure 3.10: A cross section of the start counter. Shown in the center for reference is the target [11].

twenty-four counters for the entire structure. The scintillators in the start counter are 50.2 cm long, 2.9 cm wide, and 0.215 cm thick, with each scintillator being coupled to a photomultiplier tube.

This counter is capable of providing a fast timing signal ($\sim$25 ps) for the CLAS trigger that, when coupled with the information from the tagger and time-of-flight systems, can be used to greatly reduce the accidental trigger rate and also helps determine information about the charged particles, such as their velocities when combined with information from the time-of-flight system in CLAS. When compared to the RF time, the start counter gives the start time of the particle trajectory to better than 25 ps accuracy [11].

Figure 3.11: The CEBAF Large Acceptance Spectrometer. The time-of-flight clamshells are exposed in this image, showing the drift chambers surrounding the target enclosure [8].

3.5 The CEBAF Large Acceptance Spectrometer

The CEBAF Large Acceptance Spectrometer (seen in Figure 3.11) is a detector with a detection solid angle of nearly 4π sr used to detect charged and neutral particles. The detector acceptance is somewhat less than 4π sr because the superconducting magnetic coils are located between the drift chambers, and there is also a downstream line exit of about 10° in the forward direction. When restricting event analysis to regions where CLAS detection efficiency is relatively uniform, the acceptance falls to around 2π sr.

The momenta of charged particles passing through the toroidal magnetic field can be measured with a resolution that varies with angle. The fractional momentum resolution $\Delta p/p$ varies between 3% and 5%. The detector has a central magnetic-field-free region for targets, including complex targets such as FROST [13].

CLAS is formed into six ideally-identical magnetic spectrometers that are effectively independent of each other, arrayed in a hexagonal geometry. The magnetic field in the detector is produced by six superconducting coils which define the six sectors. The coils are arranged around the beam line in such a way as to produce a field primarily pointing in the ϕ-direction, azimuthal to the z-direction along the photon beam path.

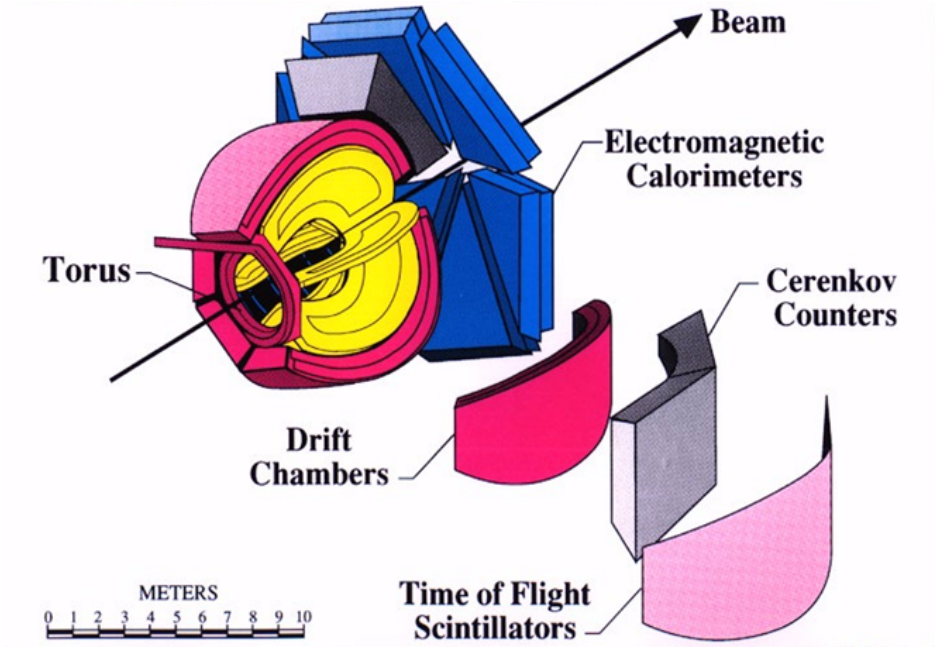

Figure 3.12: The CLAS detector subsystems [8].

The detector consists of several subsystems. Drift chambers are used for trajectory determination, Čerenkov counters for differentiating electrons from pions and triggering for electron runs, scintillation counters for time-of-flight information, and electromagnetic calorimeters to detect neutral particles. These subsystems can be seen in Figure 3.12, and will discussed here in turn.

3.5.1 Drift chambers subsystem

Each sector of CLAS includes three sets of drift chambers for tracking and trajectory determination. The curvature of the trajectory gives the sign of the charge of the

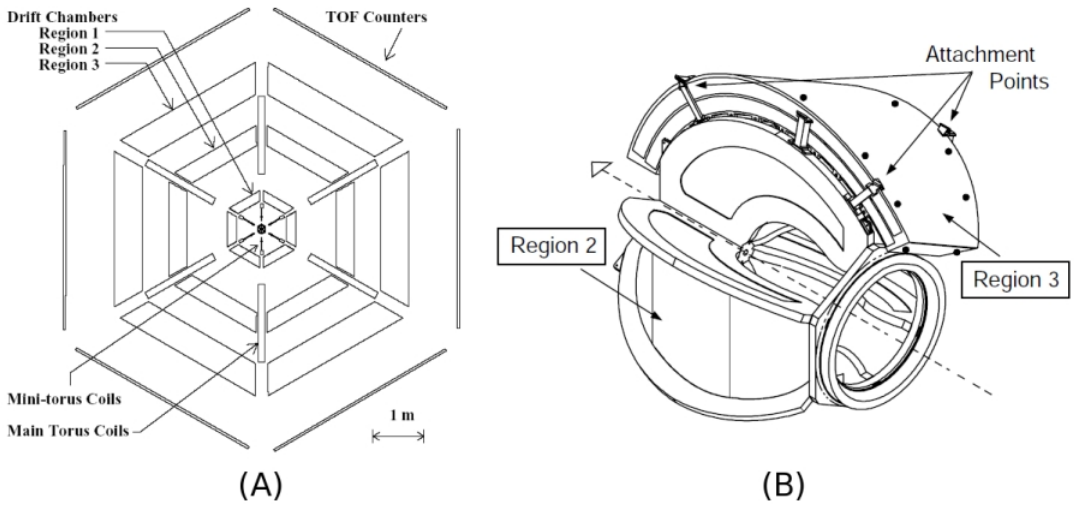

Figure 3.13: (a) A vertical cross section of the class subsystems showing the arrangement of the three drift chamber regions in relation to the beam center and the time-of-flight counters. (b) The interior layout of one of the six drift chamber sections [12].

particle q, and the radius of curvature R. The magnetic field B is known from field maps and knowledge of the supplied current, so the momentum p can be determined from the relation $p = qB/R$.

In total, each sector has 18 drift chambers arrayed in three different regions, with each region containing six drift chambers, as shown in Figure 3.13. Region 1 (R1) surrounds the target in the low magnetic field area. Region 2 (R2) is larger and placed within the area of highest magnetic field. Region 3 (R3), by far the largest, is placed outside the magnetic field outer boundary. The combination of these three drift chamber sets allows for trajectory ("track") reconstruction when particles hits are registered in multiple regions, along with a hit in the start counter and time-of-flight counters. Particle hits refers to the detection of a charged particle in a particular wire and are used for "hit-based" tracking, which is the method of combining the segments between each "hit" into the overall track the particle took.

The drift chambers are composed of wires stretched between two end plates. These wires consist of field wires and sense wires, with a repeating pattern of two field

wire layers and then one sense wire layer to form a quasi-hexagonal pattern, with each sense wire being surrounded by six field wires. These groupings of wires are called "superlayers," with each superlayer consisting of two sets of the field and sense wire patterns, as shown in Figure 3.14. Regions R2 and R3 consist of two sets of superlayers for redundancy in tracking, one being axial to the magnetic field and the other being tilted at a 6° stereo angle. Region 1 is limited to only four layers of wires in the stereo superlayer due to the space constraints from its proximity to the target.

As constructed, with the size and spacing of the wires in each region, the momenta for charged particles can be reconstructed with a resolution of $\Delta p/p$ = 3% to 5% [12].

3.5.2 Time-of-flight subsystem

When combined with timing information from the start counter, the ToF subsystem measures the transit time for charged particles passing through the magnetic field region of a given sector. When coupled with the tracking information from the drift chamber system, the track length can be found, from which the velocity $\beta = v/c$ can be determined. Once β and p are found, the mass of the particle can be calculated, and thus particle identification made (i.e. pion, proton, kaon, etc.). The time-of-flight scintillators surround the entire active area inside CLAS containing scintillating

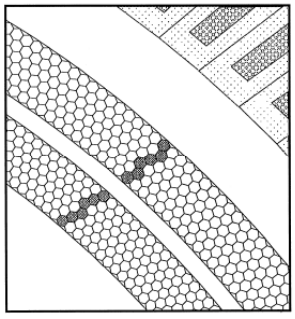

Figure 3.14: A representation of the wire layout in the R3 wire superlayers. The sense wires are at the center of each hexagon and the field wires are at the vertices [12].

materials and drift chamber wires, covering laboratory scattering angles from 8 to 142°. The total coverage area of the ToF system is 206 m^2.

The time-of-flight (ToF) counters are located after the Region 3 drift chambers but before the electromagnetic-calorimeter. ToF counters are plastic scintillator counters coupled to photomultiplier tubes, and read out using time-to-digital converter boards along with amplifier and discriminator boards, giving a record of positions and passage time as a charged particle leaves CLAS. Timing resolution of the ToF counters is 120 ps at the smallest scattering angles and 250 ps at the largest angles (above 90 degrees). These counters also serve as neutron detectors, with a 5% neutron detection efficiency.

The scintillators themselves are mounted in four panels in each of the six sectors and have a uniform thickness of 5.08 cm. The first 23 scintillators are located on panel one and cover scattering angles of less than 45°; this set is referred to as the "forward-angle" counters. The remaining time-of-flight counters are located on the other three panels, and are called "large-angle" counters. The "forward-angle" counters have a width of 15 cm due to space constraints while the "large-angle" counters have a 22 cm width. Each scintillator is placed approximately perpendicular to the incident beam so as to subtend approximately 2° of the scattering angle [28].

3.6 The Čerenkov counters subsystem

The Čerenkov counters serve as a means of separating electrons from pions in CLAS. The counters are designed such that they are minimally intrusive to the rest of the CLAS sub-systems. Light collection cones and photomultiplier tubes are placed in areas already obscured by magnetic coils while covering as much area as possible with the use of mirrors as shown in Figure 3.15. The Čerenkov counters are only utilized for very forward going angles and as such are designed to cover up to a 45° laboratory scattering angle [13]. Because FROST is a photon beam experiment, these counters

were turned off for the entirety of the running period and will not be discussed further.

3.7 The electromagnetic calorimeter subsystem

The forward electromagnetic calorimeter subsystem detects electrons with energies above 500 MeV, photons with energies above 200 MeV, and also detects neutrons. Similar to the Čerenkov counters, the electromagnetic calorimeter subsystem covers laboratory scattering angles from 0 to 45°. The calorimeters are constructed of alternating sheets of scintillator and lead. Each sheet of scintillator is 10 mm thick and is followed by a sheet of lead 2.2 mm thick. Each electromagnetic calorimeter consists of 39 of these layers, roughly shaped into an equilateral triangle, as shown in Figure 3.16. There are six electromagnetic calorimeters, matching the CLAS sector geometry.

The large angle calorimeters are used for detection of scattered electrons and neutral particles at large laboratory scattering angles, from 45°-75°. The large angle calorimeters cover only two of the six CLAS azimuthal sectors. The construction of the large angle calorimeters is similar to that of the forward ones with layers of scintillator and lead sheets. The large angle calorimeters have 33 layers, with 2 mm thick lead sheets and 15 mm thick scintillator bars, with the bars rotating by 90 degrees in subsequent layers. Teflon sheets, of 0.2 mm thickness, separate each of the neighboring scintillators. The detection efficiency for the large angle calorimeters is around 95% for 2 GeV electrons [13].

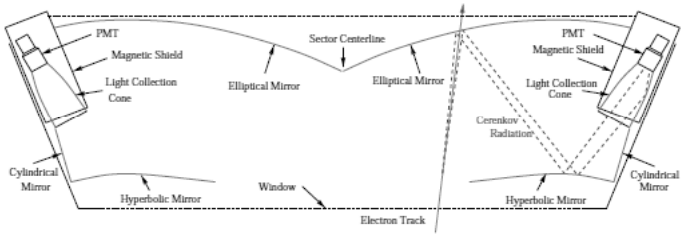

Figure 3.15: An illustration of how the Čerenkov counters are set up and utilize mirrors to capture information while being minimally invasive [13].

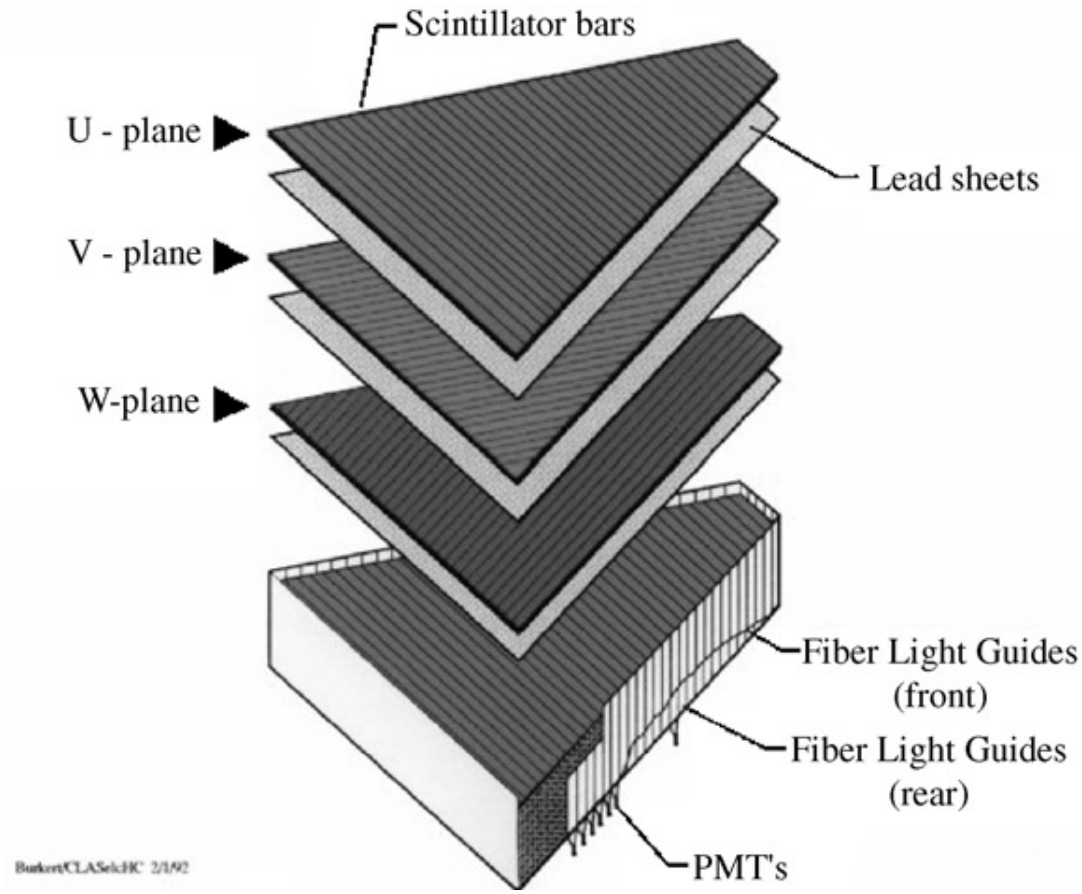

Figure 3.16: The layering of the scintillator and lead sheets for each electromagnetic calorimeter. The U, V, and W planes represent different groupings of wire orientations, each 120° off from the previous plane and spanning 13 layers [13].

3.8 The event trigger

An event trigger is the logical combination of conditions that indicate an event of interest has occurred. This logic condition is realized through a combination of electronic modules that take logical signals from the various subsystems of CLAS.

The electronics logic for this experiment utilized two specific event triggers, a Level 1 trigger (L1) and a Level 2 trigger (L2). The L1 trigger for the FROST experiment required a coincidence between the start counter and ToF scintillators within the same sector. The L2 trigger for FROST required that, in the same sector as

the L1 trigger, three out of the six superlayers in the drift chambers recorded track segments. If an event did not pass the L1 trigger, nothing was recorded for that event, and an L2 trigger was ignored. Likewise, without an L2 trigger, the event was not recorded. If both an L1 and L2 trigger occurred, then information for the event was acquired by the data acquisition system as a CLAS event for final analysis. These two conditions meant that at least one sector had at least one charged particle that could be reconstructed.

3.9 Software for control and data acquisition

The software monitoring systems for all CLAS and CEBAF subsystems utilize the Experimental Physics and Industrial Control System (EPICS) software environment. These EPICS systems gather information necessary for the experimental hall to remain functional. The software is a GUI-based system run on the computers in the counting house located above the experimental hall, but also can be accessed through a secure connection from outside computers.

EPICS controls configuration settings and permits remotely resetting experimental components in the hall, as well as running performance scans on the different subsystems of CLAS without stopping a run.

Tied closely to the EPICS software is the data acquisition system (DAQ). The DAQ software system handles incoming signal information from all CLAS subsystems, and processes those signals to data files written to disk in the main computer center. The DAQ runs three main processes while collecting the data: (1) the Event Builder, which reconstructs the events from the subsystems; (2) the Event Transport, which manages shared memory for all events reconstructed with Event Builder; and (3) the Event Recorder, which picks up the data generated by the Event Builder system and writes the data in a single stream to disks. The average event rate for the DAQ during the FROST running period was around 4.5 kHz.

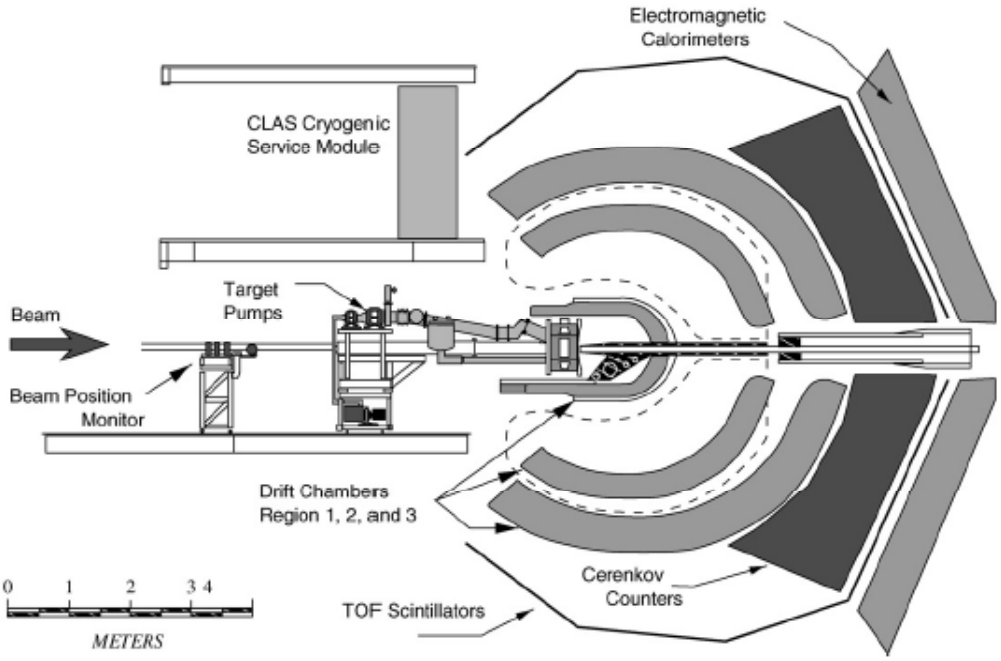

Figure 3.17: A cross section of the CLAS detector, illustrating target position, incoming beam, and target related equipment. The event originates within the target and will propagate outwards through the different sub-systems of CLAS, and the information registered in these sub-systems is used to reconstruct four-momentum and missing masses of charged and neutral particles [8].

3.10 Summary

The measurements of polarization observables for this work required the use of both a circularly-polarized photon beam and very-low-temperature polarized target. The polarized photon beam was generated with well-determined energy and time information using the Hall-B tagged bremsstrahlung facility. That tagged polarized photon beam was then incident on FROST. FROST was surrounded by the start counter and CLAS, as seen in Figure 3.17. Both L1 and L2 triggers were required for an event to be recorded as a CLAS event. The combinations of drift chambers, time of flight counters, and start counter readings were used for measurement of four-momentum for charged particles registered in CLAS. This information, when

coupled with that from the tagger, allows for reconstruction of the missing mass spectra for the reactions examined in this work, as discussed in the next chapter.

Chapter 4

DATA ANALYSIS

4.1 Overview of technique

For this thesis, the analysis of η photoproduction on the proton uses a missing mass reconstruction technique, which assumes a photon interacting with a free proton in the initial state and a $p+X$ final state, with M as the determined missing mass for the missing particle X. For topologies where pions are required, a secondary missing mass calculation for reactions of the type $\gamma + p_i \rightarrow p_f + \pi^{\pm}(+\pi^{\mp}) + X'$ is used to restrict the yield from the missing mass on the recoil proton, with M' as the determined missing mass for the particle X'. The topologies using a kinematic restriction involving a secondary missing mass calculation required a combination of π^+ and/or π^- detected in coincidence with the recoil proton within CLAS, as well as having all detected particles linked to the same generating photon in the bremsstrahlung tagger.

Numerator and denominator yields for the helicity asymmetry E, as defined in Chapter 2, were formed using additional information described later in this chapter. The missing mass spectrum for both numerator and denominator yields for the reaction $\gamma + p \rightarrow p + X$ were then fit in the range of the η meson mass with a combination of a polynomial and a Gaussian. The polynomial was then subtracted from the mass spectrum to determine the meson yield. Once yields were extracted for both numerator and denominator missing mass reconstructions, the observable E was constructed by dividing the numerator by the denominator.

4.2 Details of the technique

The process used to create the E observable from the raw data is as follows:

- Identify the subset of runs that are stable and contain data usable for η photoproduction analysis.

- Identify the charged particle tracks (proton, π^+, and π^-) within the data, and determine the momentum and angle of each particle.

- Apply energy, momentum, and trigger efficiency corrections to each charged particle.

- Reconstruct the missing mass M_X assuming a two-body reaction $\gamma + p_i \rightarrow p_f + X$, and also the reaction $\gamma + p_i \rightarrow p_f + \pi^{\pm}(+\pi^{\pm}) + X'$ when applicable.

- Separate each event into topologies based on the presence of detected charged particles and photons.

- Sort the resulting missing mass spectra for each topology into kinematic bins based on the center-of-mass energy $W = \sqrt{2M_pE_\gamma + M_p^2}$, the center of mass cosine of the reconstructed missing mass $cos(\theta_X^{c.m.})$, vertex position, and helicity where M_p is the mass of the proton and E_γ is the energy of the incident photon.

- Determine a scaling factor based on the fraction of free protons present in the butanol target region (-5.0 cm - +4.5 cm) compared to the carbon target region (+4.5 cm - +10 cm).

- Correct for the leakage between the butanol target region and the carbon target region due to vertex location uncertainties.

- Use the scaling factor to construct a free-nucleon histogram from histograms of the butanol target region and the carbon target region.

- Correct the number of free nucleons using the leakage factor.

- Employ fitting routines to determine the yield of the helicity-subtracted mass histogram ($H_{1/2} - H_{3/2}$) and the free nucleon mass histogram.

- Divide the helicity-subtracted yield by the free-nucleon yield for each kinematic bin to obtain the E observable.
- Estimate systematic uncertainties in the resulting data points.

The subsequent subsections detail each of these steps.

4.2.1 The running period

Data for the study of the helicity asymmetry E for η photoproduction was collected during the running period designated "g9a" at JLab, with data collection beginning on November 10, 2007 and ending on February 11, 2008. The data set consisted of both linearly and circularly polarized photon beam running periods utilizing the longitudinally polarized FROST target. The polarized photon beam was generated from the polarized electron beam, provided by CEBAF, using the bremsstrahlung photon tagger in Jefferson Lab's Experimental Hall B.

Data from the running periods are separated into intervals of incident beam energies along with the associated electron beam polarization. The circularly polarized data sets utilized electron beam energies of 1.645 GeV and 2.478 GeV. The photon energy ranged from 20% to 95% of the electron beam energy, giving a photon energy range of 329 MeV to 1563 MeV for the initial circularly polarized period from November 10, 2007 to November 20, 2007, and a range of 496 MeV to 2354 MeV for the remaining two circularly polarized periods. Table 4.1 shows the dates, energies, and polarization settings for the electron beam used during the g9a running period.

To obtain the polarization observable E for η, which is the focus of this dissertation, the circularly polarized photon beam setting is required. Since both circularly polarized beam energy settings (1.645 GeV and 2.478 GeV) were in the energy range at which η photoproduction is possible, the three circular beam polarization running periods shown in Table 4.1 were included in the data analysis. As

Start Date	End Date	Electron Beam Energy	Photon Beam Polarization Setting
Nov. 10	Nov. 20	1.645 GeV	Circular
Nov. 27	Dec. 7	2.478 GeV	Circular
Dec. 7	Dec. 20	3.539 GeV	Linear
Jan. 5	Jan. 11	2.751 GeV	Linear
Jan. 17	Feb. 3	4.599 GeV	Linear
Feb. 4	Feb. 11	2.478 GeV	Circular

Table 4.1: The dates and energies for the different running periods of the g9a data set. The data was taken in JLab's Experimental Hall B using the FROST target, CLAS detector, and Bremsstrahlung tagger with a polarized electron beam provided by CEBAF.

discussed in section 3.8, there were two event triggers in CLAS for this experiment where, if both trigger conditions were met, then there existed at least one charged particle that could be reconstructed.

4.2.2 Valid runs

The determination of the validity of any given run from the g9a running period was the responsibility of the head chef (Mr. Sungkyun Park, Florida State University), with additional input from Drs. Eugene Pasyuk (JLab) and Franz Klein (Catholic University of America). Detailed documentation of each run by the Hall B shift workers allowed for pre-screening by removing any run marked as "junk", as denoted by the shift workers, from the final run list. A "junk" listing on a run indicated that something was observed to be wrong with the data collection and that the data recorded should not be used in analysis. The most common cause of a junk run was the data acquisition system crashing when running the start-up scripts for a new run; however, full documentation for why a run has been labelled as junk is available in the electronic log book, which is a documentation of everything pertinent to data collection that occurs during the running period. Along with junk runs, any runs denoted as "special" were removed from the current working run list. Special runs included commissioning, calibration, Mölar runs (used for determining electron beam

polarization), and amorphous (unpolarized). No further refinement of the run list from the g9a running period were made.

4.2.3 Particle and event identification

Particle identification in this analysis uses the time-based tracking reconstruction (TBTR) algorithm called by GPID [29] in the CLAS cooking software. GPID requires vertex information (that is, the location of the point in space where the particle originated following the reaction) from the start counter (see section 3.4) along with momentum, scattering angle, charge, and timing information from the time-of-flight subsystems (see section 3.5). GPID takes the CLAS-measured momentum of a particle and calculates a theoretical β value for that particle from this measured momentum. This theoretical β value for all possible hadron particle types is then compared to the CLAS-measured empirical β values β_m. Particle identification is then determined based on matching the closest expected theoretical β value with the empirical β_m values. A comparison between the resulting identification from GPID and a spectrum constructed from β_m and the total momentum of the particle ρ can be seen in Figures 4.1(A) and (B).

A unique requirement for pion events is also imposed on the data set. GPID does not separate pions from electrons within the data. To correct for this, a difference is taken between the calculated β and the measured β_m, as can be seen in Figure 4.2 Any events with a value of $|\beta - \beta_m|$ greater than 0.08 are filtered out of the data set as this is an indication that the event was an electron instead of a pion.

In addition to determining the particle type, GPID also attempts to match each of the particle tracks to a photon event registered in the bremsstrahlung tagger. The matching process determines the photon with the closest vertex timing to that of the particle and is considered the generating photon for that particle. The timing for the remaining photons associated with that event are then examined. If any fall within 1 ns

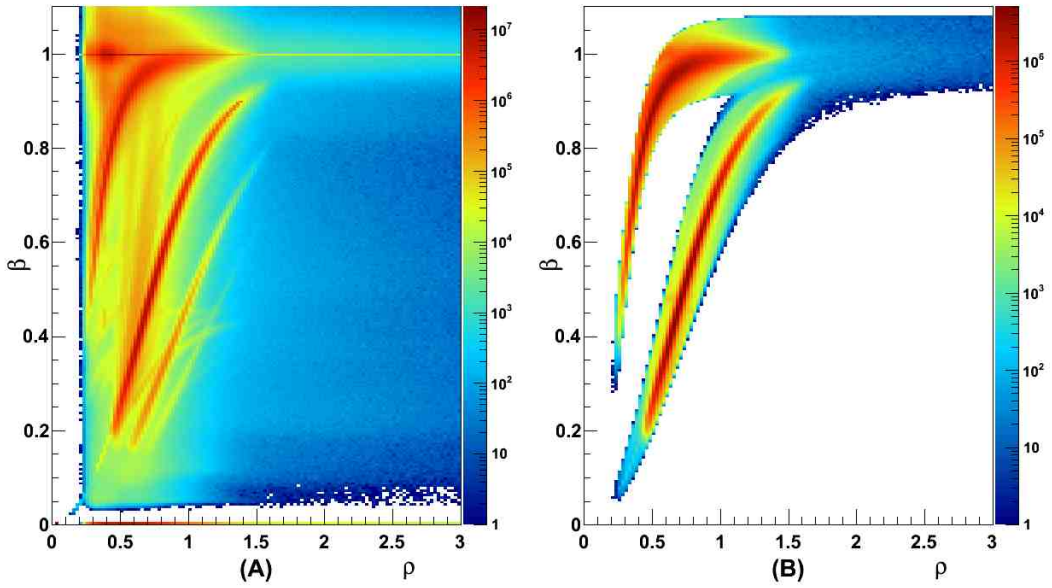

Figure 4.1: (A) A β versus ρ plot for all unsorted events recorded in GPID on a logarithmic color scale. Notice the clear stripes for pions at the top, followed by protons and deuterons. (B) A β versus ρ plot for what GPID identifies as pions and protons on a logarithmic color scale. This plot clearly shows that GPID is capable of correctly determining charged particles.

of the generating photon, the event is thrown out, since the determination of the generating photon energy is ambiguous. If only one generating photon exists within the ± 1 ns window, then the event is kept. Any identified particles that can be traced back to that vertex are then associated with that photon event. Events that did not have a generating photon associated with them are removed in the data sorting/skimming processes.

4.2.4 Energy, momentum, and trigger efficiency corrections

The energy lost by a charged particle passing through various components within the target and CLAS is non-trivial and need to be accounted for. To correct for the energy losses, the program eloss uses vertex, start counter (see section 3.4), and the tracking information for each particle (see section 3.5). In the eloss program, the CLAS

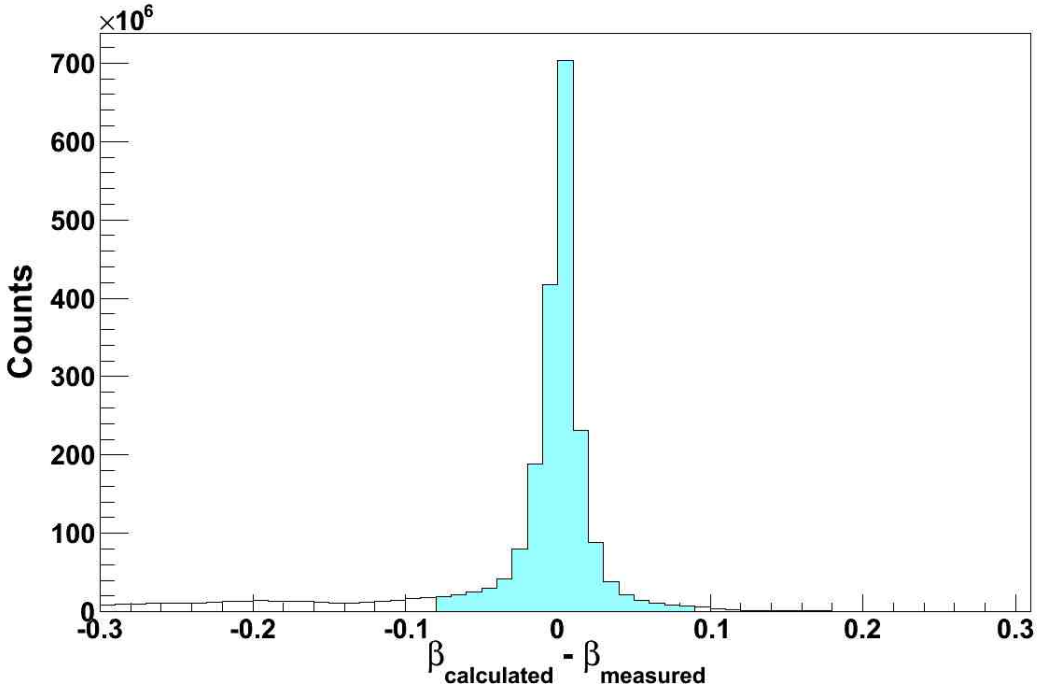

Figure 4.2: The difference between the measured and calculated β values for the entire data set. The tail to the left of zero is representative of electron events that need to be filtered out. This is done by fitting the main peak with a Gaussian and placing a cut three σ from the peak. This value is ± 0.08.

detector and subsystems are separated into components composed of like materials; these components are referred to as logical volumes. Using the vertex position and the trajectory of each charged particle, a four-momentum is established for each charged particle detected in an event. The trajectory is then propagated outwards from the vertex position through the subsystem volumes inside of CLAS, recording the length traversed within each logical volume. The length a given particle traversed, the material of the logical volumes, and the out-going four-momentum of the particle are used as input for the "eloss" algorithm. The eloss algorithm utilizes density tables for the materials of the different logical volumes, and then calculates and returns the value of the change in three-momentum for a particle propagating through that volume. The eloss process is repeated until a track propagates back to the original vertex of that

particle. The final three-momentum returned by eloss is then fed back to the analysis routines, producing a shift in mass for the missing mass calculation plots as can be seen below (Figures 4.3(A) and 4.3(B)):

After processing the energy lost due to traversing logical volumes, a momentum correction based on kinematic fitting was applied. The kinematic fitting process requires the use of the $\gamma + p_i \rightarrow p_f + \pi^+ + \pi^-$ reaction channel, since this channel is able to be fully reconstructed, allowing for a four-constraint fit to the data. Pull distributions are then created for each particle based on these fits. Slight corrections are then applied to the momentums used in the kinematic fitting process to adjust the positions of the pull distributions. This process is repeated until the pull

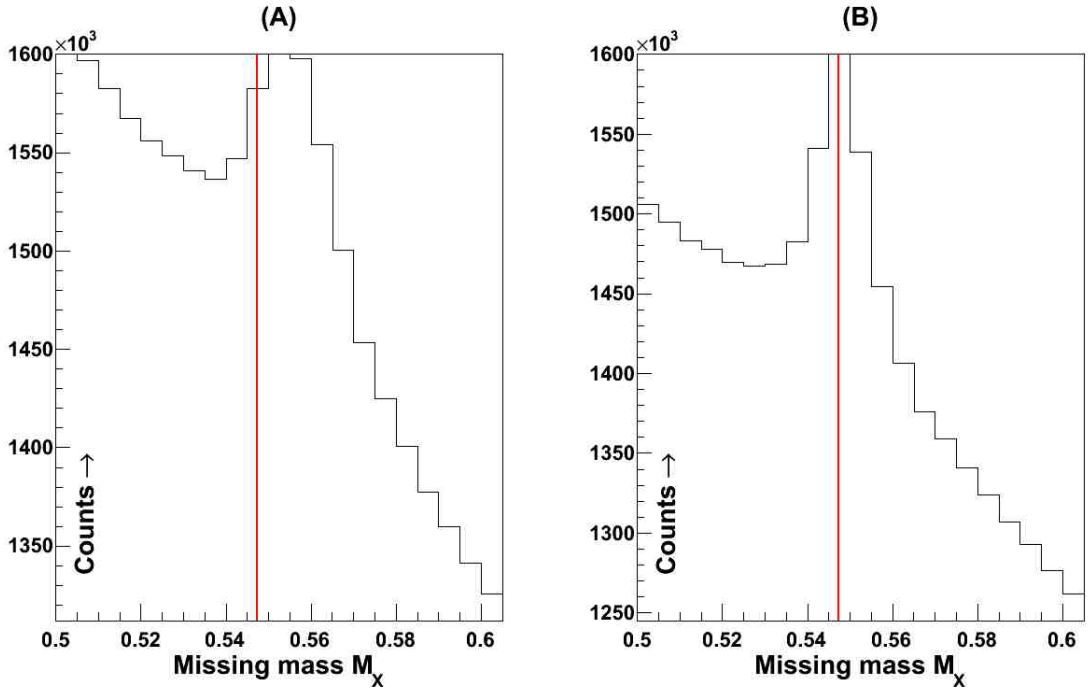

Figure 4.3: (A) The mass spectrum M_X (in GeV) for the calculated missing mass on the proton with no energy or momentum corrections. Notice the broad peak shape along with the clearly high peak mass compared to the red line for the η mass. (B) The mass spectrum for the calculated missing mass on the proton with energy and momentum corrections included. The peak shape is noticeably narrower and the peak position is correctly positioned at the η mass.

distribution for each particle is centered at zero with a symmetric shape. These final correction values are used as the momentum corrections for the data based on angle, momentum, and sector within the CLAS detector.

Trigger efficiency corrections should divide out for an asymmetry measurement. This can be shown through a simple derivation. Let subscripts one (two) denote the butanol (carbon) target region. Let superscript f (b) denote the free (bound) nucleon content in a particular target region. Then

$$\chi_1^f = \chi_1 - \chi_1^b$$

and

$$\chi_2^f = \chi_2 - \chi_2^b,$$

where χ is the number of events if no trigger inefficiencies exist. A scaling factor for the bound nucleon content subtraction $S \equiv \left(\chi_1^b + \chi_2^b\right)/\chi_2^b$ (discussed in section 4.2.8) and a correction factor for misidentified vertices $L \equiv L_{2,tbtr} + L_{2,mvrt} \big/ L_1$ (discussed in section 4.2.9) are also required. The following assumptions can be made:

$$\chi^b = (1+L)\cdot S \cdot \chi_2$$

and

$$\frac{\chi_1^b + \chi_2^b}{\chi_2^b} = \frac{\tilde{\chi_1} + \tilde{\chi_2}}{\tilde{\chi_2}} = S$$

where $\tilde{\chi}$ is exactly equivalent to χ^b for the reaction $\gamma + p_i \rightarrow p_f + \pi^+ + \pi^- + X$ when mass X^2 is negative (bound nucleon region). The initial equation can now be rewritten as:

$$\chi^f = \chi_1 + \chi_2 - (1-L)\cdot S \cdot \chi_2$$

$$\chi^f = \chi_1 + \chi_2 - (1-L)\cdot \frac{\chi_1^b + \chi_2^b}{\chi_2}$$

Since χ is an idealized measurement, the above equation is instead considered in terms of N

$$\chi = \frac{N}{\varepsilon_\lambda},$$

where ε_λ represents the efficiency of detecting the particle(s) used in reconstructing this event and N is the number of events when the trigger was not 100% efficient. Rewriting the equation for the free content χ^f in terms of efficiencies gives

$$\frac{N^f}{\varepsilon_p} = \frac{N_1}{\varepsilon_p} + \frac{N_2}{\varepsilon_p} - (1-L)\frac{\frac{\tilde{N_1^b}}{\varepsilon_p\varepsilon_{\pi^+}\varepsilon_{\pi^-}} + \frac{\tilde{N_2^b}}{\varepsilon_p\varepsilon_{\pi^+}\varepsilon_{\pi^-}}}{\frac{\tilde{N_1^b}}{\varepsilon_p\varepsilon_{\pi^+}\varepsilon_{\pi^-}}} \cdot \frac{N_2}{\varepsilon_p}.$$

As can be seen, all efficiencies cancel out from the final equation for the free nucleon content, as expected.

4.2.5 Missing mass reconstruction

The missing mass technique assumes that the initial state is known. In this analysis, the equation $\gamma + p_i \rightarrow p_f + X$ is assumed, where X is the assumed produced particle, p_f is the recoil proton, p_i is the initial proton, and γ is the incident photon four-momentum. Treating the four parts of the equation as Lorentz vectors and solving for X gives

$$X^\nu = \gamma^\nu + p_i^\nu - p_f^\nu.$$

Contracting X^ν with itself gives the squared mass of X, given by

$$M_x^2 = 2(E_\gamma \cdot M_p + E_\gamma \cdot p_z - E_\gamma \cdot E_{p_f} - E_{p_f} \cdot M_p + M_p^2).$$

Here M_p is the mass of the proton, E_p is the kinetic energy of the recoil proton, and E_γ is the incident photon energy.

The software package ROOT was used to analyze the data observed. ROOT is an analysis package produced, and maintained, by a team of scientists at CERN [30], and is used for the study and manipulation of large data sets. ROOT consists of a wide variety of classes and functions that are commonly used in physics processes. In

particular, the TLorentzVector class in ROOT allows for definitions of four-vectors as (p_x, p_y, p_z,E). Once defined, a TLorentzVector can then be manipulated as any normal four-vector by using the built-in functionality of the TLorentzVector class in ROOT. For this analysis, the TLorentzVector methods for obtaining missing mass and cosine θ values were used. To perform a missing mass calculation using the ROOT classes, three known vector quantities of the system need to be defined:

$$\gamma^{\nu} = (0,0,E_{\gamma},E_{\gamma}),$$

$$p_i^{\nu} = (0,0,0,M_p)$$

$$p_f^{\nu} = (p_x,p_y,p_z,E_{p_f})$$

These four-vectors can then be added in-line as $X = \gamma + p_i - p_f$. Once this four-momentum is defined, the M2() method is used on the X Lorentz vector. The resulting quantity is the missing mass squared for the assumed initial equation. To calculate the cosine of the polar angle for the X Lorentz vector, the CosTheta() method is used, which returns the cosine value that is used in the binning structure for the data plots.

4.2.6 Topologies

Because CLAS is primarily a charged particle detector, and the η lifetime is on the order of 5×10^{-19} s , η yields cannot be directly measured by detecting the photoproduced meson. However, particles arising from η decay may be observed in CLAS. The main branches for η decay can be seen in Table 4.2.

Since the η meson is a neutral particle, any η photoproduction event originating from a proton is expected to have a proton in the final state. In coincidence with detection of the proton, a matching tagged photon must also be present. Requiring a proton associated with a tagged generating photon in an event serves as an initial filter on the data for accidental coincidences. Unique data filters can be

Decay Modes	Branching Ratio (%)
2γ	39.24 ± 0.34
$3\pi^0$	32.2 ± 0.4
$\pi^+\pi^-\pi^0$	23.1 ± 0.5
$\pi^+\pi^-\gamma$	4.77 ± 0.13

Table 4.2: The main η decay branches from the Particle Data Group [5]

constructed by requiring different final state combinations to be observed within the CLAS detector. These filters, refered to as "topologies", are determined based on the potential η decay branches and the detection capabilities of CLAS. The final-state topologies considered for this analysis are shown in Table 4.3, with the associated decay branches for each topology (only branches $>1\%$ are shown). These six potential topologies can be seen in Figure 4.4.

To reduce the number of accidental pions and protons within each topology, events are sorted based on the tagger ID's associated with each charged particle. (Tagger ID refers to the photon recorded in the bremsstrahlung tagger associated with each charged particle detected within CLAS as discussed in section 4.2.3.) For example, an event with both a proton and a π^+ registered in CLAS, but with mismatched tagger ID's for their generating photons, would be sorted into the single-proton topology instead of a proton-plus-pion topology.

Topology	Reaction	Branches
1	$\gamma + p_i \rightarrow p_f + X$	2γ, $3\pi^0$, $\pi^+\pi^-\pi^0$, $\pi^+\pi^-\gamma$
2	$\gamma + p_i \rightarrow p_f + X$, only the proton detected	2γ, $3\pi^0$
3	$\gamma + p_i \rightarrow p_f + N\gamma + X$, $N \geq 1$	2γ, $3\pi^0$
4	$\gamma + p_i \rightarrow p_f + \pi^+ + X$	$\pi^+\pi^-\pi^0$, $\pi^+\pi^-\gamma$
5	$\gamma + p_i \rightarrow p_f + \pi^- + X$	$\pi^+\pi^-\pi^0$, $\pi^+\pi^-\gamma$
6	$\gamma + p_i \rightarrow p_f + \pi^+ + \pi^- + X$	$\pi^+\pi^-\pi^0$, $\pi^+\pi^-\gamma$

Table 4.3: The final state topologies considered for η photoproduction analysis with the CLAS detector and the FROST target.

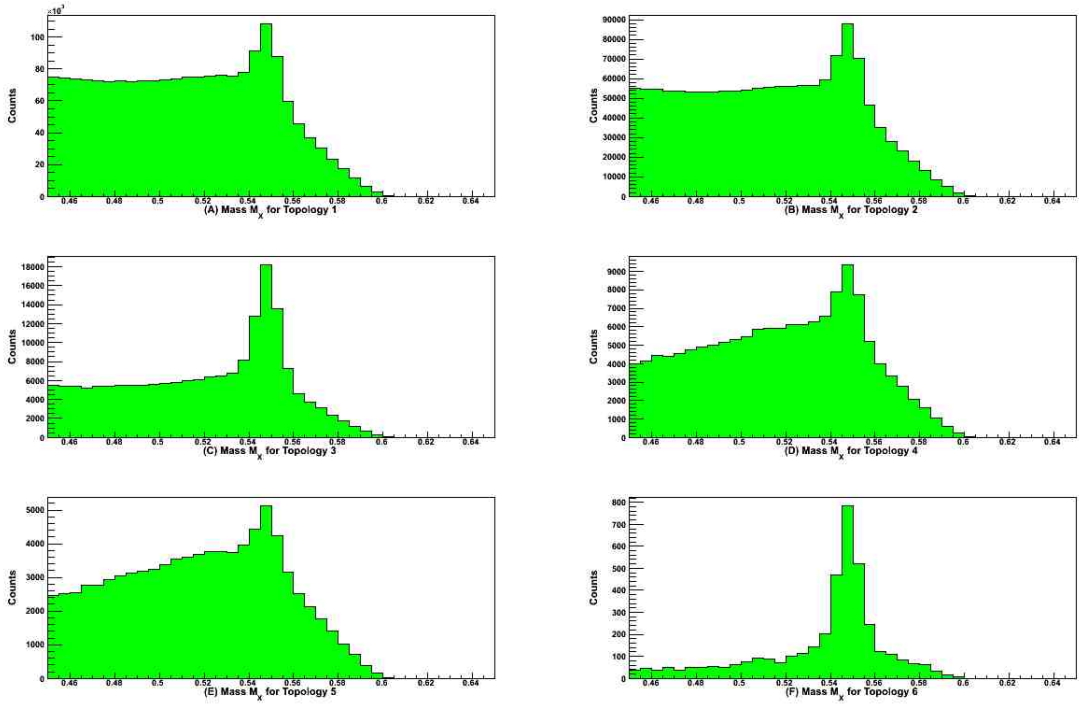

Figure 4.4: Missing mass M_X (in GeV) for the reaction $\gamma + p_i \rightarrow p_f + X$ at $W = 1.5 - 1.55$ GeV, integrated over all $cos(\theta)$ bins and helicities for each topology. (A) $p + X'$. (B) $p + X'$, no other charged particles detected. (C) $p + X' + n\gamma$, no other charged particles detected and $n \geq 1$. (D) $p + \pi^+ + X'$. (E) $p + \pi^- + X'$. (F) $p + \pi^+ + \pi^- + X'$. Topologies 4 and 5 had an additional restriction of $M_{X'} > 0.2$ GeV. Topology 6 had a restriction of $M_{X'} > 0.06$ GeV.

The ideal topology would be Topology 6 from Table 4.3, which is the closest to a full final-state reconstruction for an η decay, resulting in fewer background events. However, as can be seen in Figure 4.4(F), there is insufficient data to form a reliable measurement when the topology is further binned into the two helicity states and ten cosine bins. The same holds true for both single-pion topologies, seen in Figures 4.4(D) and 4.4(E). Out of the remaining three topologies, Topology 3 has the best signal-to-background ratio, as seen in 4.4(C). The only concern with this topology is the amount of data within each kinematic bin is low when compared to similar kinematic bins in Topologies 1 and 2. Because of this, Topology 3 can only be used up to an energy of $W = 1750$ MeV, at which point the yields for individual kinematic bins

become too small to produce reliable results. After $W = 1900$ MeV, all the topologies become unusable due to poor statistics.

One more item of note in these topologies is that there is an apparent structure in the missing mass reconstruction for the denominator plots, which traverses through the η mass region between $W = 1500$ and 1700 MeV. The source of this structure is unknown. Figures 4.5 and 4.6 show the effects of this unknown structure on the kinematic bins for Topologies 2, and its apparent absence in Topology 3, respectively.

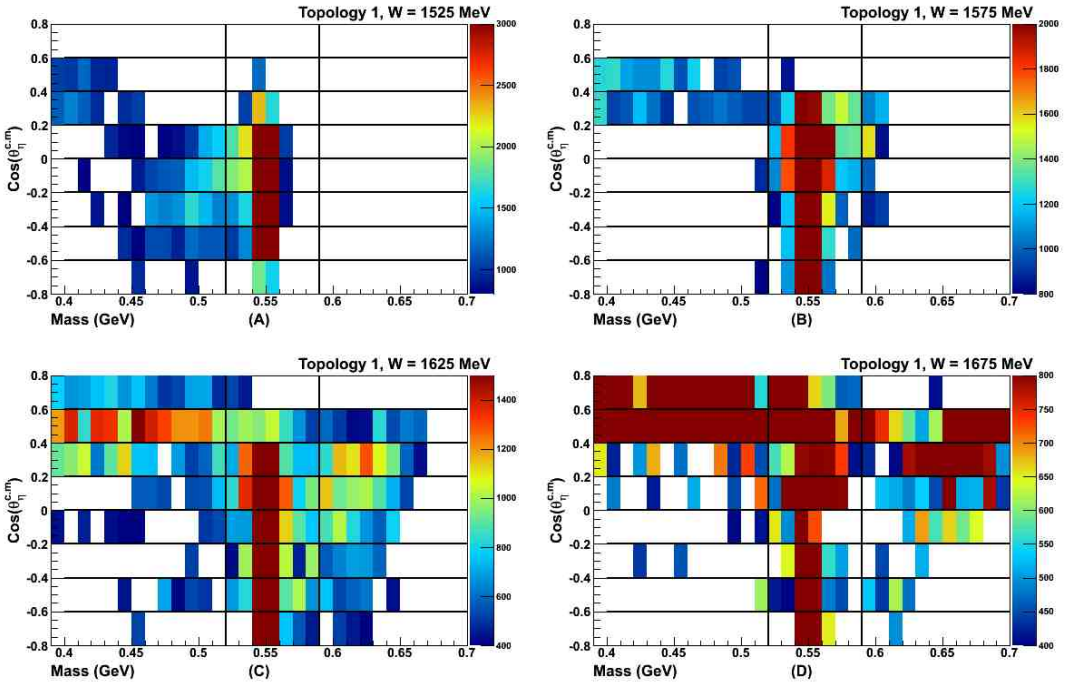

Figure 4.5: Plots of missing mass (in GeV) versus cosine (with a suppressed maximum and minimum) illustrating structure outside of the η peak region. These plots show an unknown structure within the data in the energy range of $W = 1500 - 1700$ MeV for Topology 2. Lines on each plot differentiate the kinematic cosine bins and mark the region of the η mass.

As seen in Figure 4.5(A), the structure appears to begin around -0.6 $\leq$ $\cos(\theta_\eta^{c.m.}) <$ -0.4 at M_X = 500 MeV and seems to move upward in mass and cosine as W increases. The plot in Figure 4.5(B) shows the η mass spectrum and this structure are almost indistinguishable, indicating that this energy range will not be reliable for

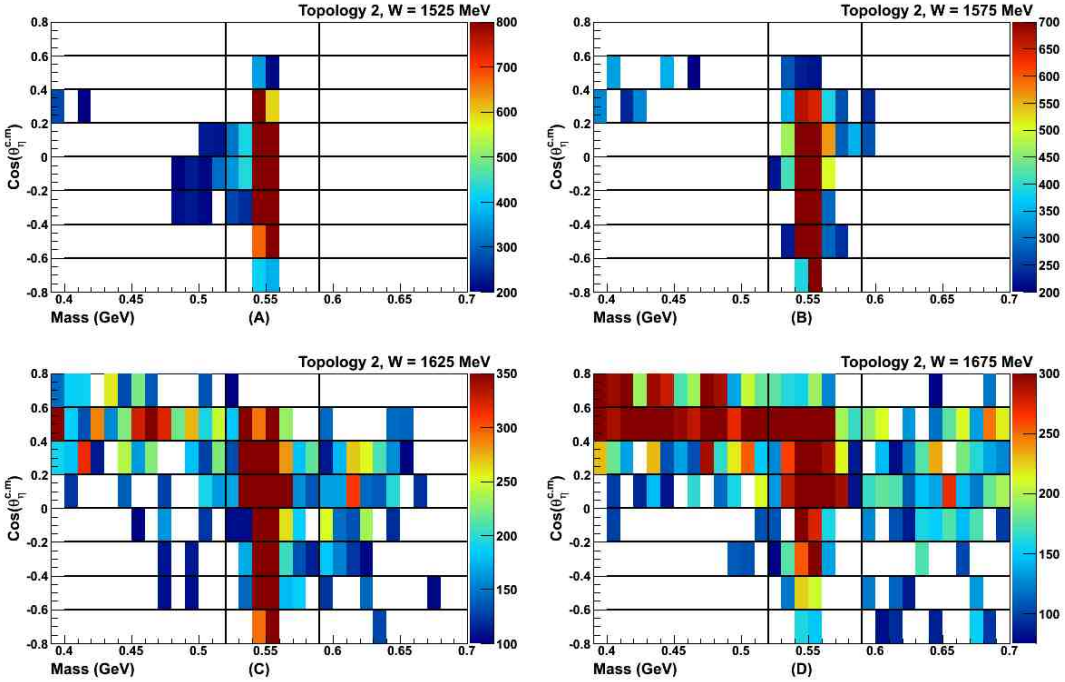

Figure 4.6: Plots of the events in Topology 3. The structure seen in Figure 4.5 appears to be negligible in this topology. Once again, lines have been drawn on each plot to differentiate the kinematic cosine bins and to denote the η mass region. The maximum and minimum have also been suppressed in the plots to show any possible structure in the data.

this topology; Topology 2, thus, cannot be used in the final analysis for this W bin. Figure 4.5(C) shows the structure beginning to move past the η mass region; however, the structure will still affect the cosine bins from -0.8 $\leq \cos(\theta_\eta^{c.m.}) <$ 0.0. In Figure 4.5(D), the structure appears to have moved fully past the η mass region.

The plots in Figure 4.6 show that this structure does not appear to have a contribution to Topology 3. The lack of contribution is most likely attributable to the suppressed background content within this topology due to the requirement of one or more photons within the event. Because of this suppression aspect, data from Topology 3 is used throughout the region where the structure is present.

4.2.7 Binning of the missing mass spectrum in helicity, W, and polar angle

The full missing-mass spectra for the topologies listed in the previous section were separated into kinematic bins of W, $cos(\theta_{\eta}^{c.m.})$, and helicity states. Each topology was sorted between 1/2 and 3/2 initial-helicity states based on the data from the trigger and the overall sign applied to that run determined empirically from initial π^+ photoproduction analysis by Dr. Steffen Strauch (University of South Carolina). By convention, the helicity 3/2 state was assigned a negative sign. The yields for π^+ photoproduction were chosen for sign determination of the helicity for individual running periods because the pion can be directly detected by CLAS. This particular channel has a very strong signal-to-background ratio and has a large cross section, making initial measurements reliable for extraction of helicity signs.

Bin sizes of 50 MeV in W and $\Delta cos(\theta_{\eta}^{c.m.}) = 0.2$ were chosen for the the data set. The energy spacing of 50 MeV was selected so that, at threshold and beyond, a yield could reliably be extracted for a given kinematic bin while keeping the spacing small enough to span any possible nucleon resonance with at least two data points (assuming the average resonance has a typical width of 100 MeV or greater). The spacing of the cosine bins was set to 0.2 to ensure that a yield could reliably be extracted in each bin, while still providing a sufficient number of kinematic bins at an energy to show structure in the polar angle.

4.2.8 The scaling factor

In order to obtain a cleaner spectrum for combined helicity plots (the denominator portion of the asymmetry equation described in Section 2.1), the contribution from the bound nucleons in the butanol target are removed from the combined spectrum before fitting routines are implemented. The removal of bound nucleon content requires a determination of the ratio of bound events present within both target regions (butanol

and carbon) to the bound events present in the carbon target region. This ratio is called the scale factor.

An unphysical mass region ($m^2 \leq -0.4$ GeV^2) is used to create a scaling factor for the bound events. The unphysical mass region is used because events found within that region must be bound events (as a negative missing-mass-squared indicates that the assumption of the reaction coming from a free nucleon is incorrect), thus giving a good ratio of bound content between the two target volumes. With the assumption that $\tilde{N_1}$ is the bound nucleon content for target volume 1 (z vertex between -5.0 cm and +4.5 cm, which should be pure butanol) in the unphysical region and $\tilde{N_2}$ is the bound nucleon content for target volume 2 (z vertex between +4.5 cm and +10.5 cm, which should only contain carbon) in the unphysical region, a scaling factor can then be defined as

$$S = \frac{\tilde{N_1} + \tilde{N_2}}{\tilde{N_2}},$$

which is the ratio of the bound content in the sum of the two target volumes to the bound nucleon content in target volume 2 (the region that should be completely empty of free nucleons in an ideal situation).

This scaling factor will vary from kinematic-bin to kinematic-bin because of differences in the probability of a recoil proton "swimming" through the targets. The scaling factors resulting from this ratio can be seen in Figure 4.7.

4.2.9 Leakage factor

Due to the positioning of the targets within FROST, a correction factor for the overlap in the target vertex spectrum between the butanol and carbon targets needs to be included when determining yields. As mentioned previously, TBTR is used for vertex reconstruction in this analysis. Another method of determining the vertex is available for events with multiple charged particles, called multi-vertex reconstruction (MVRT).

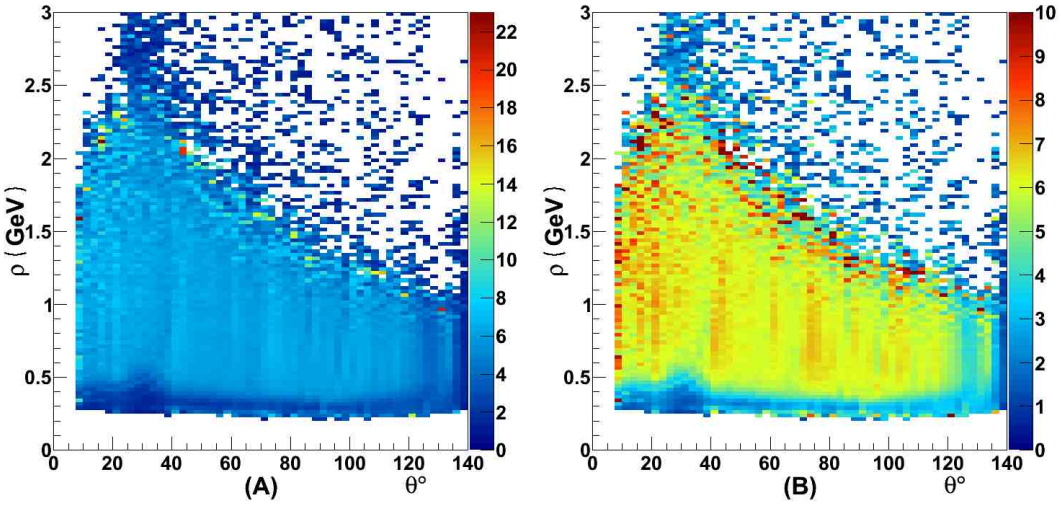

Figure 4.7: (A) The scaling factor $S = \left(\tilde{N}_1 + \tilde{N}_2\right)/\tilde{N}_2$ binned into recoil proton angle and momentum. (B) The same scaling factor with a maximum value of 10 imposed to better show the change in S over angle and momentum.

The difference between TBTR and MVRT comes from the number of particles used to reconstruct the vertex. The reconstruction from TBTR uses only information from the proton associated with the tagged generating photon. The reconstruction from MVRT uses the tracking information from all available charged particles within CLAS.

In an ideal situation, both TBTR and MVRT would give identical results, which looks to be a good approximation when looking at the vertex information for the entire run set, as seen in Figure 4.8. However, the low proton momentum and small polar angle events show large discrepancies between TBTR and MVRT, as seen in Figure 4.8. As seen in Figure 4.9, the vertex positions of MVRT and TBTR are far from identical for low proton momentum and small polar angle events.

If the two reconstruction methods produced identical results, the plots in Figures 4.8 and 4.9 would be single thin straight lines with V_z(TBTR)= V_z(MVRT). A deviation from a straight line occurs because TBTR only uses one particle track for reconstruction, while MVRT will incorporate as many tracks as are available in

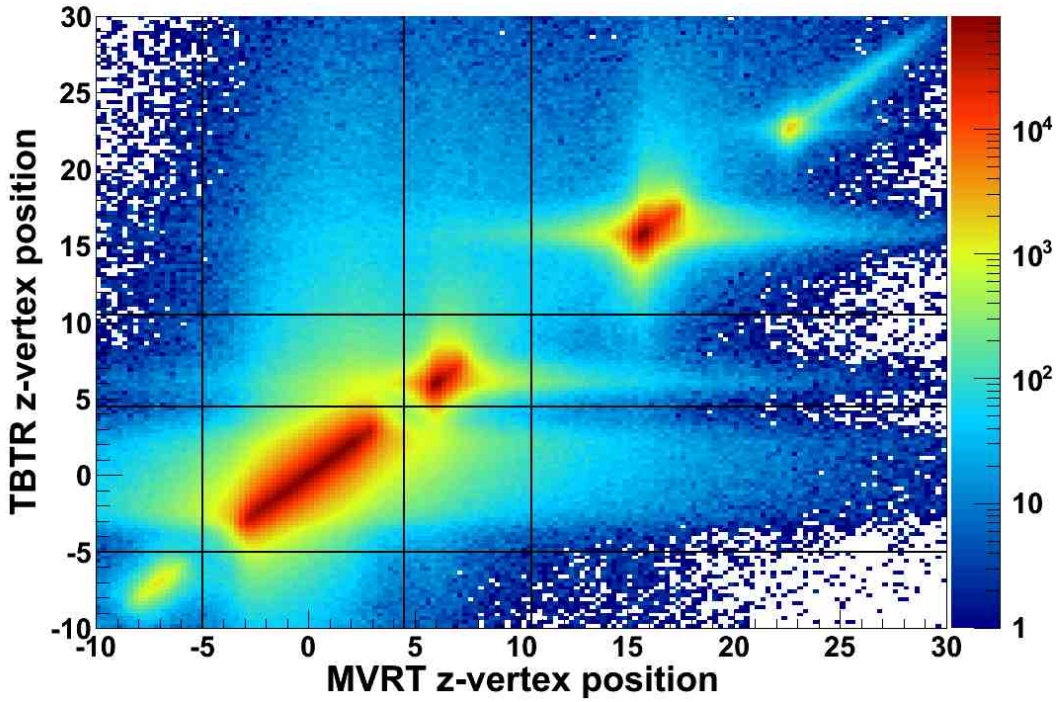

Figure 4.8: A comparison of the vertex reconstruction from MVRT and TBTR shown on a log-z color scale. Lines indicating the target cut regions are shown in black.

determining the vertex location. Thus, the MVRT vertex reconstruction is more accurate than the TBTR when there are multiple tracks within an event since, with more tracks included in a reconstruction, the vertex location will be determined with a higher degree of accuracy than a single track reconstruction can give. A simple projection on each axis shows more clearly the discrepancy between the two vertex reconstruction methods. In Figure 4.10(A), the MVRT projection is shown and a clear separation between the targets can be seen with minimal overlap. Figure 4.10(B) is the projection of TBTR; the ambiguity of the butanol and carbon target vetricies is quite apparent. Also plotted on Figure 4.10(B) are the events which MVRT determines to be a butanol event (shown in red) or a carbon event (shown in blue). The leakage seen is non-trivial and therefore must be accounted for if the TBTR reconstruction method is used in any analysis.

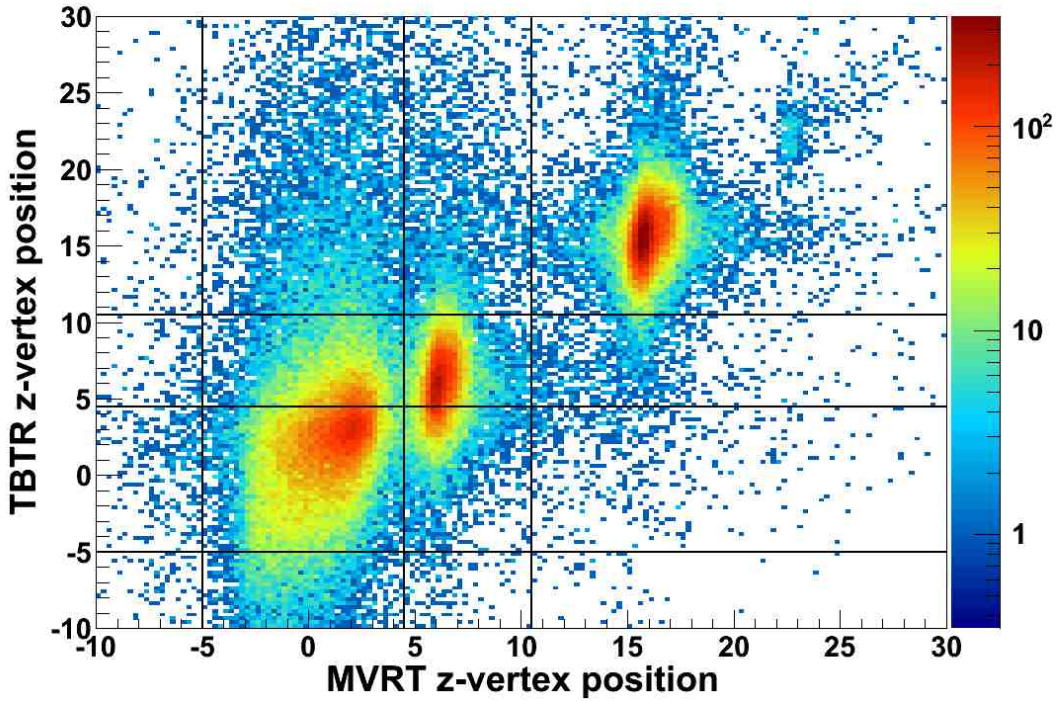

Figure 4.9: A comparison of the vertex reconstruction from MVRT and TBTR on a log-z color scale, showing the discrepancy between the two vertex reconstruction methods at low proton momentum and angle ($\rho < 400$ MeV and $\cos(\theta_p^{c.m.}) < 30^\circ$.

Unfortunately, because of the topologies single recoil proton selected for this analysis, only vertex reconstruction with TBTR can be used, and a correction "leakage" factor needs to be introduced to account for the vertex smearing. To determine this leakage factor, the assumption that the MVRT vertex for $\gamma + p \to p + \pi^+ + \pi^-$ events is correct is made. This assumption allows for use of the MVRT vertex to determine the leakage of the TBTR vertex. The number of events recorded within the butanol target as determined by both the MVRT vertex reconstruction and the TBTR reconstruction for $\gamma + p \to p + \pi^+ + \pi^-$ events are counted; this value is called L_1. Next, the number of events that MVRT reconstruction places within butanol which TBTR reconstruction places within the carbon target are counted; this value is called L_2. The ratio of these two numbers is taken as the vertex

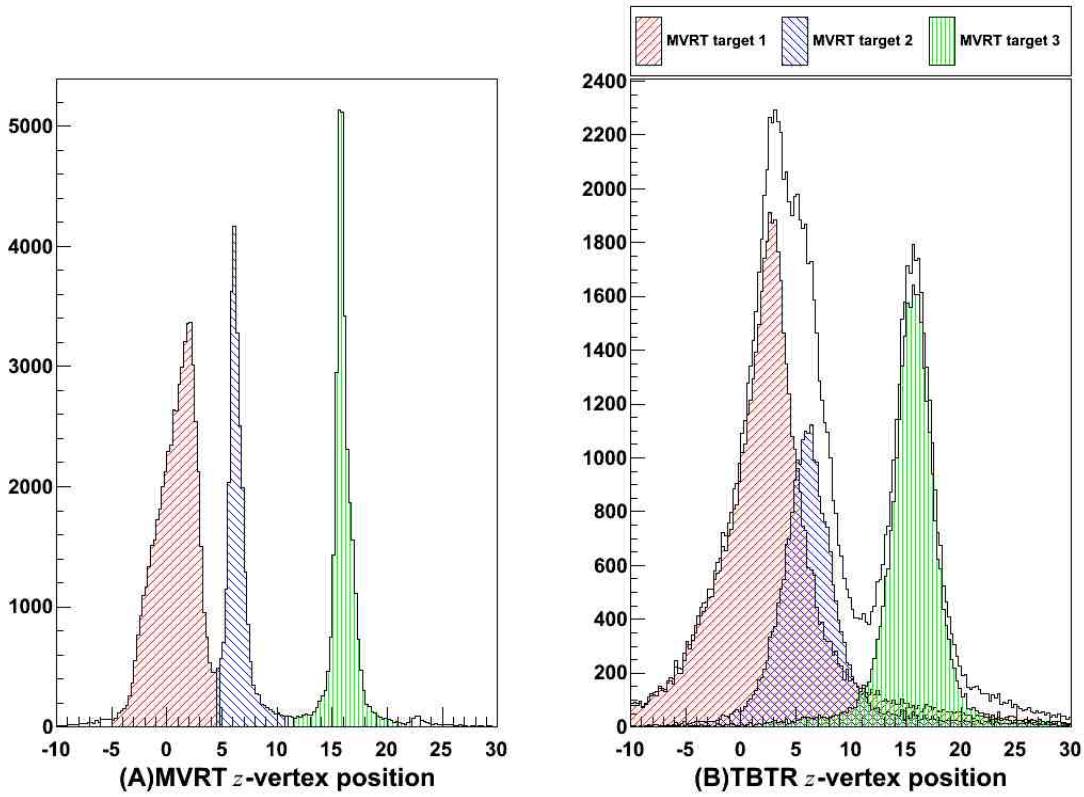

Figure 4.10: (A) A projection of Figure 4.9 for the MVRT vertex reconstruction method, each target area is shaded with a different color. (B) A projection of Figure 4.9 for the TBTR vertex reconstruction method with the vertex as determined by MVRT overlayed in their respective colors and target cuts indicated by vertical lines. As can be seen, at low laboratory proton angle and momentum, the leakage is nontrivial when using TBTR.

leakage,

$$L = \frac{L_2}{L_1}.$$

This ratio is shown in Figure 4.11 in terms of the lab momentum and angle of the recoil proton.

Up to this point, MVRT was assumed to be correct; however, this is not the case. As seen in Figure 4.10(A), a small leakage exists between the two target areas which must be accounted for. By fitting the two vertex regions in each kinematic bin,

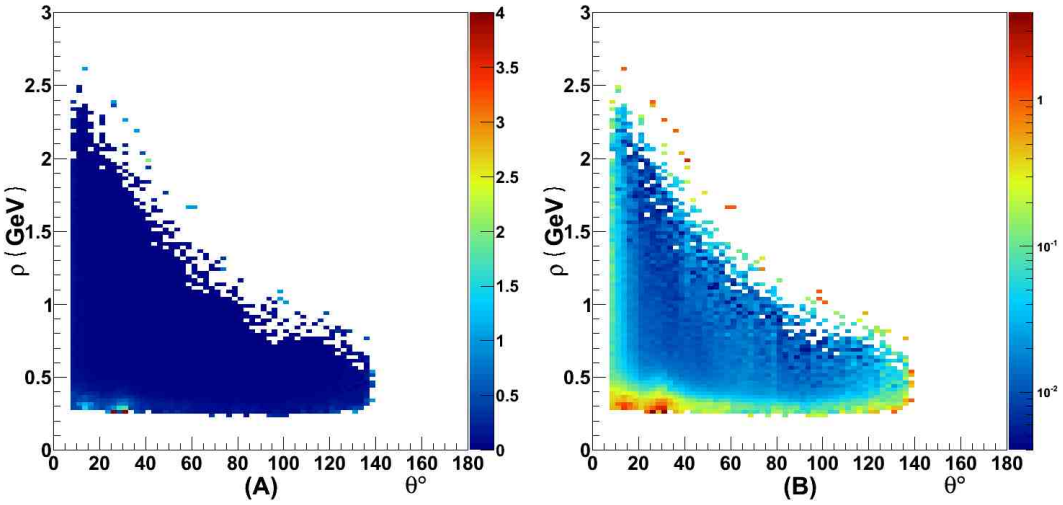

Figure 4.11: (A) The leakage ratio as defined in the text ($L = L_2/L_1$) binned into the lab momentum and angle of the recoil proton. (B) A logarithmic color scale is imposed to better show the structure of the leakage. Of note is that most of the leakage is relatively small once outside of the low lab angle and momentum area.

the amount of leakage from the butanol target into the carbon target using MVRT can be empirically determined. A sample of these fits can be seen in Figure 4.12.

The leakage within MVRT is then brought into the original leakage equation as

$$L = \frac{L_2 + L_{2,MVRT}}{L_1}.$$

which is the final equation for the leakage, as defined by the ratio of butanol events that leaked into the carbon target ($L_2 + L_{2,MVRT}$) to the total events in the butanol target (L_1). The resulting leakage factors can be seen in Figure 4.13.

4.2.10 Constructing E using the scale factor method

As a means of checking consistency, two methods were considered for the construction of the double polarization observable E. The first method involves constructing the observable from a scaling factor. Starting from a general equation O, given by

$$O = \frac{Y_1 + Y_2}{N_1 + N_2 - \alpha}.$$

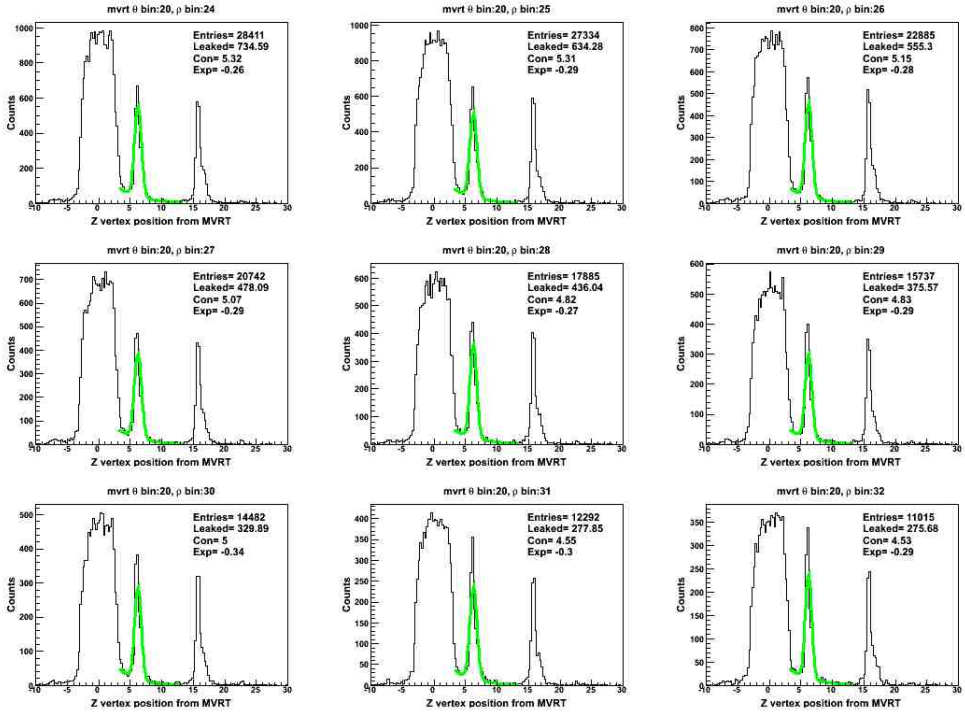

Figure 4.12: A sample of fits to the carbon target area using a Gaussian for the carbon peak and an exponential for the butanol leakage.

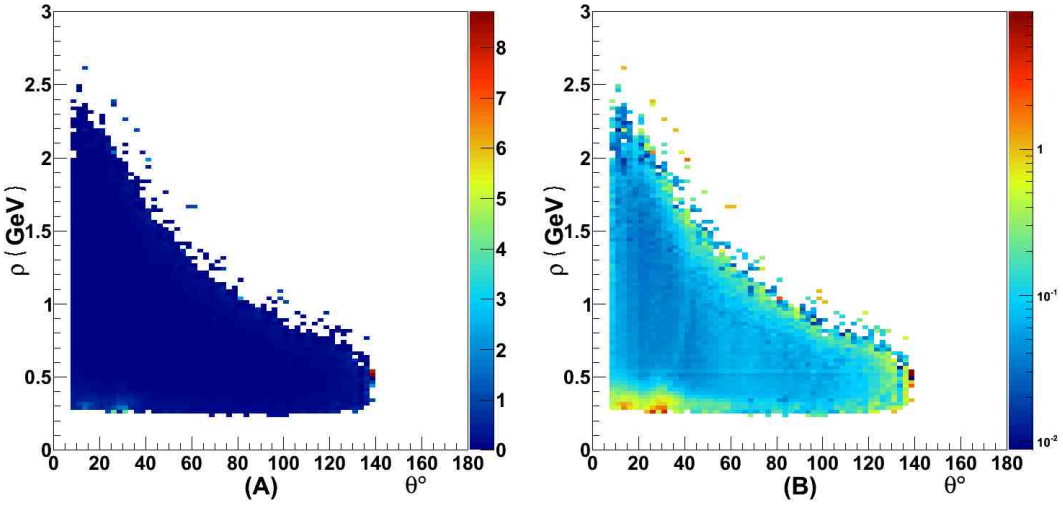

Figure 4.13: (A) The final leakage factors as used in the analysis. This version includes both TBTR and MVRT leakage. (B) A logarithmic color scale is imposed on the leakage factors to better show their structure.

Here, Y_1 and Y_2 are the helicity subtracted yields for each target region, N_1 (N_2) is the full yield coming from the butanol (carbon) target region, and α will be defined in terms of S, L, N_1, and N_2. In order to connect O with E, O will need to be a ratio of free nucleons. Specifically, O will need to have a numerator of helicity subtracted free nucleons and a denominator of helicity added free nucleons. Fortunately, the numerator is already in terms of free nucleons, since, by subtracting the two helicity states, the bound content will cancel due to equal sampling sizes and that the bound nucleons are unpolarized. This leaves the denominator to be modified. In order to determine what form α must take, first write N_1 and N_2 in terms of their free and bound content

$$N_1 = N_1^b + N_1^f,$$

where N_1^b is the bound content and N_1^f is the free content. The same type of equation can be written for the carbon target as

$$N_2 = N_2^b + N_2^f.$$

The desired result is $N_1^f \Gamma$, where $\Gamma = 1$ when there is no target leakage. In order to arrive at this, two assumptions must be made. The first assumption is

$$\frac{\tilde{N}_1 + \tilde{N}_2}{\tilde{N}_2} = \frac{N_1^b + N_2^b}{N_2^b}.$$

This assumption will hold true since the ratio of the bound content between the unphysical region (as defined in the scale factor section) and the physical region should remain constant. The second assumption is that

$$L = \frac{L_2}{L_1} = \frac{N_2^f}{N_1^f}.$$

This assumption is based on the fact that the ratio of free content that has leaked into the carbon target area to the free content in the butanol target area is equal to the

leakage between the two targets. So, with these two assumptions in place, Γ can be created to give the desired result:

$$N_1^f \cdot \Gamma = N_1 + N_2 - \alpha.$$

$$N_1 + N_2 - \alpha = N_1^f + N_1^b + N_2^f + N_2^b - \alpha.$$

Due to the bound content in N_1 and N_2, α must include negative values of N_1^b and N_2^b at the very least. To get that, $S \cdot N_2$ is introduced as α:

$$\alpha \equiv S \cdot N_2 = \frac{\tilde{N_1} + \tilde{N_2}}{\tilde{N_2}} \cdot N_2 = \frac{N_1^b + N_2^b}{N_2^b} \cdot \left(N_2^f + N_2^b\right),$$

$$\alpha = S \cdot N_2^f + N_1^b + N_2^b,$$

$$N_1 + N_2 - \alpha = N_1^f + N_2^f - S \cdot N_2^f.$$

By introducing the second assumption, the above equation can now be written in terms of only N_1^f and the scaling and leakage factors, $N_1^f \cdot L = N_2^f$, as

$$N_1^f + N_2^f - S \cdot N_2^f = N_1^f + L \cdot N_1^f - S \cdot L \cdot N_1^f,$$

$$N_1 + N_2 - \alpha = N_1^f \left(1 + L(1 - S)\right) = N_1^f \cdot \Gamma.$$

To get the total free content N^f the connection that $N_2^f = N_1^f \cdot L$ is made. Then adding N_1^f and N_2^f results in $N^f = (1 + L) N_1^f$. Returning to the original ratio equation O and multiplying by the term

$$\frac{1}{(1 + L)}$$

gives a ratio in terms of only the free nucleon content, making O equivalent to the helicity asymmetry E,

$$E = \frac{Y_1 + Y_2}{N_1 + N_2 - S \cdot N_2} \cdot \frac{1}{(1 + L)}$$

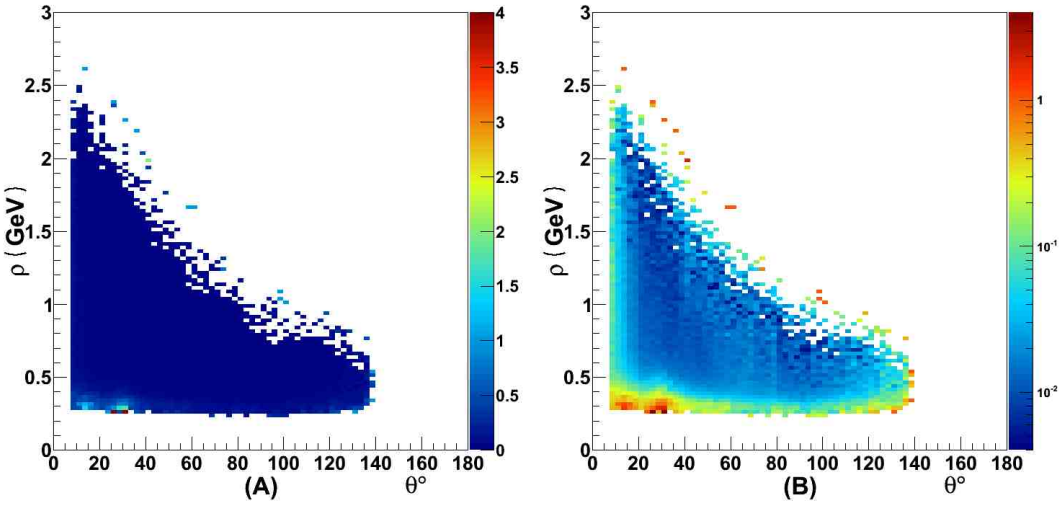

Figure 4.14: (A) The super-ratio R binned into lab recoil proton momentum and angle. (B) The same super-ratio R with a maximum value of 3 imposed in order to show the structure of the ratio. This ratio is close to one over most of phase space.

4.2.11 Constructing E using the super-ratio method

The second method takes the approach of using a "super-ratio" between free and bound content to construct the asymmetry observable. A super-ratio R is defined as a way of normalizing the detector response where

$$R = \frac{N_1}{\tilde{N}_1} \cdot \frac{\tilde{N}_2}{N_2}.$$

Note that if there is no free nucleon content in either target area, then $R = 1$. A plot of the ratio R can be seen in Figures 4.14(A) and 4.14(B).

In order to arrive at N^f to construct the asymmetry equation, it is useful to define a second super-ratio as

$$Q = 1/R = \frac{\tilde{N}_1}{N_1} \cdot \frac{N_2}{\tilde{N}_2},$$

$$Q = \frac{\tilde{N}_1}{N_1} \cdot \frac{N_2^f + N_2^b}{\tilde{N}_2} = \frac{\tilde{N}_1}{N_1} \cdot \frac{N_2^b}{\tilde{N}_2} + \frac{\tilde{N}_1}{N_1} \cdot \frac{N_2^f}{\tilde{N}_2}.$$

With the assumption that

$$\frac{N_2^b}{\tilde{N}_2} = \frac{N_2^b}{\tilde{N}_2^b} = \frac{N_1^b}{\tilde{N}_1^b} = \frac{N_1^b}{\tilde{N}_1}.$$

Q can now be rewritten as

$$Q = \frac{N_1^b}{N_1} + \frac{\tilde{N}_1}{N_1} \cdot \frac{N_2^f}{\tilde{N}_2}.$$

From here, a new scaling factor $S^{'} = \tilde{N}_1/\tilde{N}_2$ is introduced, as shown in Figures 4.15(A) and 4.15(B) . The difference between this scaling factor and the one defined previously is the inclusion of only the first target in the numerator. (The relation between the two will be resolved later.)

The ratios $f_1 = N_1^f/N_1$ and $g_1 = N_1^b/N_1$ are also introduced, where $f_1 + g_1 = 1$. Q will now take the form

$$Q = g_1 + S^{'}\frac{N_2^f}{N_1}.$$

Recalling the definition of L as defined in the previous section, N_2^f and N_1^f can be related by $N_2^f = L \cdot N_1^f$, resulting in $Q = g_1 + S^{'} \cdot L \cdot f_1$. In terms of only f_1,

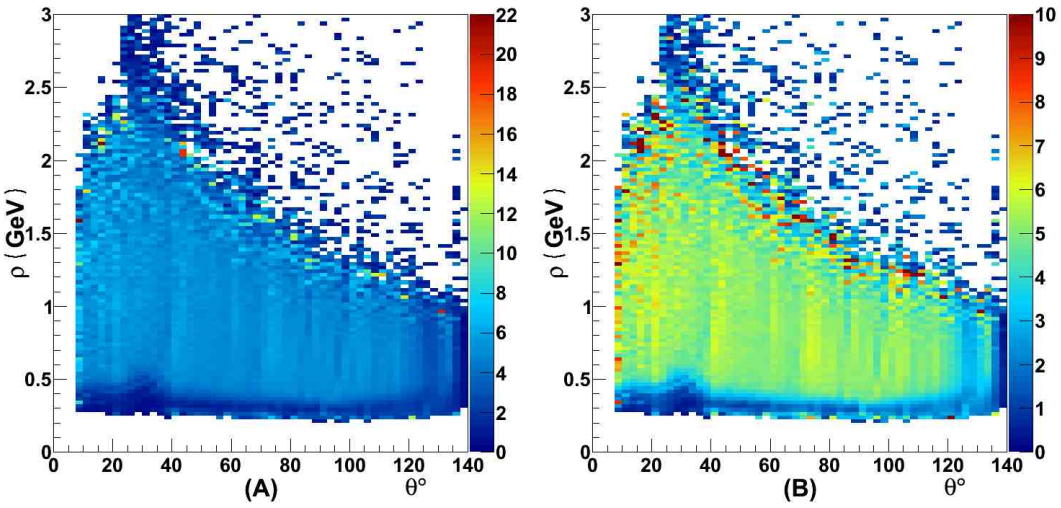

Figure 4.15: (A) The new scaling factor $S^{'} = \tilde{N}_1/\tilde{N}_2$. (B) $S^{'}$ with a maximum of 10 imposed to better show the structure over phase space.

$Q = 1 + f_1\left(S^{'} \cdot L - 1\right)$ and f_1 can be written as

$$f_1 = \left(\frac{Q-1}{S^{'} \cdot L - 1}\right).$$

In the case where there is no target leakage, $Q = 1 - f_1$, as is expected.

Next, N_1^f is related to the ratio Q by $N_1^f = N_1 \cdot f_1$, giving the equation

$$N_1^f = N_1 \cdot (Q-1)\left[\frac{1}{S \cdot L - 1}\right]$$

Note that, again, if there is no target leakage, then $N_1^f = N_1\,(1-Q)$.

Now that an equation for the free content in the butanol target area has been constructed, all that is left is to extend these ratios to find the free content that has leaked into the carbon target region. Starting from R as defined above

$$R = \frac{N_1^b}{N_1}\frac{\tilde{N}_2}{N_2} + \frac{N_1^f}{\tilde{N}_1}\frac{\tilde{N}_2}{N_2}.$$

Using the assumption

$$\frac{N_1^b}{\tilde{N}_1} = \frac{N_2^b}{\tilde{N}_2},$$

R may be expressed as

$$R = \frac{N_2^b}{N_2} + \frac{N_1^f}{\tilde{N}_1}\frac{\tilde{N}_2}{N_2}.$$

As in the case of the butanol target area, two ratios are introduced, $f_2 = N_2^f/N_2$ and $g_2 = N_2^b/N_2$, where $f_2 + g_2 = 1$. Using these ratios in conjunction with $S^{'}$ and L, R can be written as

$$R = 1 + f_2\left(\frac{1 - L \cdot S^{'}}{L \cdot S^{'}}\right).$$

Re-arranging the above equation to give a definition for f_2 gives

$$f_2 = \left[\frac{(R-1) \cdot L \cdot S^{'}}{1 - L \cdot S^{'}}\right].$$

Making the connection that $N_2^f = N_2 \cdot f_2$ gives

$$N_2^f = N_2 \cdot (R-1)\left[\frac{L \cdot S^{'}}{1 - L \cdot S^{'}}\right].$$

Note that if there is no target leakage, then $N_2^f = 0$, as is expected.

The total free nucleon content is given by $N^f = N_1^f + N_2^f$, so combining the equations for N_1^f and N_2^f gives

$$N^f = N_1 \cdot (Q-1)\left[\frac{1}{S^{'} \cdot L - 1}\right] + N_2 \cdot (R-1)\left[\frac{L \cdot S^{'}}{1 - L \cdot S^{'}}\right],$$

$$N^f = \left[\frac{1}{S^{'} \cdot L - 1}\right]\left(N_1 \cdot (Q-1) - N_2 \cdot (R-1) \cdot L \cdot S^{'}\right).$$

Setting the target leakage to zero gives a quick check to ensure this result makes sense. By imposing this condition, the equation for the free nucleon content becomes

$$N^f = N_1 (1-Q) = N_1 - N_2 \cdot S^{'}.$$

This result is exactly as expected for the case where there is no target leakage, since N_2 will be purely bound content and scaling it up by $S^{'}$ will make it equal to N_1^b.

4.2.12 Connecting the methods

These two methods should yield the same result for the number of free nucleons N^f. To connect the two methods, Q and R need to be re-written as

$$Q = \frac{N_2}{N_1} \cdot S^{'}$$

and

$$R = \frac{N_1}{N_2} \cdot \frac{1}{S^{'}}.$$

Placing these values into the equation for N^f gives

$$N^f = \left[\frac{1}{S^{'} \cdot L - 1}\right]\left(N_1 \cdot \left(\frac{N_2}{N_1} \cdot S^{'} - 1\right) - N_2 \cdot \left(\frac{N_1}{N_2} \cdot \frac{1}{S^{'}} - 1\right) \cdot L \cdot S^{'}\right),$$

$$N^f = \left[\frac{1}{S^{'} \cdot L - 1}\right]\left(N_2 \cdot S^{'} - N_1 - N_1 \cdot L + N_2 \cdot L \cdot S^{'}\right),$$

$$N^f = \left[\frac{1}{1 - S^{'} \cdot L}\right]\left(N_1 (1+L) - N_2 \cdot S^{'} (1+L)\right),$$

$$N^f = \left[\frac{1+L}{1-S^{'}\cdot L}\right]\left(N_1 - N_2\cdot S^{'}\right).$$

The two scaling factors S and $S^{'}$ are related by $S = S^{'} + 1$. Making this substitution gives

$$N^f = \left[\frac{1+L}{1-(S-1)\cdot L}\right](N_1 - N_2\cdot(S-1)),$$

$$N^f = \left[\frac{1+L}{1+(1-S)\cdot L}\right](N_1 + N_2 - N_2\cdot S),$$

$$= \left[\frac{1+L}{\Gamma}\right](N_1 + N_2 - N_2\cdot S),$$

which is exactly what the first method gave. Thus, the two methods are equivalent and should be expected to produce identical results.

4.2.13 Fitting routines

Many different approaches were used to model the background content in the numerator and denominator spectra for the kinematic bins in this analysis. While a full Monte Carlo simulation of the background was not attempted, no physics-driven model of the backgrounds were able to properly account for the observed background information in the yield histograms. For the this analysis, polynomial fitting routines have been developed to model the background content in both the denominator and numerator histograms.

The fitting routine for the denominator histograms initially uses a Gaussian function to fit the η mass region. This Gaussian is restricted such that the median value is between 540 and 560 MeV and the standard deviation σ value is limited to a maximum of 10 MeV corresponding to a resolution of 23 MeV at full-width-half-max. The median and σ values from this initial Gaussian are then used to remove the η peak content from the histogram by setting the value and error of every mass bin between three standard deviations above and below the median to zero. The ROOT fitting

routines have an option to ignore any empty bins in a histogram when performing a fit, which allows for simultaneous fitting of both sides of the mass region near the η.

Once the η mass region is excluded from the fit region, the resulting content is run through a fitting loop. This fitting loop utilizes Legendre polynomials to model the content of the histogram. Legendre polynomials are used because they form an orthogonal set over the symmetric limits of -1 to +1. In order to create the necessary symmetric limits for the Legendre polynomials, the x value fed into the fits from the fitting routine is converted to a value between -1 and +1 using the equation

$$\frac{2x-(H+L)}{H-L},$$

where H is the upper limit of the fit and L is the lower limit of the fit.

The fitting routine iterates with increasing orders of Legendre polynomials. The probability of each fit is calculated by ROOT using the built in probability function by inputting the χ^2 value and the number of degrees of freedom as determined by the fit. This probability is then compared to the current best probability (the very first fit sets the initial probability value). If the determined probability of the current fit is greater than the stored probability value, then all of the parameters of the fit and the order of Legendre used are saved and the best probability value is updated with the probability from the current fit. This process continues until either the entire range of iteration is covered (as defined by the seeded values for the limits on upper and lower bounds of the fit along with the minimum number of data points from the excluded peak region that must be included in the fit) or a probability value of 0.5 is reached. The reason for imposing the cut off at 0.5 is because this translates to a χ^2 per degree of freedom always less than 1, and any further increase is not statistically significant [31]. All denominator fits were examined on a kinematic bin-by-bin basis to ensure the fitting routine accurately portrayed the background; seeded fit parameters (upper and lower limits, minimum bins included to either side of the η mass region,

and maximum order of Legendre polynomials) were adjusted slightly, if necessary, to ensure the background contribution was modelled correctly.

Once the best fitting function is determined, the function is loaded into a new histogram and subtracted from the initial yield histogram, giving a histogram of the signal in the η mass region. The resulting signal is fit with a Gaussian function and the median and standard deviation values are used, once again, to void out the η mass region in the original yield histogram. The Legendre fitting process is then done a second time with the new histogram and the resulting best fit function is transferred into another background histogram. This second background histogram is then subtracted from the original yield histogram, giving a final signal histogram that is used for determining the η meson count. The η meson count for each kinematic bin is determined by integrating the resulting signal histogram in the region of the η mass. The limits for this integration are determined by fitting the signal with a Gaussian function and using three standard deviations from the median value as the upper and lower limits of integration. The integration limits, centroid, meson count, and error associated the count are then stored for later use.

The numerator plots were handled by excluding the η mass region in order to determine the background in the numerator yield histograms. The η mass region is input from the stored integration region for the corresponding denominator fits of the particular kinematic bin. This assumes the peak width and centroid for the numerator is the same as the denominator. By inspection, the background contribution to the numerators appears to be non-zero and flat. Because of this flatness, the numerator yield histogram with an excluded η mass region is fit with a zero order polynomial in the region from 300-700 MeV. The resulting constant value from the fit is then subtracted from the η mass region on the original numerator yield histogram and the result is integrated over that η peak region, giving a meson count for the numerator.

The main reason for using this method of determining the meson count is because the helicity asymmetry can have values near zero, and a zero value could not be fit reliably with a Gaussian curve. Figure 4.16 shows an example of a fit to a kinematic bin with strong numerator and denominator peaks. Figure 4.17 shows an example of a fit to a kinematic bin where the numerator has a value near zero. A compilation of all fits used in this analysis can be found in Appendix A.

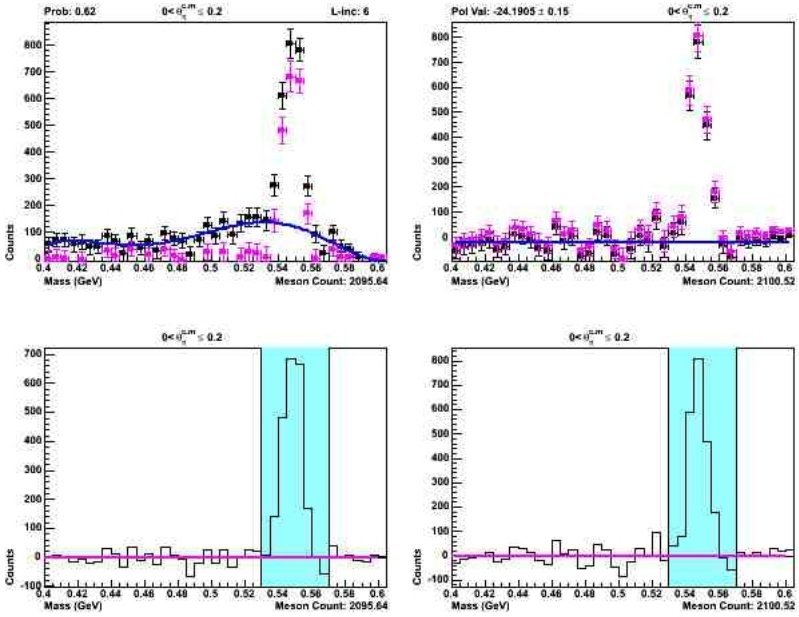

Figure 4.16: An example of a fit spectrum with a strong peak. On the left is shown the denominator spectrum, with the upper plot showing the original yield and background fit, with the lower plot showing the resulting subtracted signal spectrum. On the right are the numerator plots associated with this particular denominator. The initial yield from the data is shown in the upper boxes with black dots. The best fit to the background is shown with a solid blue line. The resulting yield from the subtraction of the background is shown with pink dots. A zero-line is drawn as a reference in the lower boxes showing a bar graph of the subtracted spectrum. The range of integration is indicated by a light blue shading in the lower boxes as well.

4.2.14 Uncertainties and systematics

The uncertainty in the observable E for each kinematic bin is given by

$$\left(\frac{\sigma_E}{E}\right)^2 = \left(\frac{\sigma_N}{N}\right)^2 + \left(\frac{\sigma_D}{D}\right)^2 - 2\frac{cov(N,D)}{N \cdot D},$$

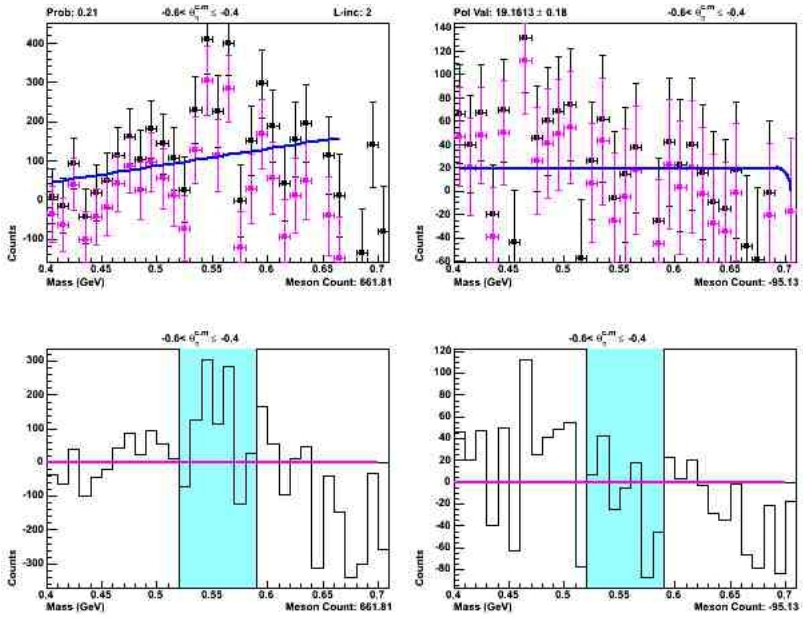

Figure 4.17: An example of a spectrum with a numerator that has a value near zero. As in Figure 4.16, the denominator is shown on the left and the numerator is shown on the right. The coloration and markings are identical to Figure 4.16 as well.

where N is the meson count from the numerator plot, D is the meson count from the denominator plot, σ_N is the uncertainty of the points in the numerator plot added in quadrature, σ_D is the uncertainty of the points in the denominator plot, and $cov(N,D)$ is the covariance between the numerator and denominator. The propagation of error within the histograms, including background subtraction, is handled by the methods built into the ROOT histogram structure using Poisson statistics (and multiplying the error by the weight of the data point).

For the covariance between the numerator and denominator, the scale factors and leak factors are treated as constants for individual kinematic bins. Expanding N and D within the covariance gives

$$cov(N,D) = cov(N_{t1}+N_{t2}, \alpha \cdot (D_{t1}+D_{t2}-S \cdot D_{t2})),$$

where α is the constant associated with the polarization and leakage factors and S is the constant associated with the scaling factors for carbon. Since the butanol and

carbon target region are independent, their covariance will be zero. The covariance equation then becomes

$$\alpha\left(cov(N_{t1},D_{t1})+cov(N_{t2},D_{t2})\cdot(1-S)\right).$$

The covariance between the numerator and denominator is

$$cov(Y_{1/2}-Y_{3/2},Y_{1/2}+Y_{3/2})=\sigma^2_{Y_{1/2}}-\sigma^2_{Y_{3/2}}.$$

Utilizing Poisson statistics, $\sigma^2_{Y_{1/2}}$ and $\sigma^2_{Y_{3/2}}$ can be correlated to the $Y_{1/2}$ and $Y_{3/2}$ yields directly, since the variance in Poisson statistics gives the mean value of the measured variable. The mean value for individual helicity bins can be directly measured as the yield for that particular helicity, giving $\sigma^2_{Y_{1/2}}\approx Y_{1/2}$. This approximation can be applied to individual target regions, resulting in the equation

$$\sigma^2_{Y_{1/2}}-\sigma^2_{Y_{3/2}}=Y_{1/2}-Y_{3/2}=N.$$

This now gives an expression for the covariance between the numerator and denominator as

$$cov(N,D)=\alpha\cdot(N_{t1}+N_{t2}\cdot(1-S)).$$

This histogram is generated simultaneously with the denominator and numerator histograms, and the value of the covariance term is obtained by integrating this histogram over the same region as the integral used for determining the meson count (as mentioned in section 4.2.16). This error propagation is handled on a kinematic-bin by kinematic-bin basis for each topology.

Since E is an asymmetry measurement, many systematic uncertainties divide out. Among these are the number of scattering centers, acceptance, and trigger efficiencies (as shown earlier). What does need to be accounted for are the systematic uncertainties resulting from beam polarization, photon flux, and scaling factors.

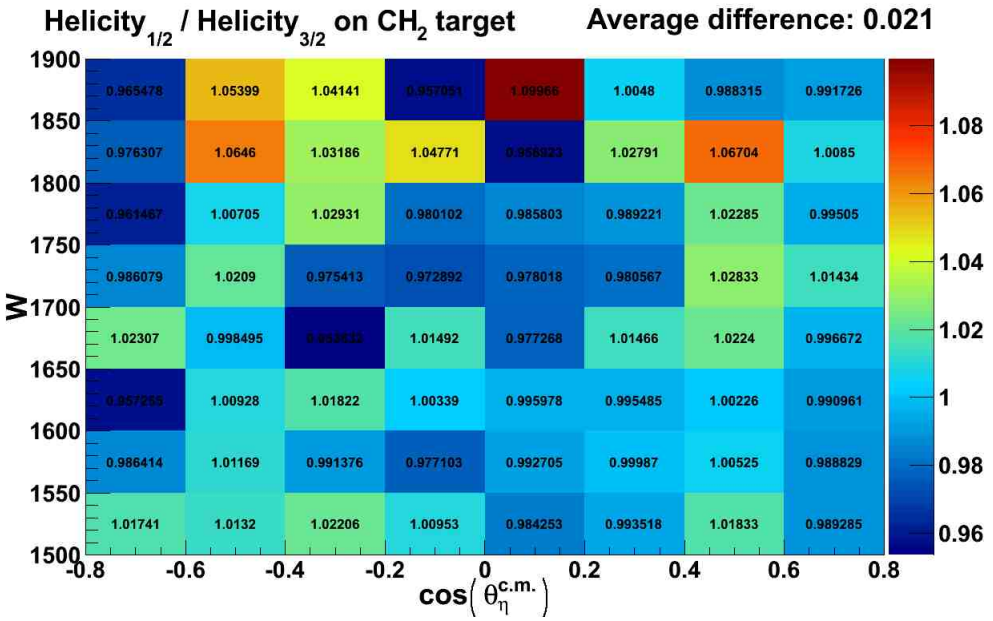

Figure 4.18: The ratio of the helicity 1/2 to the helicity 3/2 events on the CH_2 target with a mass restriction or $M_X < 0.2$ GeV, which limits the events to π^0 photoproduction.

To measure the photon flux, the CH_2 target was used with a cut around the π^0 mass. The number of helicity 1/2 and helicity 3/2 states are counted over the entire data set and separated by kinematic bin. Figure 4.18 shows the resulting flux for each kinematic bin; in an ideal situation these values should all be 1. The average of the photon flux for all kinematic bins gives a systematic uncertainty of 2.1% in the range of data used in this analysis.

Systematic uncertainties for target polarization for the g9a data set have been determined in Reference [32]. The value for the systematic portion of the uncertainty is $\pm 1.3\%$, and the statistical uncertainty is $\pm 0.2\%$, giving a total uncertainty for target polarization of 1.3% when added in quadrature.

Since the polarization depends on the photon energy, the systematic uncertainty for the electron beam energy can be taken as a systematic uncertainty of the resulting photon beam. The beam specifications for the g9a running period give the relative precision of the electron beam energy as being $\sigma_{E_{e^-}}/E_{e^-} = 0.0005$. Assuming

that a photon at the lowest possible energy from a generating electron ($0.2 \cdot E_e$) should give the greatest uncertainty contribution, and that the variance of photon energy is given by the possible range of tagged photon energies ($E_e(0.95-0.2)$) divided by the number of E counter channels (767), the uncertainty for photon beam polarization can be derived from the equation which yields the polarization

$$P = \frac{4\kappa - \kappa^2}{4 - 4\kappa + 3\kappa^2},$$

as derived in section 2.4, yielding a value of 0.6% as the maximum uncertainty in P. The average value for electron beam polarization, disregarding polarization directionality, was 83.7% with an uncertainty of $\pm 0.4\%$ (determined by averaging the errors added in quadrature) as established by Mölar measurements [33]. This results in a systematic uncertainty for the electron beam polarization of 0.4%. The total polarization for the photon is given by $P \cdot P_e$, and the calculation for the statistical uncertainty of the photon beam polarization gives a statistical uncertainty for the photon beam polarization of 0.7%.

A study of the systematic uncertainties in the scaling factors has been performed in Reference [34]. The systematic uncertainties for the two topologies used in this analysis are less than 2%.

4.2.15 Finalizing the data points

Not all kinematic bins have a well-determined E. This can quickly be seen by looking at the higher energy denominator fits, as many of them have very little signal recoverable from the background events.

One method used to determine if a bin is acceptable is by looking at the variance of the scaling factors within each kinematic bin. This is done in three steps: Calculating the average of the scaling factors within a kinematic bin, determining the standard deviation of each scaling factor from this average, and creating a ratio of this

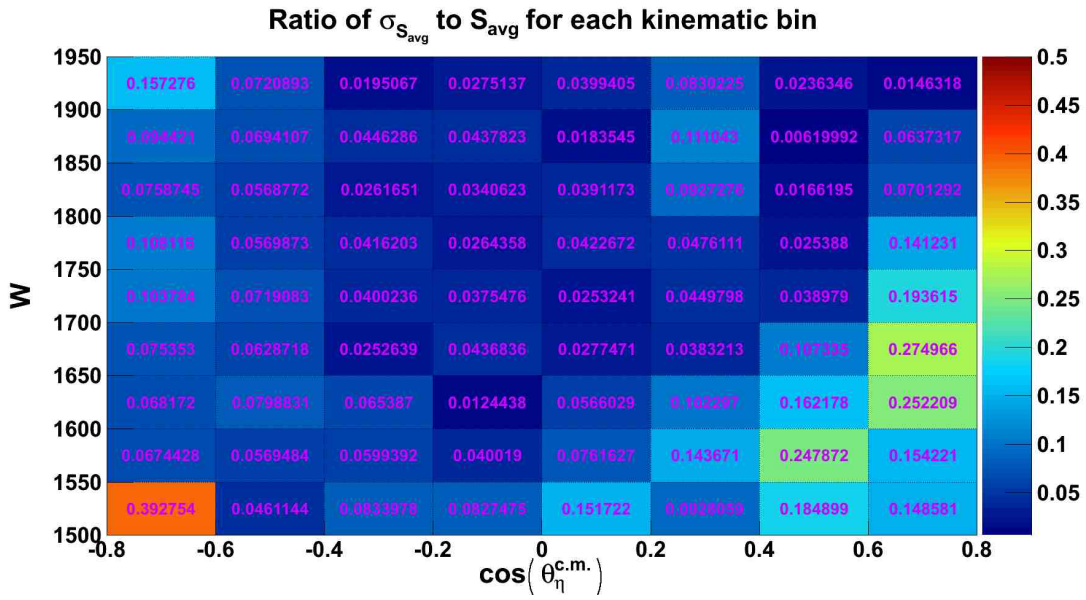

Figure 4.19: The ratio of the average standard deviation of the scaling factors to the average value of the scaling factors.

standard deviation to the average scaling factor value. These values are shown in Figure 4.19. Plotting these ratios allows them to be fit with a Gaussian; the resulting fit, along with the one, two, and three standard deviation values can be seen in Figure 4.20. Upon examining the plot, a reasonable cut can be imposed at the three standard

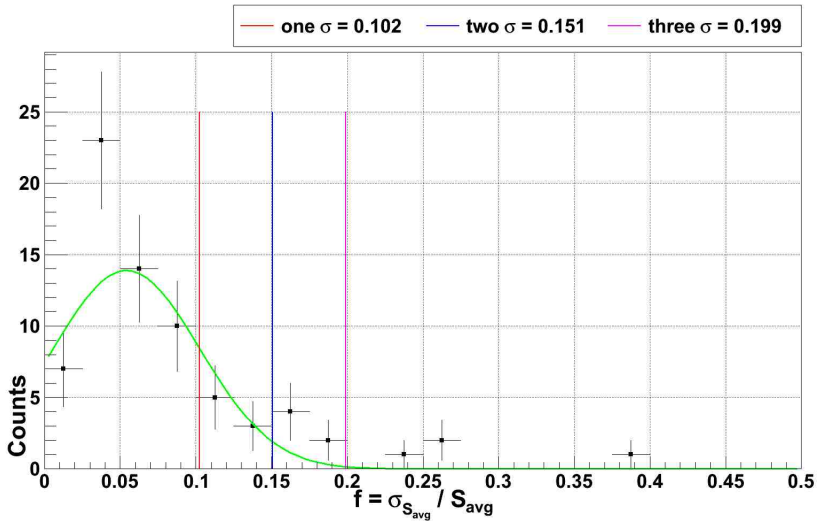

Figure 4.20: A plot of the variance in the scaling factors. A Gaussian has been fit to the spectrum with one, two, and three σ values indicated.

deviation value of 0.2. Making this restriction ensures that the regions analyzed will have relatively small and smooth variations in scaling factors, and the values used should be reliable.

After the initial scaling factor selection criteria, the denominator plots are examined on a kinematic bin-by-bin basis to remove data with little to no signal in the denominator after performing the background subtraction, since no reliable results could be obtained from these bins.

Once the bin rejection process has been completed, the final results are plotted with their associated error bars and are presented in the following chapter.

Chapter 5

RESULTS

By following the procedure outlined in the previous chapter, results for the helicity asymmetry E were obtained. In this chapter, these results are compared to the SAID, η-MAID, and Bonn-Gatchina predictions discussed in Section 2.2. The results are presented for Topologies 2 and 3 in ascending center-of-mass energy from $W = 1500$ to 1900 MeV. Beyond $W = 1900$ MeV, both topologies become unusable due to a lack of statistics. For both topologies, the very first and very last kinematic bins in $\cos(\theta_\eta^{c.m.})$ (-1.0 to -0.8 and 0.8 to 1.0) are excluded because at these extreme angles there are holes within the CLAS detector to allow the photon beam to enter and exit, resulting in rapidly changing acceptance that could not be modelled.

5.1 Helicity observable E for $W = 1500 - 1700$ MeV

Shown in Figure 5.1 are the resulting E observables for the first four energy bins above threshold for η photoproduction from the proton. The black data points were obtained by using Topology 3, while the purple data points were obtained from Topology 2. The green line represents the partial wave analysis model from Bonn-Gatchina, the blue line represents the isobar model of η-MAID, and the red line is the partial wave analysis model from SAID's 2004 publication.

Figure 5.1(A) shows the E observable at threshold ($W = 1500 - 1550$ MeV). Here, the kinematic bin -0.8 $\leq \cos(\theta_\eta^{c.m.}) <$ -0.6 has been rejected in both topologies due to the large variation in the scaling factor, being greater than 0.2, within the bin. The kinematic bins for -0.2 $\leq \cos(\theta_\eta^{c.m.}) <$ 0.8 are rejected in Topology 2 due to the structure discussed in section 4.6. This structure does not appear to affect Topology 3.

Since the $S_{11}(1535)$ resonance dominates η photoproduction at threshold, the expected value for the results of this bin should have values near one. A value of

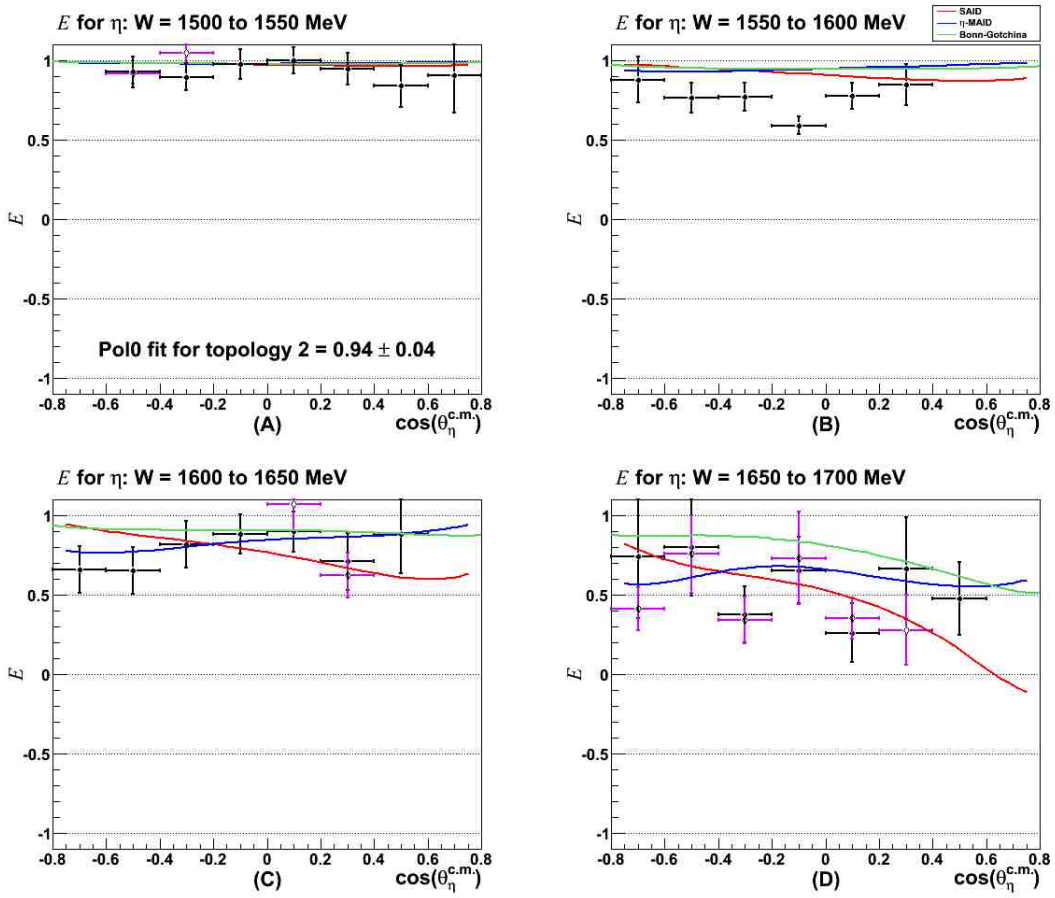

Figure 5.1: The E observable for $W = 1500-1550$ MeV (A), $W = 1550-1600$ MeV (B), $W = 1600-1650$ MeV (C), and $W = 1650-1700$ MeV (D). The data for Topology 3 is shown with black and the data for Topology 2 is shown with purple when available.

exactly one is not expected since η photoproduction does still couple to other resonances near threshold (as seen in Figure 1.2), albeit very weakly. There is also the possibility of non-resonant contributions under the $S_{11}(1535)$ resonance that need not have a helicity asymmetry of one. A fit to the theoretical predictions gives a value of 0.98, and a fit of a constant to the data gives a value of 0.94 ± 0.04, within one standard deviation of the theoretical prediction. Thus, existing theories agree with the data observed here at threshold.

Figure 5.1(B) shows the E observable for $W = 1550 - 1600$ MeV. The entirety of Topology 2 is not used in this energy range due to the structure mentioned in section 4.6.

For Topology 3, the kinematic bin $0.4 \leq \cos(\theta_{\eta}^{c.m.}) < 0.6$ has been rejected due to the large variation of the scaling factor within the kinematic bin. The kinematic bin for $0.6 \leq \cos(\theta_{\eta}^{c.m.}) < 0.8$ has also been rejected in Topology 3 due to poor statistics in the denominator, resulting in a spectrum that could not be reliably fit.

Figure 5.1(C) shows the E observable for $W = 1600 - 1650$ MeV. In this energy range the structure begins to disentangle itself from the η mass region, allowing for the use of the kinematic bins $0.0 \leq \cos(\theta_{\eta}^{c.m.}) < 0.8$ for Topology 2. In this energy range, the kinematic bin with $0.6 \leq \cos(\theta_{\eta}^{c.m.}) < 0.8$ has been rejected due to the large variation of the scaling factor within the kinematic bin for both topologies. In this energy range, η-MAID appears to fit the data the best; however, as can be seen at the higher angles, there may be a second dip in the observable, as predicted by SAID.

Figure 5.1(D) shows the E observable for $W = 1650 - 1700$ MeV. The structure that has appeared in the data from Topology 2 up to this point now appears to have moved far enough past the η mass region to allow for full usage of both topologies. The kinematic bin for $0.6 \leq \cos(\theta_{\eta}^{c.m.}) < 0.8$ is rejected for both topologies due to the large variation of the scaling factor within the bin. For Topology 2, the kinematic bin for $0.4 \leq \cos(\theta_{\eta}^{c.m.}) < 0.6$ has also been rejected due to poor statistics in the denominator plot, resulting in a spectrum that cannot be reliably fit. The resulting data points between the two topologies are consistent with one another and appear to approximately follow the prediction by SAID, but no theory seems to very accurately represent the data in this energy range.

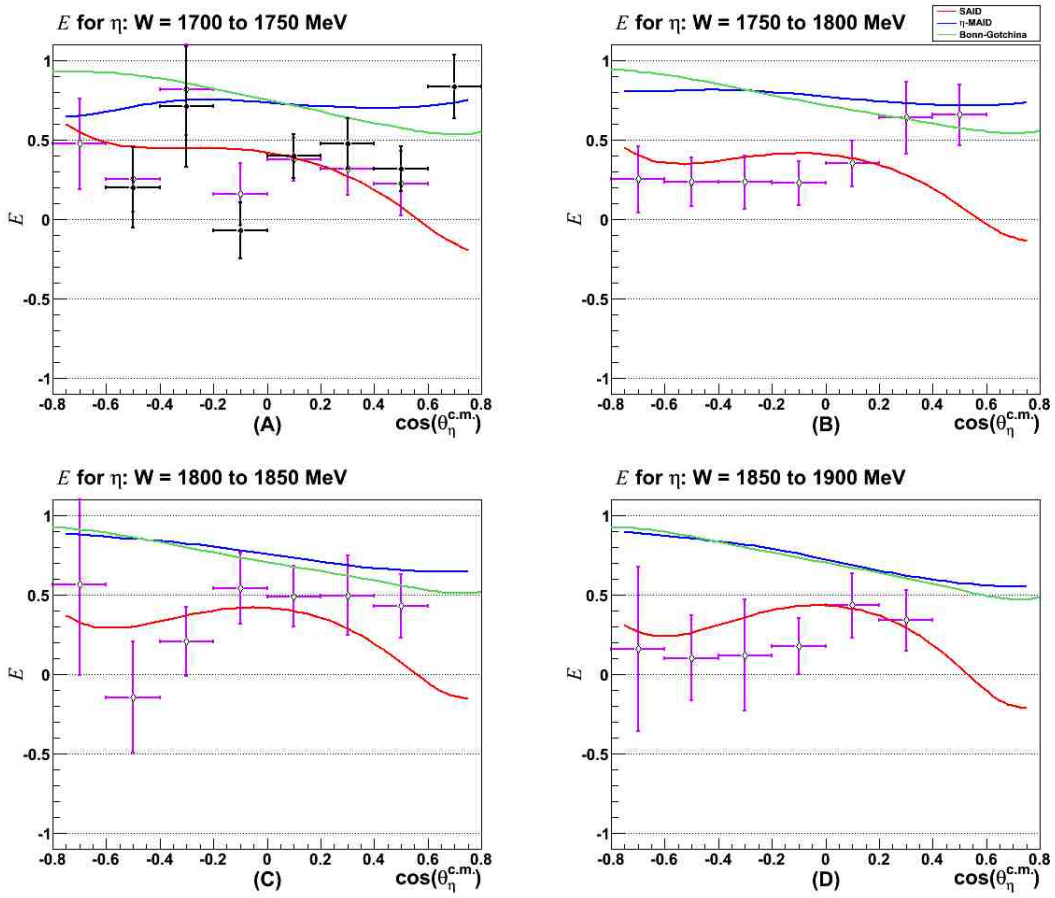

Figure 5.2: The E observable for $W = 1700 - 1750$ MeV (A), $W = 1750 - 1800$ MeV (B), $W = 1800 - 1850$ MeV (C), and $W = 1850 - 1900$ MeV (D). As before, the data for Topology 2 is shown in purple and the data for Topology 3 is shown in black.

5.2 Helicity observable E for $W = 1700 - 1900$ MeV

Shown in Figure 5.2 are the resulting E observables for the energy bins of $W = 1700$ MeV to 1900 MeV for η photoproduction from the proton. The data for Topology 2 is shown in purple and the data for Topology 3 is shown in black. The green line represents the partial wave analysis model from Bonn-Gatchina, the blue line represents the isobar model of η-MAID, and the red line is the partial wave analysis model from SAID's 2004 publication.

Figure 5.2(A) shows the E observable for $W = 1700 - 1750$ MeV. For Topology 2, the kinematic bin for $0.6 \leq \cos(\theta_\eta^{c.m.}) < 0.8$ has been rejected due to poor statistics in the denominator, giving an unreliable fit to the data. Likewise, the kinematic bin for -0.8 $\leq \cos(\theta_\eta^{c.m.}) <$ -0.6 has been rejected from Topology 3 for poor statistics in the denominator. At this W, Topology 3 is becoming much less useful as the statistics are nearing the point of being unusable. However, the resulting distributions for each topology are still consistent with one another and seem to show a bit more structure than any theory. SAID is by far the closest, but still misses many of the data points.

Figure 5.2(B) shows the E observable for $W = 1750 - 1800$ MeV. From this point onwards, the statistics in Topology 3 become unusable; only the results from Topology 2 will be shown. The kinematic bin for $0.6 \leq \cos(\theta_\eta^{c.m.}) < 0.8$ has been rejected in this energy range due to poor statistics, resulting in unreliable fits to the denominator spectrum. Here, SAID seems to do fairly well for the backward angles, but does not account for the upward trend of the data in the forward angles. Bonn-Gatchina and η-MAID clearly do not fit the data well from this energy onward.

Figure 5.2(C) shows the E observable for $W = 1800 - 1850$ MeV. Here, once again, the kinematic bin for $0.6 \leq \cos(\theta_\eta^{c.m.}) < 0.8$ has been rejected due to poor statistics in the denominator spectrum. The main point of emphasis in this energy range is for the kinematic bin within -0.6 $\leq \cos(\theta_\eta^{c.m.}) <$ -0.4, where a numerator value of near or below zero is obtained. This structure is not predicted by any of the theories, although SAID has a small dip in the theory at this point. Other than that one point, SAID seems to fit the data fairly well.

Figure 5.2(D) shows the E observable for $W = 1850 - 1900$ MeV, this is the last energy range available in this analysis, as, past this point, the statistics in all topologies become very poor, making a reasonable fit to the data nearly impossible. In

this energy range, the kinematic bin for $0.6 \leq \cos(\theta_\eta^{c.m.}) < 0.8$ has been rejected due to poor statistics, resulting in unreliable fitting results to the denominator spectrum. Many of the bins for this energy range have E values that are approaching zero, where only SAID predicts small, positive values.

5.3 Excitation plots

The data for the helicity asymmetry E may also be displayed for a given $\cos(\theta_\eta^{c.m.})$ bin as a function of W. Such plots, shown in Figure 5.3, are called excitation plots. Also shown in Figure 5.3 are the the fits from the 2004 SAID prediction (red line), the newest numbers from SAID (black line), η-MAID (blue line), and Bonn-Gatchina (green line) for each $\cos(\theta_\eta^{c.m.})$ bin. Data from Topology 2 is indicated in purple and data from Topology 3 is indicated in black. While all models predict $E \sim 1$, only the 2004 SAID values come close to the data once past the region where the $S_{11}(1535)$ dominates η photoproduction.

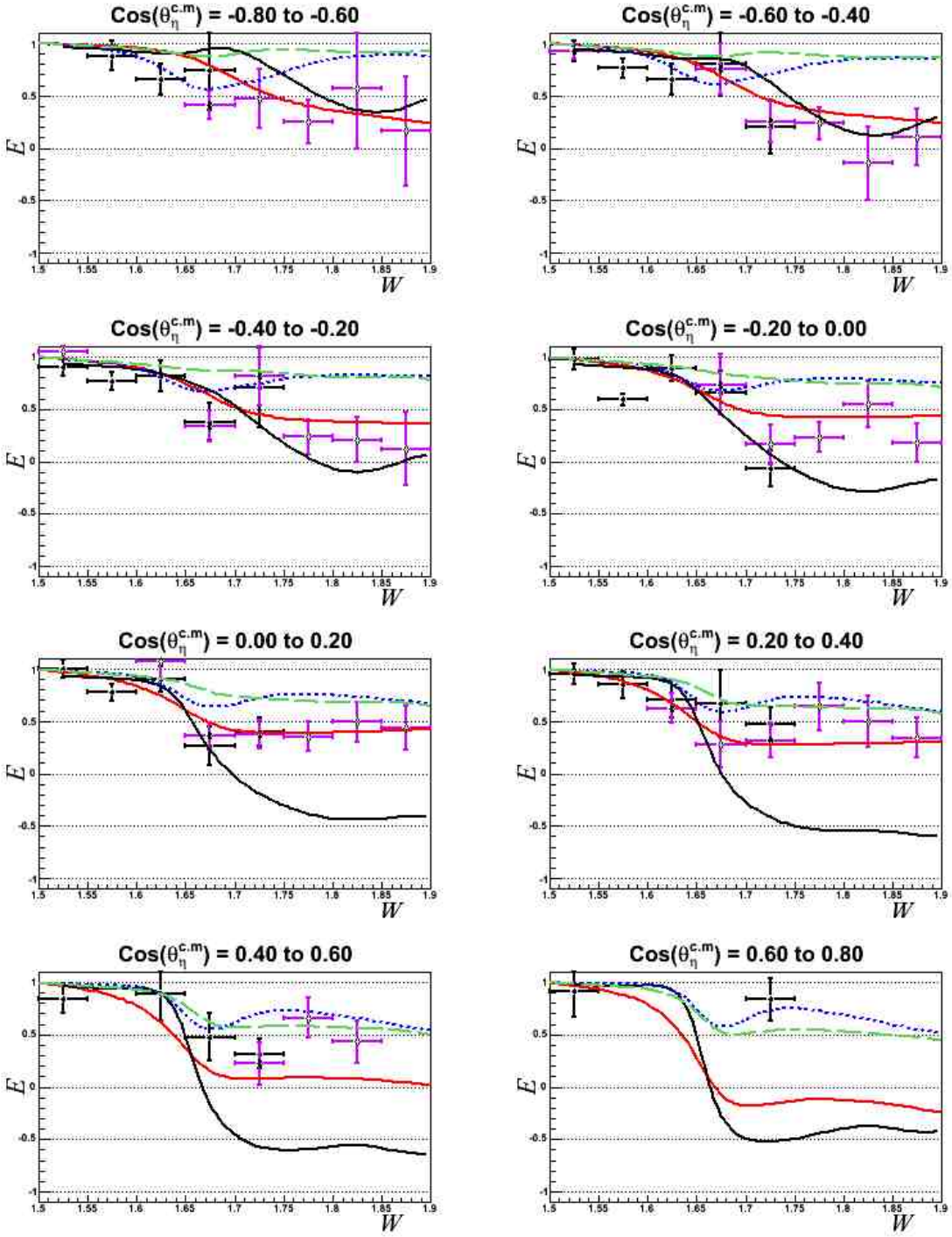

Figure 5.3: Excitation plots for each $\cos(\theta_\eta^{c.m.})$ bin. Center-of-mass energy W is given in GeV.

Chapter 6

CONCLUSIONS

A better knowledge of the nucleon resonance spectrum is essential to properly understand the structure of the nucleon in terms of of quark models. There are currently no published data for the double polarization observable E.

In every kinematic bin studied in this dissertation, a non-zero value for the helicity asymmetry E was found (though several overlapped zero). This simple observation alone underscores that for understanding the energy region covered by these measurements, awash in overlapping nucleon resonances, these data will be extremely helpful in deconvolving the competing and interfering resonance amplitudes that yield E. The results presented in the previous chapter are the first glimpses of the E observable for η photoproduction, and will provide a benchmark for theoretical models.

Helicity asymmetries were found for the reaction $\gamma + p \rightarrow p + \eta$ at energies of $W = 1500 - 1900$ MeV with large center-of-mass angle coverage. These helicity asymmetries E were compared to the partial-wave models of SAID and Bonn-Gatchina along with the isobar model η-MAID. Without a full partial-wave analysis on the data presented in the previous chapter, no new information can be inferred about possible resonance couplings and parameters with any certainty. However, the data clearly shows that the current models for resonance couplings in η photoproduction are incorrect, despite the models being derived from fits to the current world database (131 data points, including differential cross sections and single polarization observables). Of the four models to which the data has been compared, the 2004 version of SAID does the best once past the region of the $S_{11}(1535)$

resonance. The data from this thesis will give model-builders a better idea of how the resonance spectrum for η photoproduction behaves past threshold energies.

Further studies of the backgrounds for the numerators and denominators seen in the kinematic bins within this work should be performed in hopes of creating a better method for fitting the histograms. Attempts are currently being made to generate an accurate Monte Carlo simulation for the FROST experiment to better model the background. If successful, the resulting observables should become more stable, and some kinematic bins may no longer need to be excluded from the final results. Studies should be performed to better understand the structure that is seen in the lower energy bins of η photoproduction when using the butanol target with FROST. The cause of this structure is unknown, but is assumed to be caused by some aspect of the target that has not been fully understood.

Further theoretical predictions for the helicity asymmetry E for η photoproduction should also be obtained. In particular, effective Lagrangian predictions from Nakayama and Haberzettl should be available soon and will provide a physics-driven comparison to the data [35].

The next step in investigating the nucleon resonance spectrum is to measure more double polarization observables for η photoproduction. The Σ single polarization observable and the G double polarization observable will be extracted from the g9a data set. In 2011, the CLAS g9b run period took data with a polarized photon beam and a transversely polarized target with both circularly and linearly polarized photon beams. With the transversely polarized target and polarized beam it should be possible to measure the observables T, P, F, and H.

The data from the this thesis, along with the Σ, G, T, F, P, and H observable data, will help refine models of the nucleon by almost completely specifying the

W-dependence of the helicity amplitudes for the process. Every viable model will need to agree with this nearly complete and stringent data set.

BIBLIOGRAPHY

[1] K. Nakamura *et al.*, J. Phys. **37**, 075021, 30 (2010).

[2] K. Nakamura *et al.*, op. cit., 1149 (2010).

[3] R. Arndt, W. Briscoe, R. Workman, and I. Strakovsky, *SAID Partial-Wave Analysis*. URL: http://gwdac.phys.gwu.edu/ (accessed November 11, 2011).

[4] W.-T. Chiang, S.-N. Yang, L. Tiator, and D. Drechsel, Nucl. Phys. A **700**, 429 (2002).

[5] K. Nakamura *et al.*, op. cit., 625 (2010).

[6] F. J. Klein, *Complete pseudoscalar photo-production measurements*, in *May 2011 NSTAR Conference Proceedings*, Newport News, VA, 2011.

[7] C. Keith, *Jefferson Lab Frozen Spin Target*. URL: https://userweb.jlab.org/∼ckeith/frozen/frozen.html (accessed November 11, 2011).

[8] Jefferson Science Associates, LLC., *Jefferson Lab website*. URL: http://www.jlab.org (accessed November 12, 2011).

[9] D. I. Sober *et al.*, Nucl. Instrum. Methods Phys. Res. A **440** (2), 263 (2000).

[10] C. Keith, private communication (2011).

[11] Y. G. Sharabian *et al.*, Nucl. Instrum. Methods Phys. Res. A **556** (1), 246 (2006).

[12] M. D. Mestayer *et al.*, Nucl. Instrum. Methods Phys. Res. A **449** (1-2), 81 (2000).

[13] B. A. Mecking *et al.*, Nucl. Instrum. Methods Phys. Res. A **503** (3), 513 (2003).

[14] A. Bock *et al.*, Phys. Rev. Lett. **81** (3), 534 (1998).

[15] R. L. Walker, Phys. Rev. **182** (5), 1729 (1969).

[16] K. Nakamura *et al.*, op. cit., 374 (2010).

[17] A. V. Anisovich *et al.*, Eur. Phys. J. **A25**, 427 (2005).

[18] H. Olsen and L. Maximon, Phys. Rev. **114** (3), 887 (1958).

[19] C. Keith, *Freezing the Spin of the Proton*. URL: https://userweb.jlab.org/∼ckeith/frozen/frozen.pdf (accessed November 12, 2011).

[20] A. W. Overhauser, Phys. Rev. **92** (2), 441 (1953).

[21] A. Abragam and M. Goldman, Rep. Prog. Phys. **41**, 395 (1978).

[22] M. Borghini and K. Scheffler, Phys. Rev. Let. **26** (22), 887 (1971).

[23] M. Goldman, Appl. Magn. Reson. **34**, 219 (2008).

[24] Alcorn, J. *et al.*, Nucl. Instrum. Methods Phys. Res. A **522**, 294 (2004).

[25] C. Curtis, J. Dahlberg, W. Oren, J. Preble, and K. Tremblay, *Fiducialization of Superconducting Radio Frequency Cryomodules at Jefferson Lab*, URL: wwwold.jlab.org/accel/survalign/documents/publ/iwaa9_curtis.pdf.

[26] Jefferson Science Associates, LLC., *Accelerator Overview*. URL: http://www.jlab.org/accel/ops_orientation/acc_overview.html (accessed october 3, 2011).

[27] C. D. Keith, AIP Conference Proceedings **1149** (1), 886 (2009).

[28] E. S. Smith *et al.*, Nucl. Instrum. Methods Phys. Res. A **432** (2-3), 265 (1999).

[29] E. Pasyuk, *Brief users guide to GPID*, URL: https://misportal.jlab.org/ul/Physics/Hall-B/clas/viewFile.cfm/2007-008.pdf?documentId=395.

[30] R. Team, *The ROOT Users Guide 5.26*, URL: http://root.cern.ch/download/doc/Users_Guide_5_26.pdf.

[31] K. Nakamura *et al.*, op. cit., 354 (2010).

[32] J. McAndrew, *Calculation of the Calibration Constant*. URL: http://clasweb.jlab.org/rungroups/g9/wiki/index.php/Calculation_of_Calibration_Constant (accessed November 3, 2011).

[33] T. DuBose, *Beam Polarization (Circ.)*. URL: http://clasweb.jlab.org/rungroups/g9/wiki/index.php/Beam_Polarization_(Circ.) (accessed November 3, 2011).

[34] M. Dugger and B. G. Ritchie, *Phase space dependent scale factors for FROST g9a data*. URL: http://www.public.asu.edu/∼dugger/sfNote.pdf (accessed November 3, 2011).

[35] K. Nakayama and H. Haberzettl, Phys. Rev. C **73** (4), 045211 (2006).

APPENDIX A

DENOMINATOR AND NUMERATOR FITS

This appendix provides the fit results used in the construction of the E observable for this analysis. The fits are presented in denominator-numerator pairs, with the denominator always shown first. For energies where multiple topologies have fits, the fits for Topology 2 will always be shown first.

In each set of fits, several points should be noted. Most importantly, the first row is coupled with the second row and the third row with the fourth row. The upper of the coupled rows shows the full yield (in black data points), the fit to the background (shown as a blue line), and the signal resulting from the subtracted background (shown in pink). The lower of the coupled rows shows this resulting signal as a bar-style histogram with a zero-line drawn in pink, and the integration region used to determine the meson cound shaded in light blue.

On the individual histograms are several pieces of information. In the lower right is the meson count that is used when constructing the E observable. The upper left of the denominator plots shows the probability (out of 1) of the fit to the background. The upper right of the denominator plots shows the order in Legendre polynomials used in the fit, with 1 corresponding to a constant. The upper left on the numerator plots shows the value and error of a constant fit to the numerator background. Figures for bins with "BIN NOT USED" across them were not used in this analysis for reasons outlined in Chapter 5.

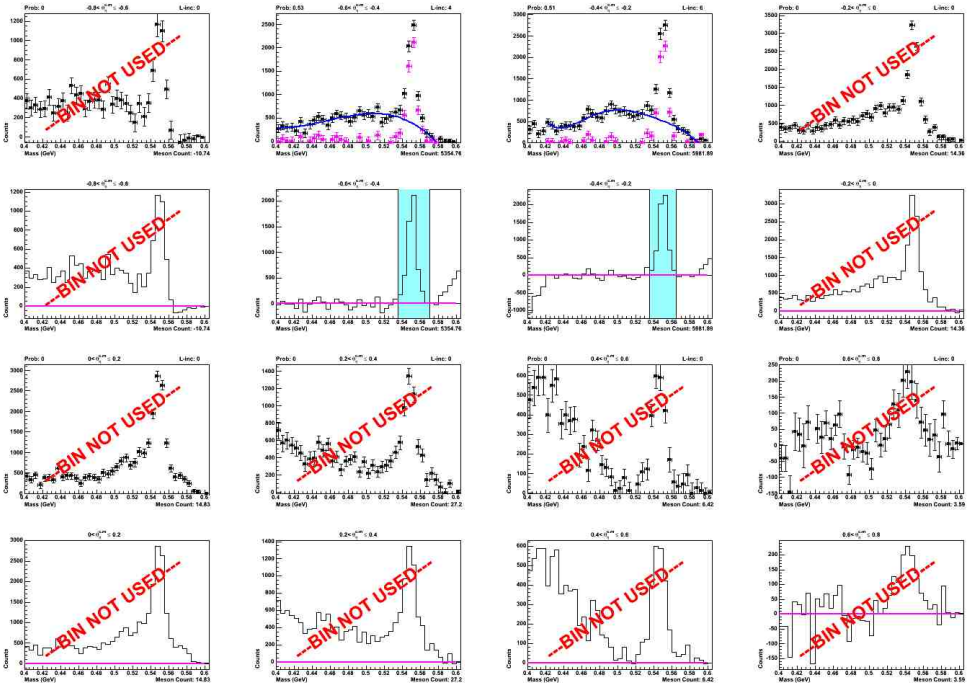

Figure A.1: Denominator fits for Topology 2 for $W = 1500 - 1550$ MeV.

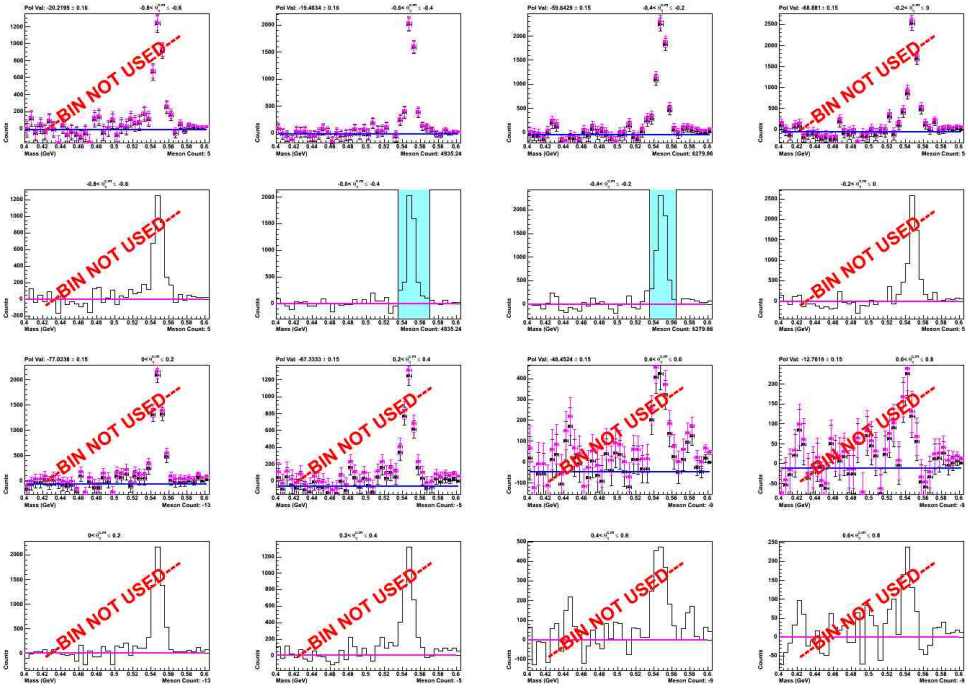

Figure A.2: Numerator fits for Topology 2 for $W = 1500 - 1550$ MeV.

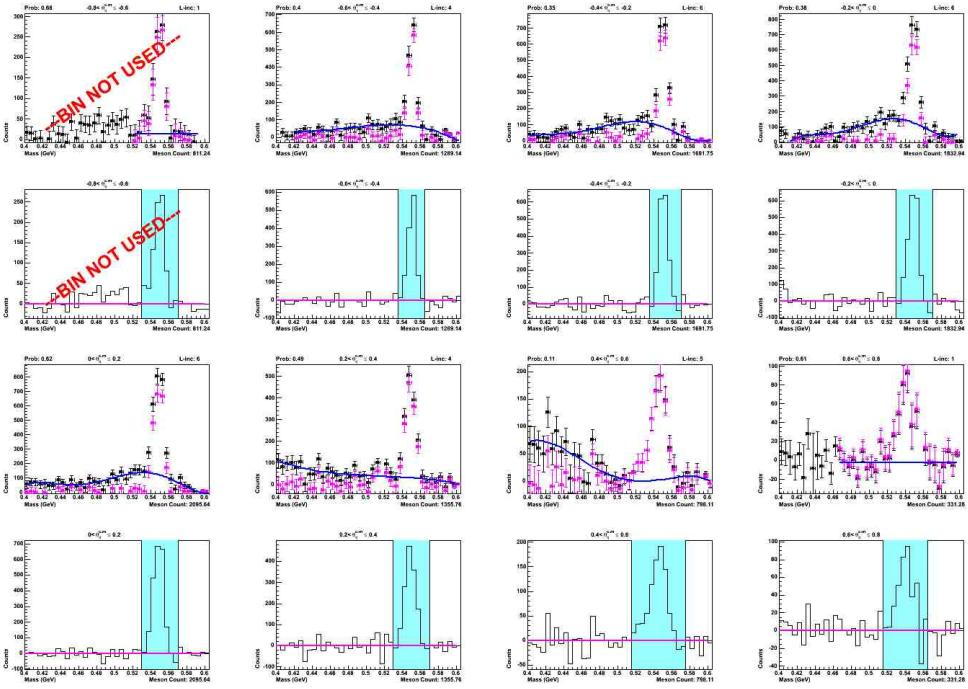

Figure A.3: Denominator fits for Topology 3 for $W = 1500 - 1550$ MeV.

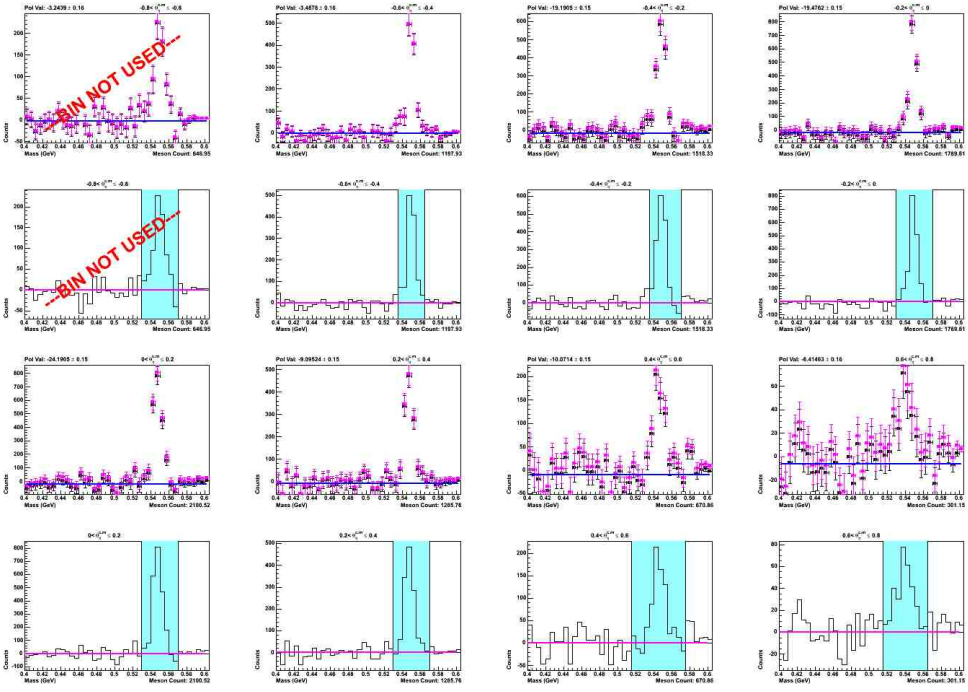

Figure A.4: Numerator fits for Topology 3 for $W = 1500 - 1550$ MeV.

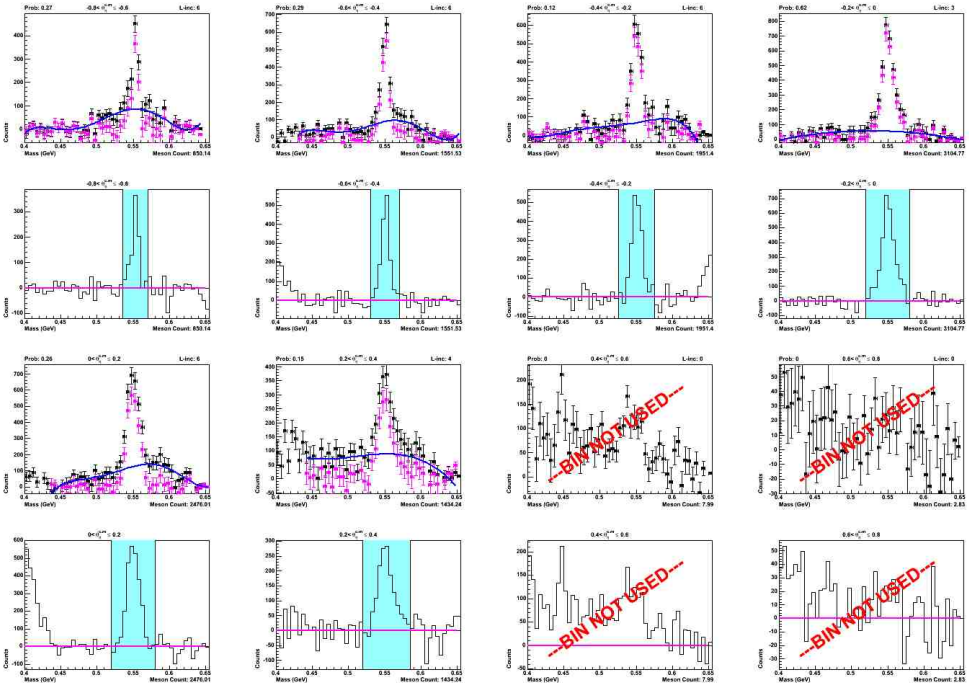

Figure A.5: Denominator fits for Topology 3 for $W = 1550 - 1600$ MeV.

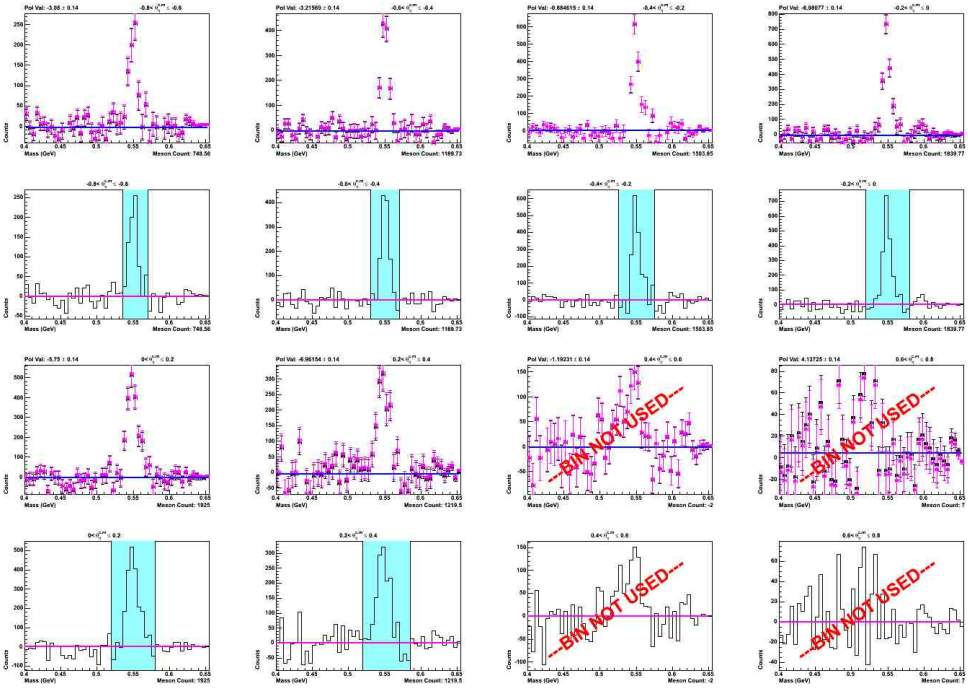

Figure A.6: Numerator fits for Topology 3 for $W = 1550 - 1600$ MeV.

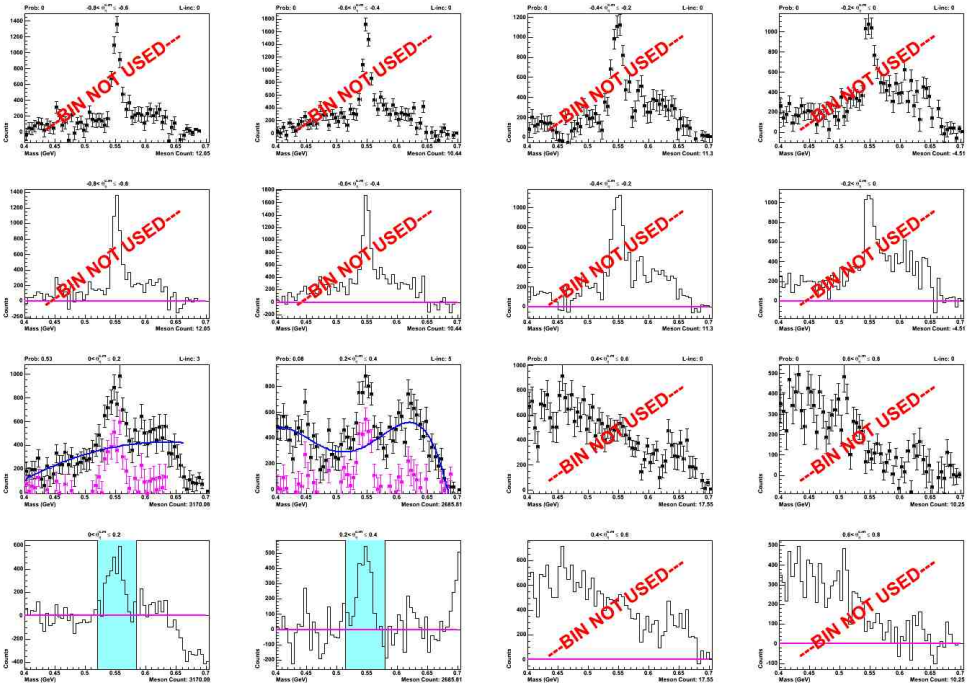

Figure A.7: Denominator fits for Topology 2 for $W = 1600 - 1650$ MeV.

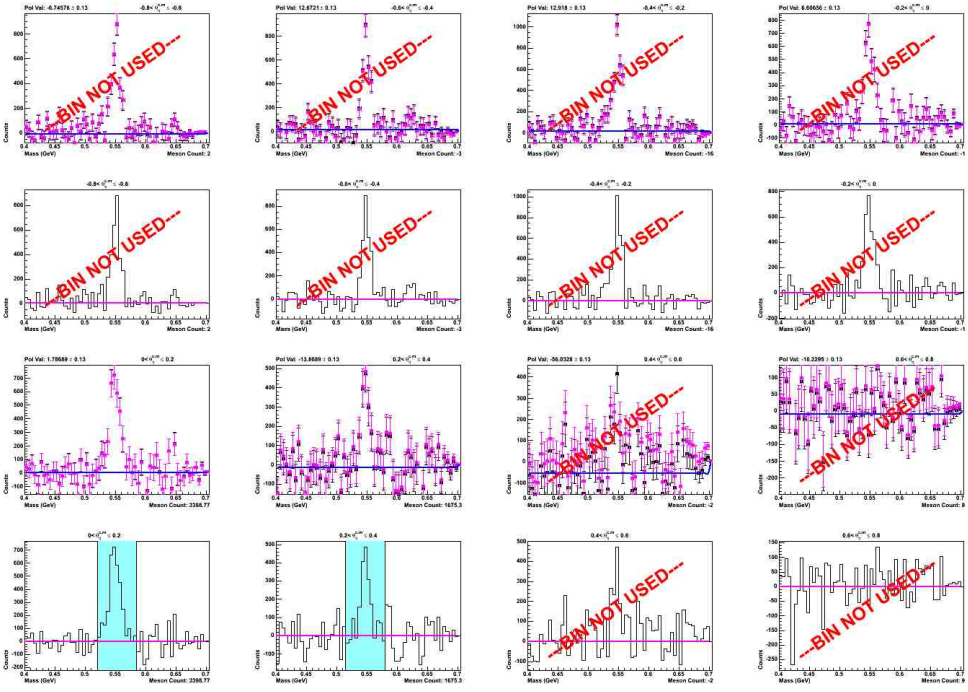

Figure A.8: Numerator fits for Topology 2 for $W = 1600 - 1650$ MeV.

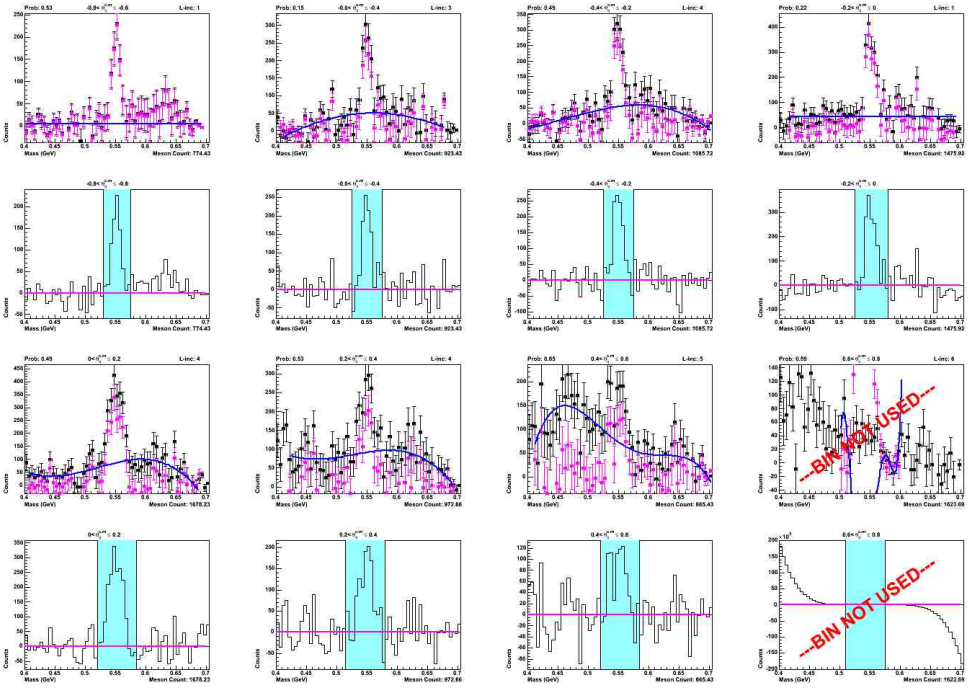

Figure A.9: Denominator fits for Topology 3 for $W = 1600 - 1650$ MeV.

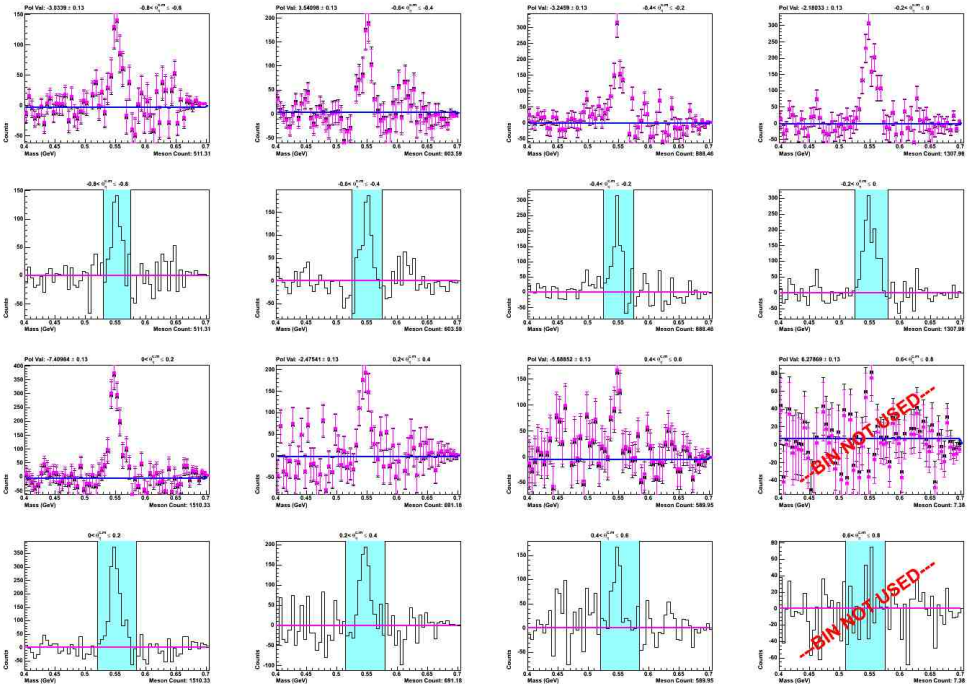

Figure A.10: Numerator fits for Topology 3 for $W = 1600 - 1650$ MeV.

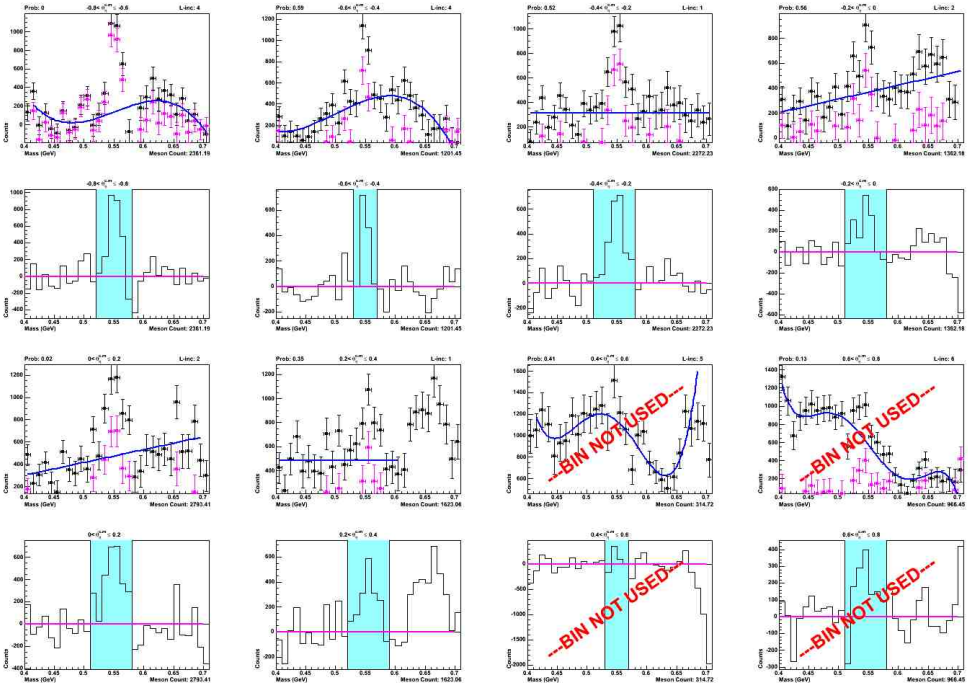

Figure A.11: Denominator fits for Topology 2 for $W = 1650 - 1700$ MeV.

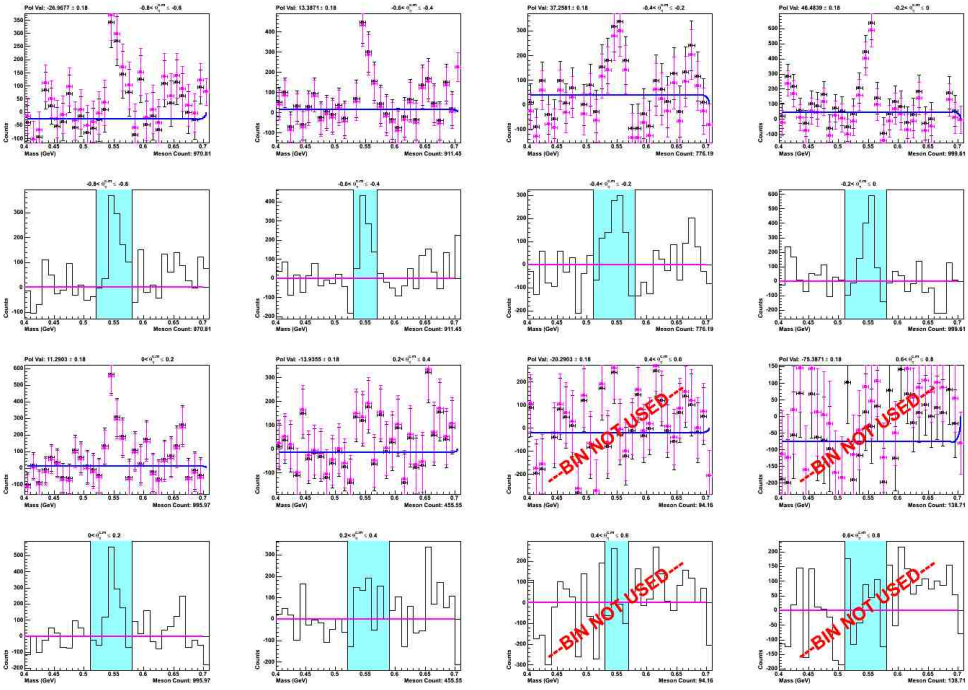

Figure A.12: Numerator fits for Topology 2 for $W = 1650 - 1700$ MeV.

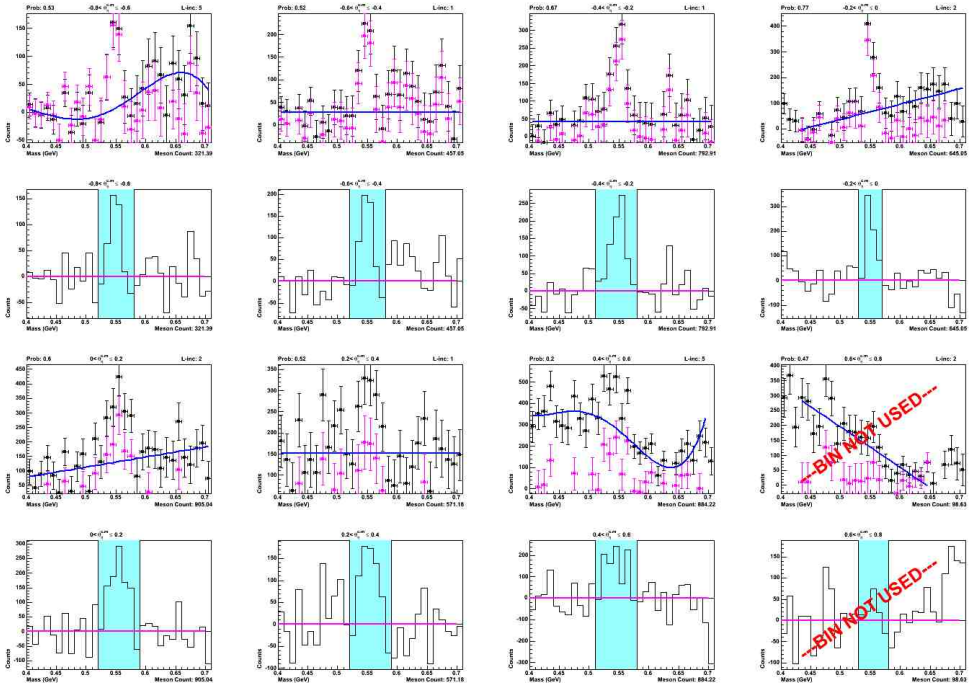

Figure A.13: Denominator fits for Topology 3 for $W = 1650 - 1700$ MeV.

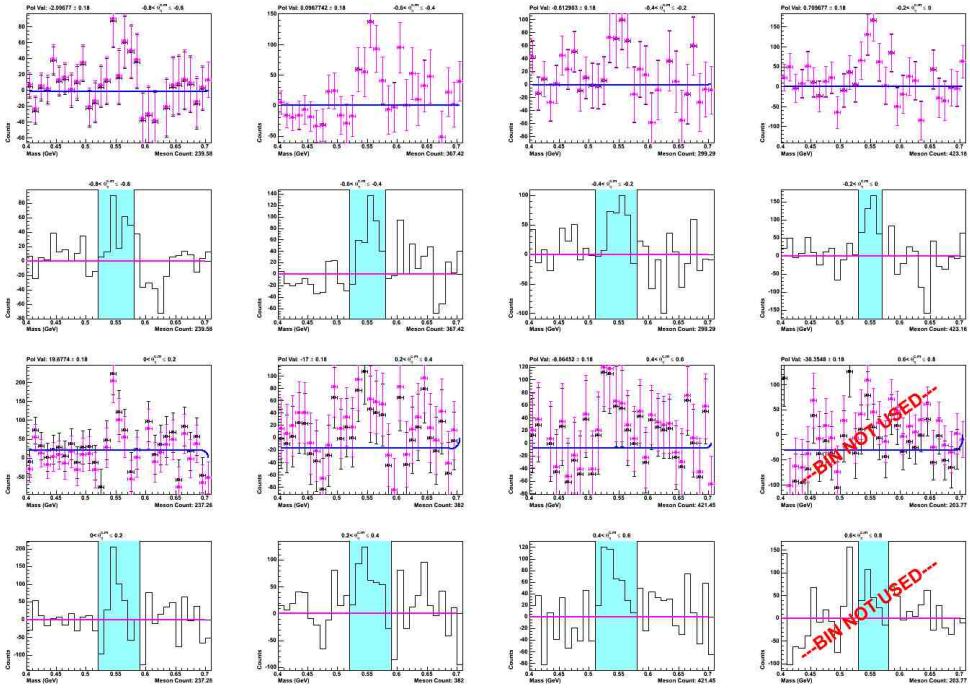

Figure A.14: Numerator fits for Topology 3 for $W = 1650 - 1700$ MeV.

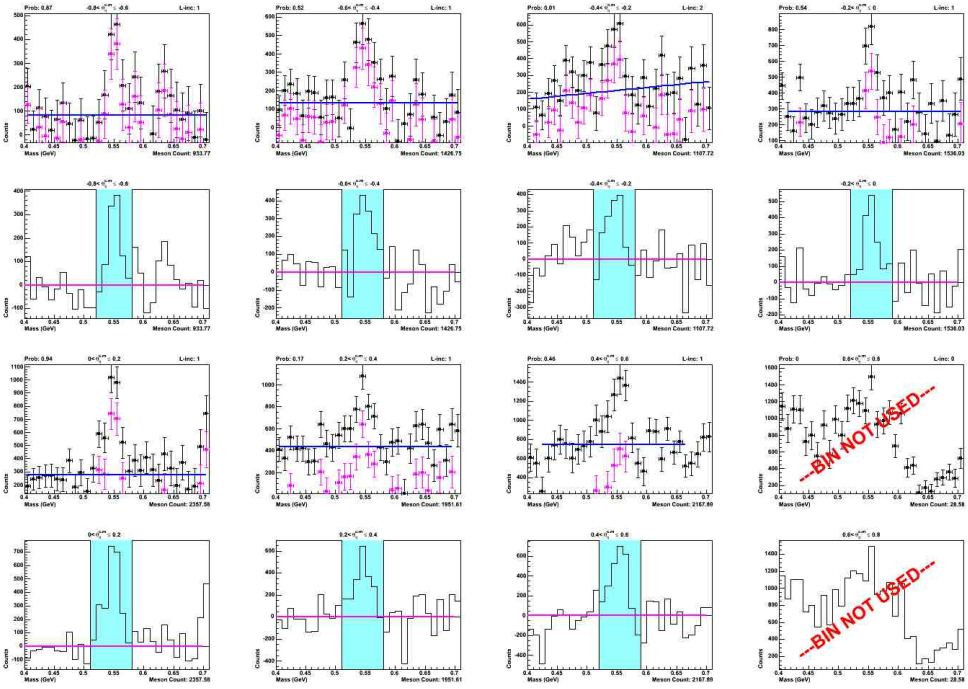

Figure A.15: Denominator fits for Topology 2 for $W = 1700 - 1750$ MeV.

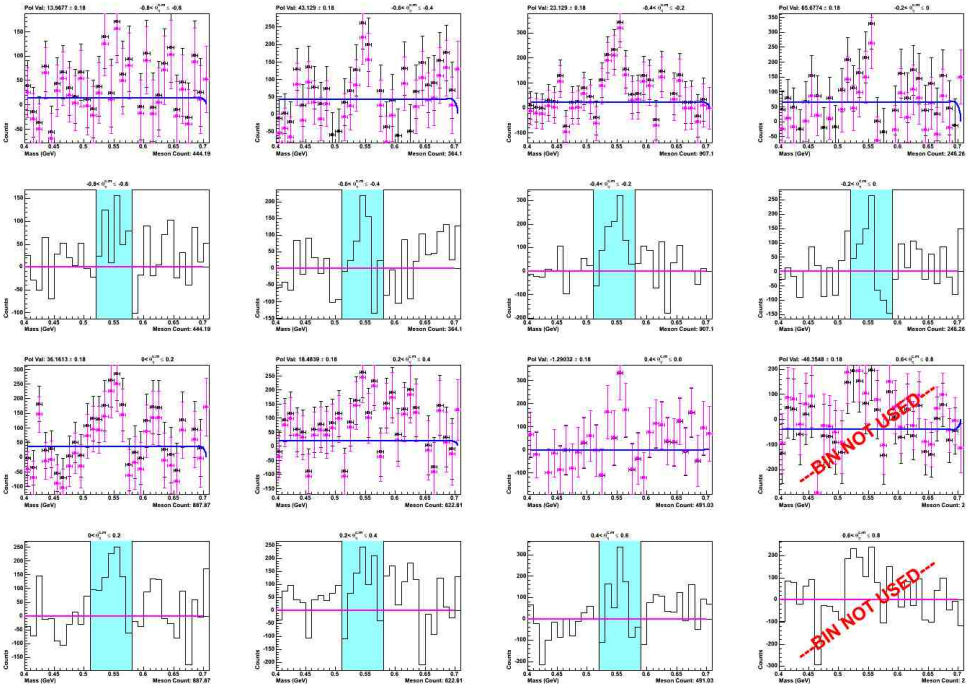

Figure A.16: Numerator fits for Topology 2 for $W = 1700 - 1750$ MeV.

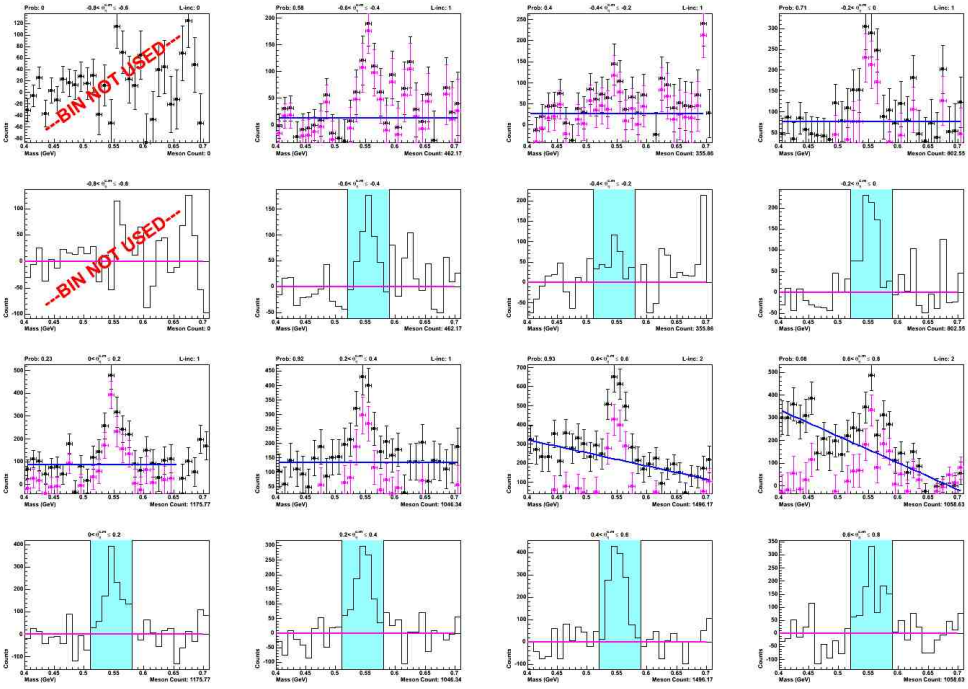

Figure A.17: Denominator fits for Topology 3 for $W = 1700 - 1750$ MeV.

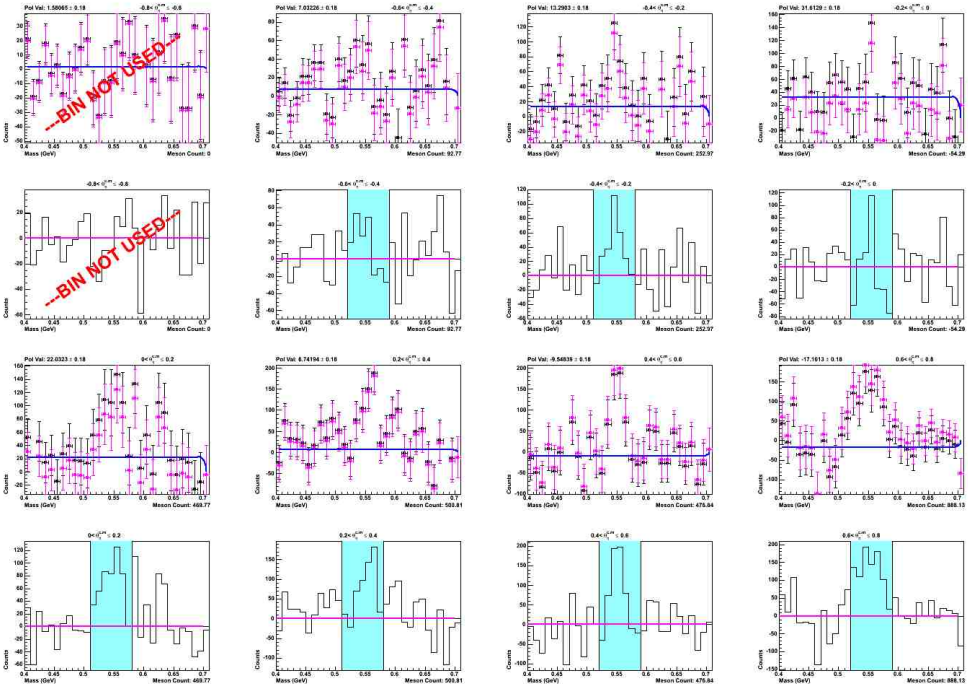

Figure A.18: Numerator fits for Topology 3 for $W = 1700 - 1750$ MeV.

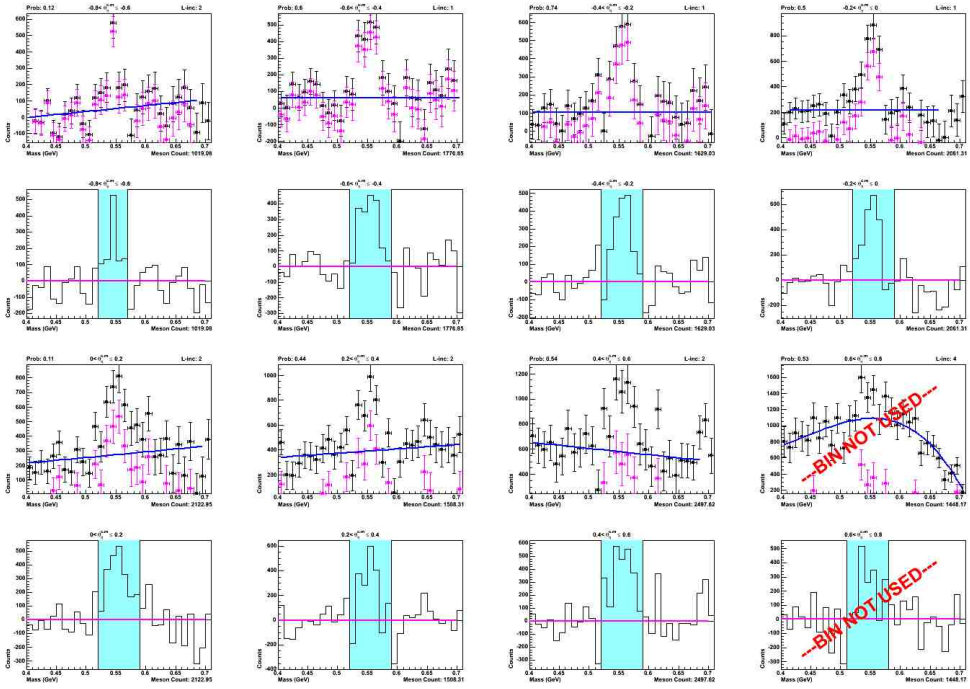

Figure A.19: Denominator fits for Topology 2 for $W = 1750 - 1800$ MeV.

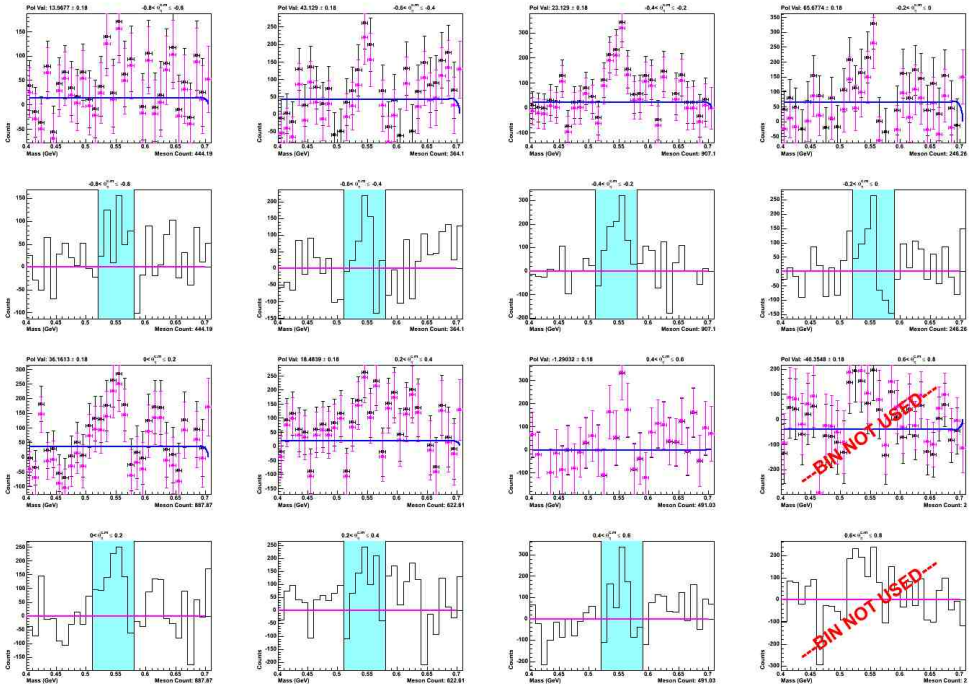

Figure A.20: Numerator fits for Topology 2 for $W = 1750 - 1800$ MeV.

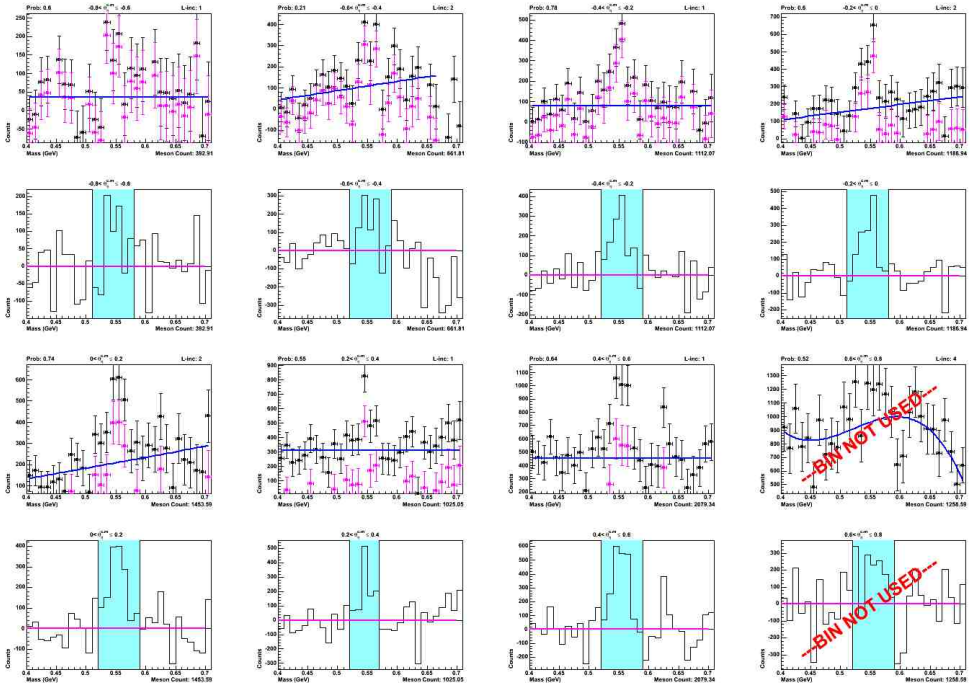

Figure A.21: Denominator fits for Topology 2 for $W = 1800 - 1850$ MeV.

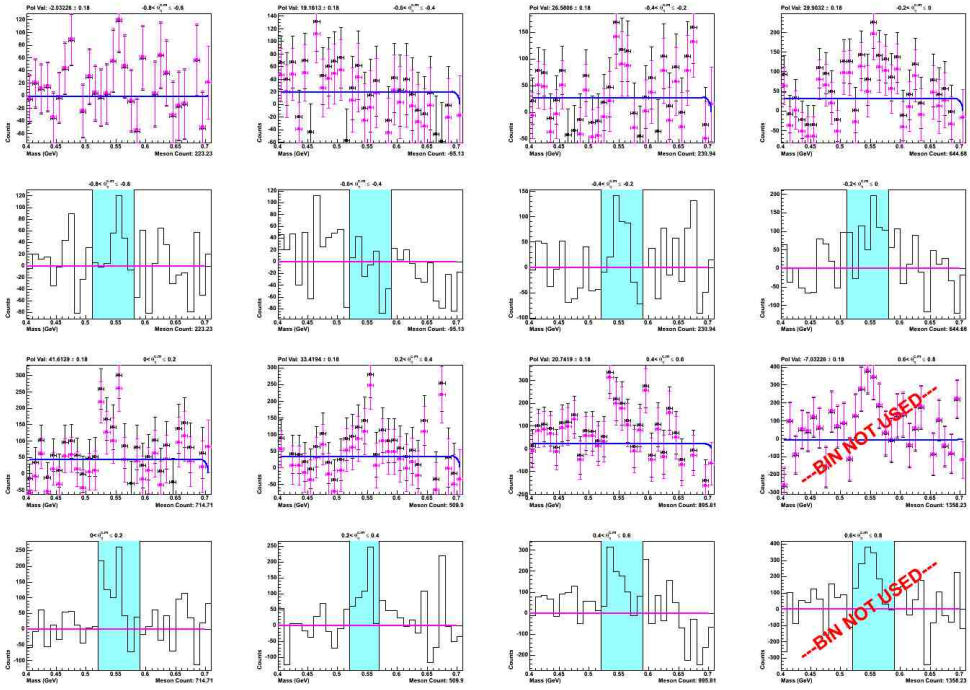

Figure A.22: Numerator fits for Topology 2 for $W = 1800 - 1850$ MeV.

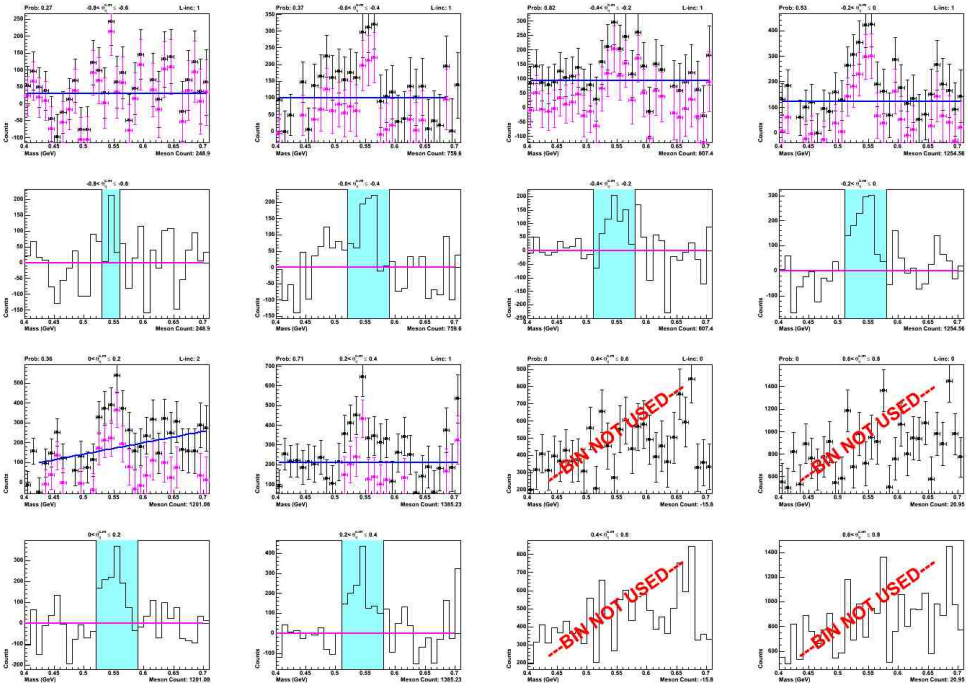

Figure A.23: Denominator fits for Topology 2 for $W = 1850 - 1900$ MeV.

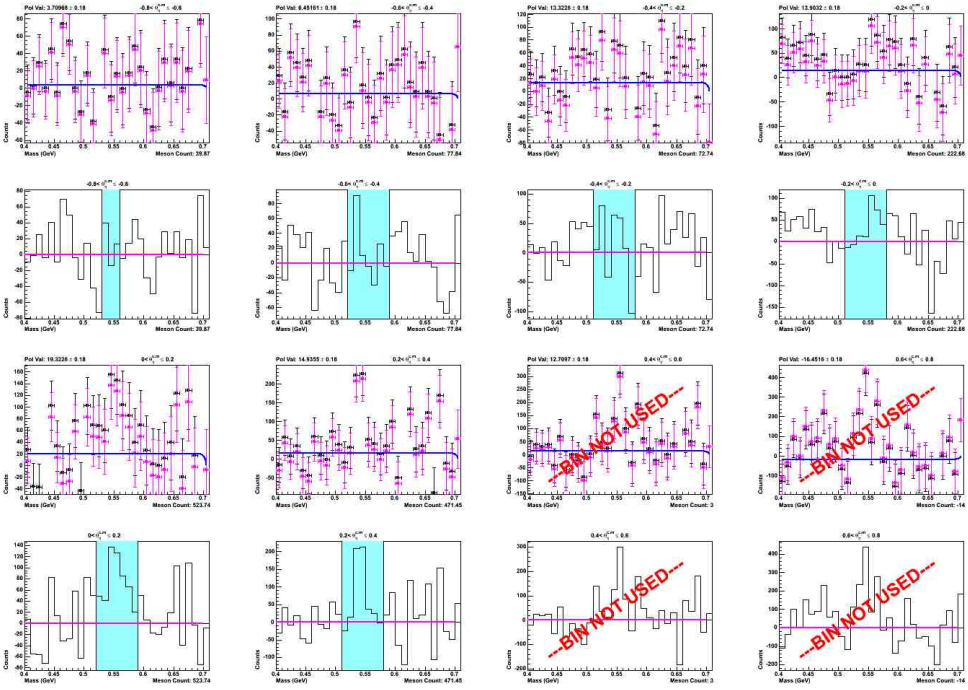

Figure A.24: Numerator fits for Topology 2 for $W = 1850 - 1900$ MeV.